Cover Page

Universiteit Leiden

Leiden University Repository

The handle http://hdl.handle.net/1887/18671 holds various files of this Leiden University dissertation.

Author: Albers, Harald
Title: Development of ATX and DUSP inhibitors : inhibiting phosphate ester hydrolysis in biology
Issue Date: 2012-04-04

Development of ATX and DUSP inhibitors

Inhibiting phosphate ester hydrolysis in biology

Harald Matheas Henricus Gerardus Albers

Development of ATX and DUSP inhibitors

Inhibiting phosphate ester hydrolysis
in biology

PROEFSCHRIFT

ter verkrijging van
de graad van Doctor aan de Universiteit Leiden,
op gezag van Rector Magnificus prof.mr. P.F. van der Heijden,
volgens besluit van het College voor Promoties
te verdedigen op woensdag 4 april 2012
klokke 15.00 uur

door

Harald Matheas Henricus Gerardus Albers

geboren te Venray

in 1980

Promotiecommissie

Promotores:	Prof.dr. H.S. Overkleeft Prof.dr. J.J. Neefjes
Copromotor:	Dr. H. Ovaa
Overige leden:	Prof.dr. A.P. IJzerman Dr. W.H. Moolenaar Dr. A. Perrakis Dr. E.W. van Tilburg

© Harald Albers, 2012

ISBN: 978-90-8570-797-4

Cover: Crystal structure of inhibitor HA155 bound to the ATX active site.

The work described in this thesis was performed at the Divisions of Cellular Biochemistry and Cell Biology II of the Netherlands Cancer Institute, Amsterdam, The Netherlands. Financial support was provided by the Netherlands Organization for Scientific Research (NWO), the Ducth Cancer Society (KWF) and The Netherlands Proteomics Centre supported by The Netherlands Genomics Initiative.

Publication of this thesis was financially supported by the Dutch Cancer Society (KWF) and the Netherlands Cancer Institute. Printed by Wöhrmann Print Service, Zutphen.

Table of contents

List of abbreviations 8

CHAPTER 1 11

Chemical evolution of autotaxin inhibitors: *An introduction*

CHAPTER 2 27

Biological validation of a boronic acid-based inhibitor of autotaxin reveals rapid turnover of LPA in the circulation

CHAPTER 3 43

Discovery and optimization of boronic acid-based inhibitors of autotaxin: *How did we exactly arrive at these inhibitors?*

CHAPTER 4 63

Structure-based design of novel boronic acid-based inhibitors of autotaxin

CHAPTER 5 85

From the phosphodiesterase autotaxin to dual specificity phosphatases: *A short introduction on dual specificity phosphatases*

CHAPTER 6 91

Controlling bacterial infection by human dual specificity phosphatase inhibition

APPENDICES

Summary and future prospects 111

Nederlandse samenvatting 115

Curriculum vitae 119

List of publications 121

Nawoord 123

List of abbreviations

ABP	activity-based probe
ABTS	2,2'-azino-bis(3-ethylbenzothiazoline-6-sulphonic acid)
AP	alkaline phosphatase
Ap_nA	diadenosine polyphosphates
APT	attached proton test
ATP	adenosine-5'-triphosphate
ATX	autotaxin
AU	arbitrary units
bs	broad singlet
BSA	bovine serum albumin
CDC	cell division cycle
CFU	colony forming units
COSY	correlation spectroscopy
cPA	cyclic phosphatidic acid
δ	chemical shift
d	doublet
dd	double doublet
DMEM	Dulbecco's modified eagle's medium
DMF	*N*,*N*-dimethylformamide
DMSO	dimethyl sulfoxide
dppf	(diphenylphosphino) ferrocene
DUSP	dual specificity phosphatase
EC_{50}	half maximal effective concentration
EDTA	ethylenediaminetetraacetic acid
EHEC	Enterohemorragische *Escherichia coli*
ENPP	ecto-nucleotide pyrophosphatase and phosphodiesterase
FACS	fluorescence-activated cell sorting
FAF	fatty acid-free
FCS	fetal calf serum
FRET	Förster fluorescence resonance energy transfer
FVB	friend virus B-type
h	hour(s)
HPLC-MS/MS	high performance liquid chromatography–tandem mass spectrometry
HRP	horseradish peroxidase
HTS	high-throughput screening
HVA	homo-vanillic acid
Hz	Hertz
IC_{50}	half maximal inhibitory concentration
J	coupling constant
K	Kelvin
LB	lysogeny broth
λ_{em}	emission wavelength
λ_{ex}	excitation wavelength
LPA	lysophosphatidic acid
LPC	lysophosphatidylcholine
LPP	lipid phosphate phosphatases

lysoPLD	lysophospholipase D
m	multiplet
M	molar
MAG	monoacylglycerol
MDR	multidrug resistance
min	minute(s)
MIO	multiplicity of infection
m/z	mass-to-charge ratio
NAD^+	nicotinamide adenine dinucleotide
NCI	National Cancer Institute
NMR	nuclear magnetic resonance
OD_{595}	optical density at 595 nm
OMF	3-*O*-methylfluorescein
OMFP	3-*O*-methylfluorescein phosphate
PAGE	polyacrylamide gel electrophoresis
PAO	phenylarsine oxide
PBS	phosphate buffered saline
PC	proprotein convertases
Pd/C	palladium on activated charcoal
PET	positron emission tomography
PI	percentage inhibition
PKB	protien kinase B
pNP	*para*-nitrophenol
pNPP	(*para*-nitrophenyl) phosphate
pNP-TMP	thymidine 5’-monophosphate *para*-nitrophenyl ester
ppm	parts per million
PSP	protein serine/threonine phosphatase
PTP	protein tyrosine phosphatase
PTPN	tyrosine-protein phosphatase non-receptor type
RA	residual activity
RMSD	root-mean-square deviation
RNA	ribonucleic acid
rpm	revolutions per minute
rt	room temperature
s	singlet
S.	*Salmonella*
S1P	sphingosine 1-phosphate
SAR	structure-activity relationship
SDS	sodium dodecyl sulphate
siRNA	small interfering RNA
SMB	somatomedin B
PEG	polyethylene glycol
SPC	sphingosylphosphorylcholine
TLC	thin layer chromatography
Tris	2-amino-2-(hydroxymethyl)-1,3-propanediol
U	enzyme unit
UDP	uridine diphosphate
Xac	*X. axonopodis* pV. *citri*.

CHAPTER 1

Chemical evolution of autotaxin inhibitors: *An introduction*

Harald M.H.G. Albers and Huib Ovaa, *Accepted for publication in Chemical Reviews.*

Abstract. Autotaxin (ATX) is a potential drug target implicated in various diseases, including cancer. ATX was originally isolated as a tumor cell motility factor from melanoma cells in 1992. It then took a decade to find that ATX has lysophospholipase D activity and is responsible for the production of the bioactive lipid lysophosphatidic acid (LPA). The link between ATX-LPA axis and disease has triggered the development of ATX inhibitors. This chapter focuses on the development of ATX inhibitors described in academic and patent literature covering both lipid-based and small molecule inhibitors, including the ATX inhibitors described in the following chapters of this thesis to place them in context of the current literature.

1.1 Introduction

In 1992, autotaxin (ATX or ENPP2) was isolated as an autocrine motility factor from melanoma cells.[1] The ~120 kDa glycoprotein ATX belongs to a small family named ecto-nucleotide pyrophosphatase and phosphodiesterase (ENPP) which consists of 7 family members.[2] ATX is the only ENPP family member with lysophospholipase D (lysoPLD) activity and is responsible for the hydrolysis of lysophosphatidylcholine (LPC) to produce the bioactive lipid lysophosphatidic acid (LPA) (Scheme 1).[3,4] LPA acts on specific G protein-coupled receptors and thereby stimulates the migration, proliferation and survival of many cell types.[5,6] ATX is produced in various tissues and is the major LPA-producing enzyme in the circulation. After biosynthesis by ATX, LPA is subject to degradation by membrane-bound lipid phosphate phosphatases (LPPs).[7,8]

ATX is essential for vascular development[9,10] and is found overexpressed in various human cancers.[11] Forced overexpression of ATX or individual LPA receptors promotes tumor progression in mouse models,[12-15] while LPA receptor deficiency protects from colon carcinogenesis.[16] In addition, to its role in cancer, ATX-LPA signaling has been implicated in lymphocyte homing and (chronic) inflammation,[17] fibrotic diseases,[18,19] thrombosis[20] and cholestatic pruritus.[21] Given its role in human disease, the ATX-LPA axis is an interesting target for therapy that deserves significant attention. The fact that ATX is an extracellular enzyme makes it even more attractive as a drug target.

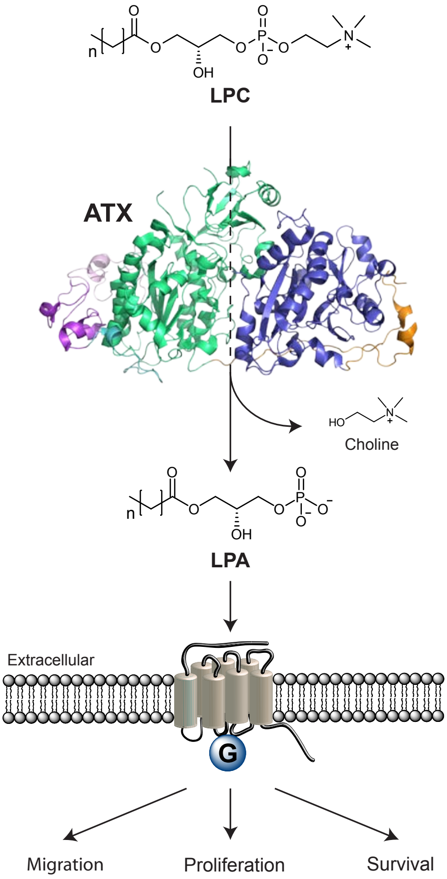

Scheme 1: ATX is responsible for hydrolyzing LPC into LPA in an extracellular environment. This reaction is catalyzed by a threonine residue and two zinc ions present in the ATX active site. LPA activates specific G protein-coupled receptors stimulating migration, proliferation and survival of cells. ATX is displayed as a cartoon representation of the crystal structure (PD ID 2XR9) with the SMB domains in purple, the PDE domain in green and the nuclease-like domain in blue.

1.2 ATX protein

Alternative splicing of the ATX gene (enpp2) results in three distinct isoforms (α, β and γ) which are differentially expressed.[22,23] ATX β (863 aa) is the best studied isoform and is identical to plasma lysoPLD. ATX β is mainly expressed in peripheral tissues, whereas lower expression levels are observed in the central nervous system. In contrast, the ATX γ (889 aa) isoform is predominately expressed in the central nervous system. ATX α (915 aa), the original melanoma-derived isoform, exhibits the lowest expression levels in both the central nervous system and peripheral tissues. The ATX α isoform contains a non-specific protease cleavage site which is not present in the other isoforms.[22] All the three ATX isoforms exhibit similar catalytic activities *in vitro*.[22]

ATX is produced initially as a pre-pro-enzyme that has an N-terminal signal peptide required for secretion.[24] This signal peptide is removed by a signal peptidase and ATX is subsequently cleaved by proprotein convertases (PCs) like furin.[24] The removal of an N-terminal octapeptide in ATX by PCs is associated with an enhancement of ATX activity.[24] The proteolytically processed ATX is secreted and it consists of several domains. Starting from its N-terminus ATX has two somatomedin B (SMB)-like domains, a central catalytic phosphodiesterase (PDE) domain and an inactive nuclease-like domain as displayed in Scheme 1. The hydrolytic activity of ATX predominately originates from a threonine residue and two zinc ions in the ATX active site located in the PDE domain.[25] Extending from the ATX active site there is a hydrophobic pocket where the alkyl chain of its lipid substrates binds.[26]

1.3 Natural substrates of ATX

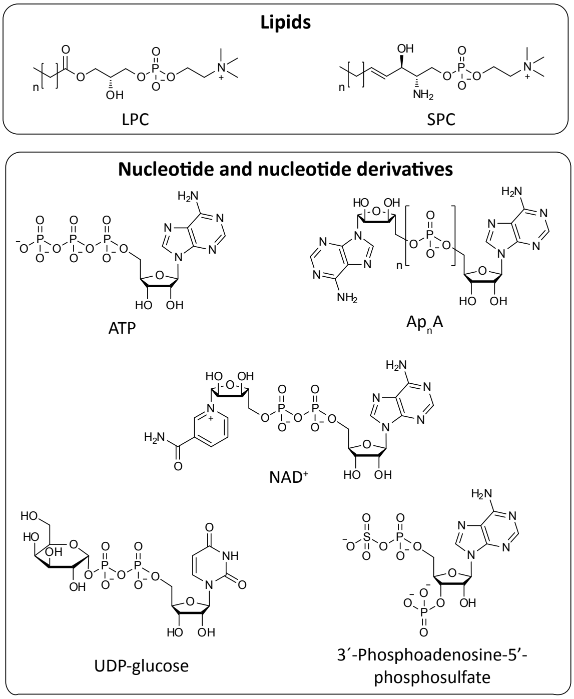
Lipids
LPC
SPC
Nucleotide and nucleotide derivatives
ATP
Ap$_n$A
NAD$^+$
UDP-glucose
3´-Phosphoadenosine-5’-phosphosulfate

Figure 1: Identified natural substrates of ATX.

Next to LPC hydrolysis, ATX is also capable of hydrolyzing sphingosylphosphorylcholine (SPC, Figure 1) into sphingosine 1-phosphate (S1P).[27] S1P has signaling properties comparable to those of LPA while acting on S1P receptors.[28-30] It is however, doubtful how relevant the contribution of ATX is to S1P production *in vivo*. S1P is thought to originate mainly from the phosphorylation of sphingosine by sphingosine kinases, rather than through SPC hydrolysis by ATX.[31]

Next to recognizing the lipids LPC and SPC as substrates, ATX can also hydrolyze nucleotides, like its family members ENPP1 and ENPP3. *In vitro* established nucleotide and nucleotide-derived substrates of ATX consist of adenosine-5'-triphosphate (ATP), diadenosine polyphosphates (Ap_nA), uridine diphosphate glucose

(UDP-glucose), nicotinamide adenine dinucleotide (NAD^+) and 3’-phosphoadenosine-5’-phosphosulfate (Figure 1).[2] The physiological relevance of ATX-mediated hydrolysis of these nucleotide substrates is still unclear.

1.4 Assays to study ATX activity

In the search for inhibitors, appropriate *in vitro* assays are required to monitor the activity of the enzyme of interest. Over the last ten years various assays have been developed and used to study the activity of ATX. ATX assays can roughly be divided in two classes depending on the kind of ATX substrate used for the activity measurement. The first class uses the physiological ATX substrate LPC and the second class uses unnatural ATX substrates.

1.4.1 LPC-based assays

As depicted in Table 1, ATX hydrolyzes LPC into LPA and choline. Both products can be used to measure ATX activity. When a ^{14}C label is introduced in the lipid tail of LPC, ATX activity can be measured by radiometry.[32,33] When radiolabeled LPC is hydrolyzed by ATX the produced LPA contains this radiolabel. After lipid extraction of the ATX-LPC incubation mixture and separation of LPC and LPA using thin layer chromatography (TLC),[4] activity of ATX can be quantified from the ^{14}C-LPA product. Although this classical method is robust and very sensitive it is not very suitable for high-throughput screening (HTS).

Another way to measure the formation of LPA is by using liquid chromatography–tandem mass spectrometry (LC-MS/MS).[34,35] From an ATX incubation mixture, LPC and LPA are separated by LC and detected by tandem MS. This method is very sensitive and suitable to detect naturally occurring LPA in biological fluids (i.e. plasma).[34-36]

ATX activity can also be measured by the detection of choline.[4,37] When choline is released from the ATX-mediated LPC hydrolysis it can be converted by choline oxidase into betaine (trimethylglycine) and hydrogen peroxide. Subsequently, hydrogen peroxide is used by horseradish peroxidase (HRP) to convert a coloring substrate into its oxidized chromophoric state. Different HRP coloring substrates can be used like 2,2'-azino-bis(3-ethylbenzothiazoline-6-sulphonic acid) (ABTS), homo-vanillic acid (HVA) or Amplex red. ABTS can be detected using absorbance while HVA and Amplex red are detected by fluorescence.[36,38,39] The throughput of this assay is high and suitable for HTS screening.

A danger of the latter assay is that small molecules that don’t inhibit ATX may interfere with the readout by inhibiting the enzymes (HRP or choline oxidase) used in the coloring reaction, which will result in false positives. Another possibility what could result in false positives is that reactive compounds tested in this assay can react with the coloring agent or hydrogen peroxide that is generated during that coloring reaction. Incubating the molecules that are active in this assay with only choline and subsequently adding the coloring reagents should reveal if identified actives are interfering with the assay readout.[38]

Table 1: Substrates for ATX-activity assays.

ATX substrate		Detectable product	References
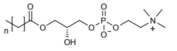 LPC [a]	⟶	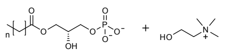	[32] [33] [34] [35] [37]
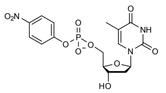 pNP-TMP	⟶	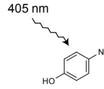	[3] [25]
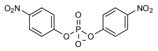 Bis-pNPP	⟶	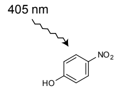	[33] [38]
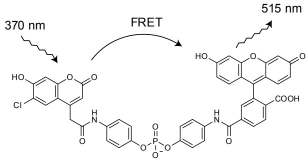 CPF4	⟶	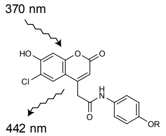 R = PO_3^{2-} or H	[33] [40]
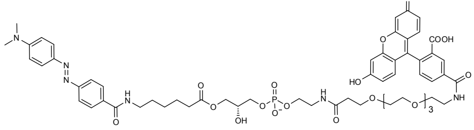 FS3	⟶	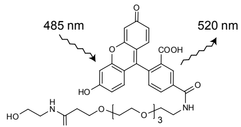	[41]
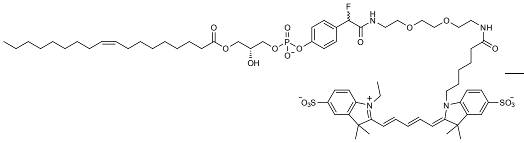 ATX-ABP	⟶	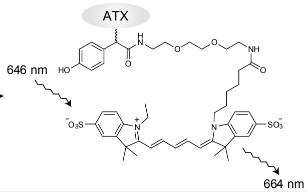	[42]

[a] LPA can be detected by radiometry or mass spectrometry. Choline can be detected in a two-step enzymatic colorimetric reaction.

1.4.2 Unnatural ATX substrate-based assays

As a member of the ecto-nucleotide pyrophosphatase and phosphodiesterase (ENPP) family, ATX also hydrolyzes nucleotides. Therefore, the nucleotide thymidine 5'-monophosphate para-nitrophenyl ester (pNP-TMP) can be used as an ATX substrate (Table 1).[3,25] Upon hydrolysis of pNP-TMP by ATX, 4-nitrophenol is released which has an absorbance at 405 nm and is detectable by colorimetry. The same product is formed when bis-para-nitrophenyl phosphate (bis-pNPP) is hydrolyzed by ATX (Table 1).[33,38] Bis-pNPP is a cheap ATX substrate that provides a direct readout.

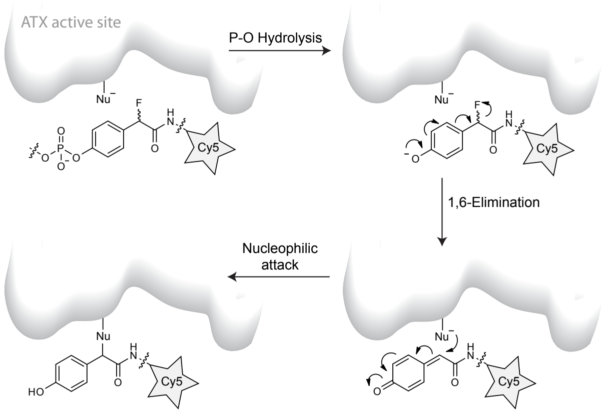

Scheme 2: Labeling mechanism of ATX with ATX-ABP. Only one of the potential labeled products resulting from the labeling is shown.

Another artificial ATX-substrate is CPF4, which has a similar core structure as bis-pNPP. In CPF4 the two nitro groups of bis-pNPP are replaced by coumarin and fluorescein (Table 1).[33,40] When the coumarin donor group in CPF4 is excited Förster fluorescence resonance energy transfer (FRET) between coumarin and the fluorescein acceptor occurs. After hydrolysis the FRET pair is separated and FRET is lost, providing a very sensitive assay reagent. Although this reagent was originally developed for phosphodiesterase I[40] it provides a very sensitive ATX activity sensor as well.[33]

FS3 is another synthetic ATX substrate, which is based on LPC (Table 1).[41] In this substrate a dabcyl moiety, a quencher of fluorescein, is connected *via* a lipid backbone to fluorescein. The fluorescein moiety in FS3 is quenched by the dabcyl moiety and becomes fluorescent when FS3 is hydrolyzed by ATX. A common advantage of the above mentioned assays is that they provide a realtime readout allowing direct kinetic studies of ATX activity.

In addition, a first generation ATX activity-based probe (ATX-ABP) has been reported (Table 1).[42] This probe makes use of the activity of ATX to label ATX covalently. Upon the hydrolysis of the phosphodiester bond in ATX-ABP, the released intermediate undergoes an 1,6-elimination of a fluoride atom (Scheme 2). This generates a reactive quinone methide species that traps nearby nucleophiles in the ATX active site resulting in covalent labeling of ATX with a fluorescent Cy5 dye in an activity-dependent manner. This ATX-ABP is able to label all the three known ATX isoforms.[42] In addition, ATX-ABP can label ATX in human plasma, however, an additional affinity-purifying step with an anti-ATX monoclonal antibody is required to make Cy5 labeled ATX detectable. Further development of this type of probes could turn them into diagnostic reagents to monitor ATX activity in complex samples such as body fluids.

1.5 Inhibitory effect of metal chelators on ATX activity

L-histidine has been reported as the first *in vitro* 'ATX inhibitor' with millimolar IC_{50} values for ATX using LPC or pNP-TMP as assay substrate.[43] It acts by scavenging metal ions in solution, such as zinc, which are essential for ATX activity. In addition, other metal chelating agents such as ethylenediaminetetraacetic acid (EDTA) and 1,10-phenanthroline also have an inhibitory effect on ATX activity.[43]

1.6 Natural lipids and lipid-based inhibitors of ATX

A distinct class of ATX inhibitors are based on lipids. The discovery of product inhibition of ATX by its lipid products LPA and S1P[33] triggered the development of lipid-based ATX inhibitors (Table 2). One class of lipid-based inhibitors includes thiophosphates.[44-46] An example of this class is thiophosphate **3** (IC_{50} = 0.6 µM, bis-pNPP) depicted in Table 2. The reported thiophosphates also act as agonists or antagonists for LPA_{1-3} receptors.[44-46] This is a general danger of lipid-based ATX inhibitors, that they may act on downstream LPA/S1P receptors due to their structural similarity with LPA and S1P.

There is also a class of ATX inhibitors based on cyclic phosphatidic acid (cPA) which is a naturally occurring analog of LPA where the *sn*-2 hydroxy group forms a 5-membered ring with the *sn*-3 phosphate.[47,48] cPA analog **4** (Table 2, IC_{50} = 0.14 µM, bis-pNPP) has no significant agonist activity at LPA receptors. Recently, a sulfur analog of cPA, 3-*O*-thia-cPA (**5**) has been reported as ATX inhibitor (Table 2).[49]

Another class of lipid-based ATX inhibitors is based on α-bromomethylene phosphonates like BrP-LPA (**6**, Table 2).[50,51] In addition, phosphonate **6** acts as a pan LPA_{1-4} receptor antagonist. α-Bromobenzyl phosphonates are well known protein tyrosine phosphatase inhibitors that target the active site covalently.[52] Whether phosphonate **6** inhibits ATX in a covalent manner is unknown. An inhibitor that is expected to bind ATX covalently is flouromethylphenyl phosphate **7** (Table 2).[53] The binding mechanism of **7** with ATX is postulated to be the same as for the ATX-ABP as depicted in Scheme 2.

Interestingly, phosphorylated FTY720 (FTY720-P, **8**, Table 2) inhibits ATX with a K_i of 0.2 µM using pNP-TMP as an ATX assay substrate.[54,55] FTY720-P is a synthetic analog of S1P and acts as an $S1P_1$ receptor antagonist (EC_{50} = 5 nM)[55] that activates this receptor, causing its internalization and subsequent polyubiquitination leading to proteasomal degradation of the $S1P_1$ receptor. This results in unresponsiveness of lymphocytes to S1P.[56]

Potencies of the previously described lipid-based inhibitors all have been determined in assays using unnatural and different ATX substrates (bis-pNPP, pNP-TMP, CPF4 and FS3) as reporter molecules. Therefore it is difficult to compare potencies of distinct inhibitors measured in different assays. In addition, inhibitors in these assays that use unnatural substrates of ATX might have no effect on LPC hydrolysis by ATX due to alternate binding of the substrate. Using assays based on LPC hydrolysis gives a direct answer if ATX inhibitors could inhibit LPA production by ATX. The most potent (IC_{50} = 5.6 nM, LPC) lipid-based inhibitor measured in an LPC hydrolysis assay is S32826 (**9**, Table 2).[39,57,58] This phosphonate inhibitor is a result of screening 13,000 small molecules for their ability to inhibit ATX. Unfortunately, the poor *in vivo* stability and/or bioavailability of the compound did not permit further use in animal models. A last lipid-like inhibitor class is based on a tyrosine building block and an example of this class is inhibitor **10**, which has a micromolar potency (K_i = 1.0 µM, LPC, Table 2).[59-61]

A frequently observed phenomenon for ATX inhibitors is their incapability to fully inhibit ATX. Examples are inhibitors **3**, **4** and **9** depicted in Table 2 that have residual ATX activity (RA) for ATX.

Table 2: Lipid and lipid-based inhibitors of ATX.

Entry	Inhibitor	Substrate	Activity	References [a]
1	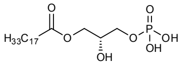 LPA	CPF4	K_i = 0.11 µM	[33]
2	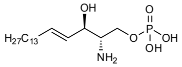 S1P	CPF4	K_i = 0.05 µM	[33]
3	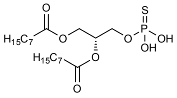 Thiophosphate	Bis-pNPP	IC_{50} = 0.60 µM RA = 27% [b]	[44] [45] [46]
4	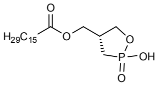 cPA-based	Bis-pNPP	IC_{50} = 0.14 µM RA = 9%	[47] [48]
5	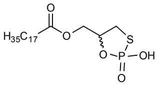 3-*O*-thia-cPA	FS3	PI = 55% @ 10 µM [c]	[49]
6	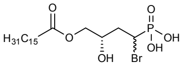 BrP-LPA	FS3	PI = 94% @ 10 µM	[50] [51]
7	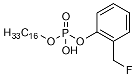 Fluoromethylphenyl	FS3	PI = 95% @ 3 µM	[53]
8	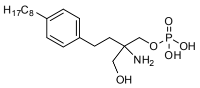 FTY720-P	pNP-TMP	K_i = 0.2 µM	[54] [55]
9	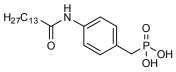 S32826	LPC	IC_{50} = 5.6 nM RA ≈ 10%	[39] [57] [58]
10	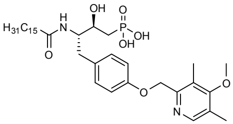 Tyrosine-based	LPC	K_i = 1.0 µM	[59] [60] [61]

---

[a] First reference corresponds with displayed structure the following references refer to similar inhibitor structures. [b] RA; residual ATX activity. [c] PI; percentage inhibition.

1.7 Small molecule inhibitors of ATX

Since 2008 many small molecule inhibitors have been reported in both academic and patent literature (Table 3). The most potent inhibitor (IC_{50} = 1.7 nM, LPC) reported to date is PF-8380 (**11**).[62,63] Interestingly, this compound reported by employees of Pfizer[62] is based on an inhibitor described in a Merck KGaA patent application.[63] Due to the high potency and favorable pharmacokinetic properties, PF-8380 is a suitable tool compound for *in vivo* evaluation of ATX inhibition.

Another very potent ATX inhibitor is the boronic acid HA155 (**12**, IC_{50} = 5.7 nM, LPC, Table 3), which is described in more detail in Chapter 3 of this thesis.[36,38] This molecule resulted from screening ~40,000 small molecules followed by medicinal chemistry efforts on the resulting screening hit. In the original screening hit a carboxylic acid moiety was replaced by a boronic acid moiety, designed to target the threonine oxygen nucleophile in the ATX active site. HA130,[36,38] a positional boronic acid isomer of HA155 that is described in Chapter 2 and 3, together with PF-8380 are the only two inhibitors to date that have been demonstrated to lower LPA levels *in vivo* (rat or mice).

Recently, other boronic acid-based inhibitors have been reported[64] as a result of a structure-based study resulting in *E*-**28** (**13**, Table 3), a potent inhibitor of ATX (IC_{50} = 5.3 nM, LPC). This study is described in Chapter 4 of this thesis.

A common feature of the three most potent inhibitors reported so far (**11**-**13**, Table 3) is that they share a long linear and flexible structure, which is also reflected in the structure of LPC and LPA. Probably this structural feature helps the inhibitors to accommodate to the lipid binding site since they bind to the ATX active site. Most of the other reported small molecules inhibitors lack this structural feature.

Several Merck KGaA patent applications claim ATX inhibitors (**15**-**18**) with *in vitro* potencies between 0.1 and 10 µM (LPC).[65-71] Structural diversity of these inhibitors is large as can be judged from Table 3.

Screening a phosphodiesterase targeted inhibitor library revealed that Vinpocetin (**19**, Table 3), a PDE type 1 inhibitor (IC_{50} = 8-50 µM), inhibits ATX with an IC_{50} value of 122 µM using LPC as a substrate.[72] In addition, screening a second library consisting of kinase inhibitors known to target the ATP binding site in kinases resulted in the discovery of Damnacanthal (**20**, Table 3), a $p56^{lck}$ tyrosine kinase inhibitor (IC_{50} = 17-620 nM), as ATX inhibitor (IC_{50} = 139 µM, LPC).[72]

Several ATX screening programs used libraries from the National Cancer Institute (NCI). This led for example to the discovery of arsenic acid NSC-48300 (**21**, Table 3) as ATX inhibitor, reported by two independent groups.[38,73,74] It is a competitive inhibitor which could suggest that the arsenic acid moiety in **21** acts as a non-hydrolyzable phosphate mimic. In addition, NSC-9616 (**22**, Table 3) has been identified as ATX inhibitor from screening an NCI library.[75]

The first virtual screen for ATX inhibitors led to the discovery of H2L-7905958 (**23**, Table 3).[76] This inhibitor has a K_i value of 1.9 µM (FS3) for ATX.[77] At the time of this virtual

Table 3: Activities of small molecule inhibitors of ATX.

Entry	Inhibitor	Substrate	Activity	References [a]
11	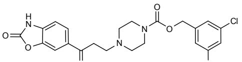 PF-8380	LPC	IC_{50} = 1.7 nM	[62] [63]
12	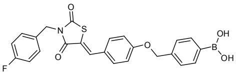 HA155	LPC	IC_{50} = 5.7 nM	[36] [38]
13	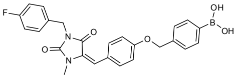 *E*-**28**	LPC	IC_{50} = 5.3 nM	[64]
14	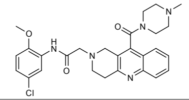	LPC	IC_{50} > 0.1 µM	[65] [66]
15	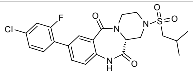	LPC	IC_{50} = 0.1-1 µM	[67] [68]
16	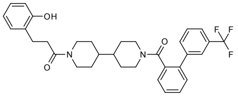	LPC	IC_{50} > 1 µM	[69]
17	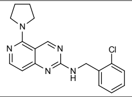	LPC	IC_{50} > 5 µM	[70]
18	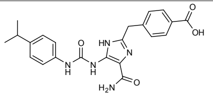	LPC	IC_{50} = 1-10 µM	[71]
19	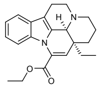 Vinpocetin	LPC	IC_{50} = 122 µM	[72]
20	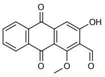 Damnacanthal	LPC	IC_{50} = 139 µM	[72]
21	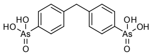 NSC-48300	FS3	K_i = 0.240 µM	[38] [73] [74]
22	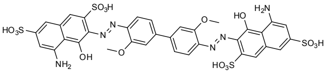 NSC-9616	FS3	K_i = 0.271 µM	[75]
23	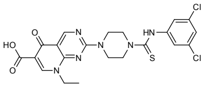 H2L-7905958	FS3	K_i = 1.9 µM	[76] [77]
24	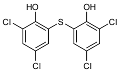 Bithionol	FS3	K_i = 66 µM	[73] [74]

[a] First reference corresponds with displayed structure the following references refer to similar inhibitor structures.

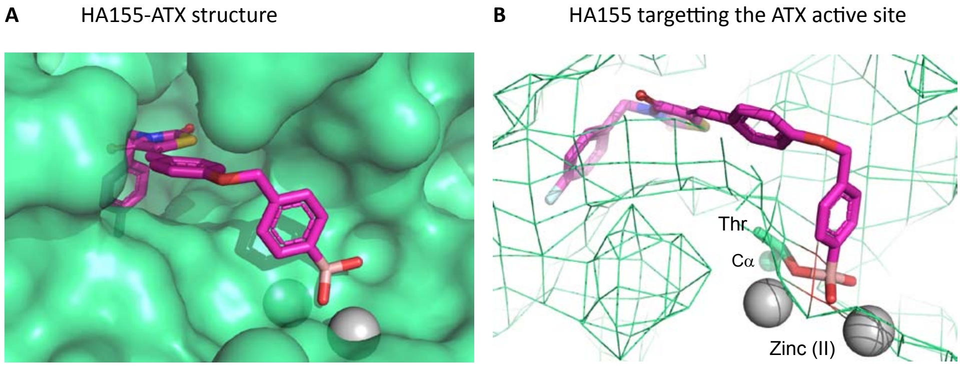

A HA155-ATX structure

B HA155 targetting the ATX active site

Figure 2: The inhibitor HA155 liganded ATX structure (PD ID 2XRG). (A) Binding of HA155 with ATX. (B) Boronic acid in HA155 targeting the threonine (Thr) oxygen nucleophile and two zinc ions in the ATX active site.

screen the ATX structure was not resolved. Therefore, the authors generated a homology model of ATX based on a *X. axonopodis p*V. *citri* (*Xac*) ENPP structure and used this homology model for virtual screening. Recently, a follow-up study has been reported describing new analogs of **23**.[77]

Another ATX inhibitor is bithionol (**24**, Table 3),[73,74] a known metal ion chelating molecule like L-histidine and EDTA.[78] The latter two inhibit ATX by scavenging metal ions in solution, which are required for ATX activity. However, inhibitor **24** appears to act directly on ATX and not *via* metal chelation since the K_i value of **24** for ATX is two orders of magnitude lower than the used metal ion concentration.

1.8 ATX structure and inhibitor design

In 2011, the crystal structure of ATX has been resolved independently by two groups.[26,79] Next to the unliganded ATX structure, structures of ATX with different species of LPA[26] and the inhibitor HA155 liganded ATX structure[79] have been reported. Binding of HA155 to the ATX active site is predominately driven by hydrophobic interactions and by a boronic acid moiety binding to the threonine oxygen nucleophile in the ATX active site (Figure 2A and B).[79] The latter binding was predicted because the boronic acid moiety in HA155 was designed and introduced to target the threonine oxygen nucleophile in the ATX active site. In addition, the ATX-HA155 structure showed that one of the boronic acid hydroxyl moieties is simultaneously tethered by the two zinc ions in the ATX active site (Figure 2B). Therefore, the boronic acid moiety not only targets the threonine oxygen nucleophile but also the two zinc ions that are essential for catalytic activity of ATX. Another feature of HA155 binding to the ATX active site is that its 4-fluorobenzyl moiety binds to the hydrophobic lipid binding pocket of ATX (Figure 2A), preventing that the alkyl chain of the lipid binds to this pocket.[26,79]

The ATX structure liganded with HA155 triggered an ATX structure-based inhibitor design, which is described in Chapter 4 of this thesis.[64] This study led to *E*-**28** (IC_{50} = 5.3 nM, LPC, Table 3) a hydantoin analog of HA155 (IC_{50} = 5.7 nM, LPC, Table 3). Remarkably, *E*-**28** is an *E*-isomer while HA155 is a *Z*-isomer. To understand how *E*-**28** binds to ATX, molecular docking experiments were performed, which suggested a binding pose for *E*-**28** different from that of the original binding pose of HA155 or from the *Z*-isomer of **28** for ATX. This study predicted that the 4-fluorobenzyl moiety in HA155 and *E*-**28** binds differently to the hydrophobic pocket in ATX. This finding may be used to design new inhibitors that fully exploit the ATX hydrophobic pocket opening further options for inhibitor design.

1.9 Concluding remarks

ATX is an attractive therapeutic target for LPA-related diseases. In the past decade, several ATX inhibitors have been discovered and developed ranging from metal chelators, lipid and lipid-based inhibitors to small molecule inhibitors. Over the last three years many patents on ATX inhibitors have appeared from pharmaceutical industry and academia emphasizing the interest on ATX as drug target. Finally, the recently reported crystal structure of ATX will aid medicinal chemistry efforts to further develop ATX inhibitors into therapeutic agents.

1.10 References

1. Stracke, M. L. et al. Identification, purification, and partial sequence analysis of autotaxin, a novel motility-stimulating protein. *J. Biol. Chem.* **267**, 2524-2529 (1992).
2. Stefan, C. Jansen, S. & Bollen, M. Modulation of purinergic signaling by NPP-type ectophosphodiesterases. *Purinergic. Signal* **2**, 361-370 (2006).
3. Tokumura, A. et al. Identification of human plasma lysophospholipase D, a lysophosphatidic acid-producing enzyme, as autotaxin, a multifunctional phosphodiesterase. *J. Biol. Chem.* **277**, 39436-39442 (2002).
4. Umezu-Goto, M. et al. Autotaxin has lysophospholipase D activity leading to tumor cell growth and motility by lysophosphatidic acid production. *J. Cell Biol.* **158**, 227-233 (2002).
5. Noguchi, K. Herr, D. Mutoh, T. & Chun, J. Lysophosphatidic acid (LPA) and its receptors. *Curr. Opin. Pharmacol.* **9**, 15-23 (2009).
6. Moolenaar, W. H. van Meeteren, L. A. & Giepmans, B. N. The ins and outs of lysophosphatidic acid signaling. *BioEssays* **26**, 870-881 (2004).
7. Sciorra, V. A. & Morris, A. J. Roles for lipid phosphate phosphatases in regulation of cellular signaling. *Biochim. Biophys. Acta* **1582**, 45-51 (2002).
8. Brindley, D. & Pilquil, C. Lipid phosphate phosphatases and signaling. *J. Lipid Res.* **50**, S225-S230 (2009).
9. Tanaka, M. et al. Autotaxin stabilizes blood vessels and is required for embryonic vasculature by producing lysophosphatidic acid. *J. Biol. Chem.* **281**, 25822-25830 (2006).
10. van Meeteren, L. A. et al. Autotaxin, a secreted lysophospholipase D, is essential for blood vessel formation during development. *Mol. Cell Biol.* **26**, 5015-5022 (2006).

11. Mills, G. B. & Moolenaar, W. H. The emerging role of LPA in cancer. *Nat. Rev. Cancer* **3**, 582-591 (2003).
12. Taghavi, P. et al. In vitro genetic screen identifies a cooperative role for LPA signaling and c-Myc in cell transformation. *Oncogene* **27**, 6806-6816 (2008).
13. Nam, S. W. et al. Autotaxin (ATX), a potent tumor motogen, augments invasive and metastatic potential of ras-transformed cells. *Oncogene* **19**, 241-247 (2000).
14. Liu, S. et al. Expression of autotaxin and lysophosphatidic acid receptors increases mammary tumorigenesis, invasion, and metastases. *Cancer Cell* **15**, 539-550 (2009).
15. Boucharaba, A. et al. Platelet-derived lysophosphatidic acid supports the progression of osteolytic bone metastases in breast cancer. *J. Clin. Invest.* **114**, 1714-1725 (2004).
16. Lin, S. et al. The absence of LPA2 attenuates tumor formation in an experimental model of colitis-associated cancer. *Gastroenterology* **136**, 1711-1720 (2009).
17. Kanda, H. et al. Autotaxin, an ectoenzyme that produces lysophosphatidic acid, promotes the entry of lymphocytes into secondary lymphoid organs. *Nat. Immunol.* **9**, 415-423 (2008).
18. Pradere, J. P. et al. LPA1 receptor activation promotes renal interstitial fibrosis. *J. Am. Soc. Nephrol.* **18**, 3110-3118 (2007).
19. Tager, A. et al. The lysophosphatidic acid receptor LPA1 links pulmonary fibrosis to lung injury by mediating fibroblast recruitment and vascular leak. *Nat. Med.* **14**, 45-54 (2008).
20. Pamuklar, Z. et al. Autotaxin/lysopholipase D and lysophosphatidic acid regulate murine hemostasis and thrombosis. *J. Biol. Chem.* **284**, 7385-7394 (2009).
21. Kremer, A. et al. Lysophosphatidic Acid Is a Potential Mediator of Cholestatic Pruritus. *Gastroenterology* **139**, 1008-1018 (2010).
22. Giganti, A. et al. Murine and human autotaxin α, β, and γ isoforms: Gene organization, tissue distribution, and biochemical characterization. *J. Biol. Chem.* **283**, 7776-7789 (2008).
23. Murata, J. et al. cDNA cloning of the human tumor motility-stimulating protein, autotaxin, reveals a homology with phosphodiesterases. *J. Biol. Chem.* **269**, 30479-30484 (1994).
24. Jansen, S. et al. Proteolytic maturation and activation of autotaxin (NPP2), a secreted metastasis-enhancing lysophospholipase D. *J. Cell Sci.* **118**, 3081-3089 (2005).
25. Gijsbers, R. Aoki, J. Arai, H. & Bollen, M. The hydrolysis of lysophospholipids and nucleotides by autotaxin (NPP2) involves a single catalytic site. *FEBS Lett.* **538**, 60-64 (2003).
26. Nishimasu, H. et al. Crystal structure of autotaxin and insight into GPCR activation by lipid mediators. *Nat. Struct. Mol. Biol.* **18**, 205-212 (2011).
27. Clair, T. et al. Autotaxin hydrolyzes sphingosylphosphorylcholine to produce the regulator of migration, sphingosine-1-phosphate. *Cancer Res.* **63**, 5446-5453 (2003).
28. Postma, F. R. Jalink, K. Hengeveld, T. & Moolenaar, W. H. Sphingosine-1-phosphate rapidly induces Rho-dependent neurite retraction: action through a specific cell surface receptor 9. *EMBO J.* **15**, 2388-2392 (1996).
29. Hla, T. Lee, M. Ancellin, N. Paik, J. & Kluk, M. Lysophospholipids-Receptor Revelations. *Science* **294**, 1875-1878 (2001).
30. Ishii, I. Fukushima, N. Ye, X. & Chun, J. Lysophospholipid Receptors: Signaling and Biology. *Annu. Rev. Biochem.* **73**, 321-354 (2004).
31. Spiegel, S. & Milstien, S. Sphingosine-1-phosphate: an enigmatic signalling lipid. *Nat. Rev. Mol. Cell Biol.* **4**, 397-407 (2003).

32. Tokumura, A. Miyake, M. Yoshimoto, O. Shimizu, M. & Fukuzawa, K. Metal-Ion stimulation and inhibition of lysophospholipase D which generates bioactive lysophosphatidic acid in rat plasma. *Lipids* **33**, 1009-1015 (1998).
33. van Meeteren, L. A. et al. Inhibition of autotaxin by lysophosphatidic acid and sphingosine 1-phosphate. *J. Biol. Chem.* **280**, 21155-21161 (2005).
34. Scherer, M. Schmitz, G. & Liebisch, G. High-Throughput Analysis of Sphingosine 1-Phosphate, Sphinganine 1-Phosphate, and Lysophosphatidic Acid in Plasma Samples by Liquid Chromatography-Tandem Mass Spectrometry. *Clin. Chem.* **55**, 1218-1222 (2009).
35. Murph, M. et al. *Methods in Enzymology Lipidomics and* Bioactive Lipids: Specialized Analytical Methods and Lipids in Disease. Brown, H. A. (ed.), pp. 1-25 (2007).
36. Albers, H. M. et al. Boronic acid-based inhibitor of autotaxin reveals rapid turnover of LPA in the circulation. *Proc. Natl. Acad. Sci. USA* **107**, 7257-7262 (2010).
37. Imamura, S. & Horiuti, Y. Enzymatic determination of phospholipase D activity with choline oxidase. *J. Biochem.* **83**, 677-680 (1978).
38. Albers, H. M. et al. Discovery and Optimization of Boronic Acid Based Inhibitors of Autotaxin. *J. Med. Chem.* **53**, 4958-4967 (2010).
39. Ferry, G. et al. S32826, A Nanomolar Inhibitor of Autotaxin: Discovery, Synthesis and Applications as a Pharmacological Tool. *J. Pharmacol. Exp. Ther.* **327**, 809-819 (2008).
40. Takakusa, H. et al. Design and Synthesis of an Enzyme-Cleavable Sensor Molecule for Phosphodiesterase Activity Based on Fluorescence Resonance Energy Transfer. *J. Am. Chem. Soc.* **124**, 1653-1657 (2002).
41. Ferguson, C. et al. Fluorogenic Phospholipid Substrate to Detect Lysophospholipase D/Autotaxin Activity. *Org. Lett.* **8**, 2023-2026 (2006).
42. Cavalli, S. et al. Development of an Activity-Based Probe for Autotaxin. *ChemBioChem* **11**, 2311-2317 (2010).
43. Clair, T. et al. L-histidine inhibits production of lysophosphatidic acid by the tumor-associated cytokine, autotaxin. *Lipids Health Dis.* **4**, 5 (2005).
44. Durgam, G. et al. Synthesis and pharmacological evaluation of second-generation phosphatidic acid derivatives as lysophosphatidic acid receptor ligands. *Bioorg. Med. Chem. Lett.* **16**, 633-640 (2006).
45. Durgam, G. et al. Synthesis, Structure-Activity Relationships, and Biological Evaluation of Fatty Alcohol Phosphates as Lysophosphatidic Acid Receptor Ligands, Activators of PPARγ, and Inhibitors of Autotaxin. *J. Med. Chem.* **48**, 4919-4930 (2005).
46. Gududuru, V. et al. Identification of Darmstoff analogs as selective agonists and antagonists of lysophosphatidic acid receptors. *Bioorg. Med. Chem. Lett.* **16**, 451-456 (2006).
47. Baker, D. et al. Carba Analogs of Cyclic Phosphatidic Acid Are Selective Inhibitors of Autotaxin and Cancer Cell Invasion and Metastasis. *J. Biol. Chem.* **281**, 22786-22793 (2006).
48. Gupte, R. et al. Synthesis and pharmacological evaluation of the stereoisomers of 3-carba cyclic-phosphatidic acid. *Bioorg. Med. Chem. Lett.* **20**, 7525-7528 (2010).
49. Tanaka, R. et al. Efficient synthesis of 3-O-thia-cPA and preliminary analysis of its biological activity toward autotaxin. *Bioorg. Med. Chem. Lett.* **21**, 4180-4182 (2011).
50. Prestwich, G. et al. Antitumor α–Chloro and α–Bromo phosphonate analogs of lysophosphatidic acid. (WO2008157361A1), 65pp. 24-12-2008. University of Utah Research Foundation, USA;

University of Tennessee Research Foundation. Ref Type: Patent

51. Jiang, G. et al. α-substituted phosphonate analogues of lysophosphatidic acid (LPA) selectively inhibit production and action of LPA. *ChemMedChem* **2**, 679-690 (2007).
52. Kumar, S. et al. Activity-based probes for protein tyrosine phosphatases. *Proc. Natl. Acad. Sci. USA* **101**, 7943-7948 (2004).
53. Parrill-Baker, A. Baker, D. & Montedonico, L. Preparation of fluoromethylphenyl phosphodiesters as mechanism-based inactivators of autotaxin. (WO2010040080A1), 38pp. 8-4-2010. USA. Ref Type: Patent
54. van Meeteren, L. Brinkmann, V. Saulnier-Blache, J. Lynch, K. & Moolenaar, W. Anticancer activity of FTY720: Phosphorylated FTY720 inhibits autotaxin, a metastasis-enhancing and angiogenic lysophospholipase D. *Cancer Lett.* **266**, 203-208 (2008).
55. Valentine, W. et al. (S)-FTY720-Vinylphosphonate, an analogue of the immunosuppressive agent FTY720, is a pan-antagonist of sphingosine 1-phosphate GPCR signaling and inhibits autotaxin activity. *Cell. Signalling* **22**, 1543-1553 (2010).
56. Oo, M. et al. Immunosuppressive and Anti-angiogenic Sphingosine 1-Phosphate Receptor-1 Agonists Induce Ubiquitinylation and Proteasomal Degradation of the Receptor. *J. Biol. Chem.* **282**, 9082-9089 (2007).
57. Gupte, R. et al. Benzyl and Naphthalene Methylphosphonic Acid Inhibitors of Autotaxin with Anti-invasive and Anti-metastatic Activity. *ChemMedChem* **6**, 922-935 (2011).
58. Jiang, G. Madan, D. & Prestwich, G. Aromatic phosphonates inhibit the lysophospholipase D activity of autotaxin. *Bioorg. Med. Chem. Lett.* **21**, 5098-5101 (2011).
59. East, J. et al. Synthesis and structure-activity relationships of tyrosine-based inhibitors of autotaxin (ATX). *Bioorg. Med. Chem. Lett.* **20**, 7132-7136 (2010).
60. Cui, P. et al. Synthesis and biological evaluation of phosphonate derivatives as autotaxin (ATX) inhibitors. *Bioorg. Med. Chem. Lett.* **17**, 1634-1640 (2007).
61. Cui, P. McCalmont, W. Tomsig, J. Lynch, K. & Macdonald, T. α- and β-Substituted phosphonate analogs of LPA as autotaxin inhibitors. *Bioorg. Med. Chem.* **16**, 2212-2225 (2008).
62. Gierse, J. et al. A Novel Autotaxin Inhibitor Reduces Lysophosphatidic Acid Levels in Plasma and the Site of Inflammation. *J. Pharmacol. Exp. Ther.* **334**, 310-317 (2010).
63. Schiemann, K. Schultz, M. Blaukat, A. & Kober, I. Preparation of piperidines and piperazines as antitumor agents. (WO2009046841A2), 152pp. 16-4-2009. Merck Patent GmbH, Germany. Ref Type: Patent
64. Albers, H. M. et al. Structure-Based Design of Novel Boronic Acid-Based Inhibitors of Autotaxin. *J. Med. Chem.* **54**, 4619-4626 (2011).
65. Staehle, W. Kober, I. Schiemann, K. Schultz, M. & Wienke, D. Preparation of benzo[b][1,6] naphthyridines as inhibitors of autotaxin for the treatment of tumors. (WO2010060532A1), 142pp. 3-6-2010. Merck Patent GmbH, Germany. Ref Type: Patent
66. Staehle, W. Kober, I. Schiemann, K. Schultz, M. & Wienke, D. Preparation of benzo[b][1,6] naphthyridines as inhibitors of autotaxin for the treatment of tumors. (DE102008059578A1), 66pp. 10-6-2010. Merck Patent GmbH, Germany. Ref Type: Patent
67. Schultz, M. Schiemann, K. & Staehle, W. Heterocyclic compounds as autotaxin inhibitors and their preparation and use in the treatment of tumors. (WO2011006569A1), 218pp. 20-1-2011.

Merck Patent GmbH, Germany. Ref Type: Patent

68. Schultz, M. Schiemann, K. & Staehle, W. Heterocyclic compounds as autotaxin inhibitors and their preparation and use in the treatment of tumors. (DE102009033392A1), 109pp. 20-1-2011. Merck Patent GmbH, Germany. Ref Type: Patent
69. Schiemann, K. Schultz, M. & Staehle, W. Piperidine and piperazine derivatives as autotaxin inhibitors and their preparation and use for the treatment and prophylaxis of cancers and other autotaxin-mediated diseases. (WO2010115491A2), 179pp. 14-10-2010. Merck Patent GmbH, Germany. Ref Type: Patent
70. Schiemann, K. et al. Preparation of 2,5-diamino-substituted pyrido[4,3-d]pyrimidines as autotaxin inhibitors useful in treating cancer. (WO2010063352A1), 177pp. 10-6-2010. Merck Patent GmbH, Germany. Ref Type: Patent
71. Schultz, M. Schiemann, K. Botton, G. Blaukat, A. & Kober, I. Preparation of carbamoylimidazoles as anticancer agents. (WO2009046804A1), 163pp. 16-4-2009. Merck Patent G.m.b.H., Germany. Ref Type: Patent
72. Moulharat, N. Fould, B. Giganti, A. Boutin, J. & Ferry, G. Molecular pharmacology of adipocyte-secreted autotaxin. *Chem.-Biol. Interact.* **172**, 115-124 (2008).
73. Saunders, L. P. et al. Identification of small-molecule inhibitors of autotaxin that inhibit melanoma cell migration and invasion. *Mol. Cancer Ther.* **7**, 3352-3362 (2008).
74. Braddock, D. Small molecule inhibitors of autotaxin, and methods of use for the treatment of cancer. (WO2009151644A2), 82pp. 17-12-2009. Yale University, USA. Ref Type: Patent
75. North, E. J. et al. Pharmacophore Development and Application Toward the Identification of Novel, Small-Molecule Autotaxin Inhibitors. *J. Med. Chem.* **53**, 3095-3105 (2010).
76. Parrill, A. et al. Virtual screening approaches for the identification of non-lipid autotaxin inhibitors. *Bioorg. Med. Chem.* **16**, 1784-1795 (2008).
77. Hoeglund, A. et al. Optimization of a Pipemidic Acid Autotaxin Inhibitor. *J. Med. Chem.* **53**, 1056-1066 (2010).
78. Fogg, A. G. Gray, A. & Burns, D. T. Stability constants of metal complexes of bithionol, fenticlor and hexachlorophene. *Anal. Chim. Acta* **51**, 265-270 (1970).
79. Hausmann, J. et al. Structural basis of substrate discrimination and integrin binding by autotaxin. *Nat. Struct. Mol. Biol.* **18**, 198-204 (2011).

CHAPTER 2

Biological validation of a boronic acid-based inhibitor of autotaxin reveals rapid turnover of LPA in the circulation

Harald M.H.G. Albers, Anping Dong, Laurens A. van Meeteren, David A. Egan, Manjula Sunkara, Erica W. van Tilburg, Karianne Schuurman, Olaf van Tellingen, Andrew J. Morris, Susan S. Smyth, Wouter H. Moolenaar and Huib Ovaa, *Proceedings of the National Academy of Sciences of the United States of America* **2010**, *107*, 7257-7262.

Abstract. Autotaxin (ATX or ENPP2) is a secreted ecto-nucleotide pyrophosphatase/phosphodiesterase (ENPP) that functions as a lysophospholipase D to produce the lipid mediator lysophosphatidic acid (LPA), a mitogen, chemoattractant and survival factor for many cell types. The ATX-LPA axis has been implicated in angiogenesis, chronic inflammation and tumor progression, making this system an attractive target for therapy. However, potent and selective non-lipid inhibitors of ATX were not available at the beginning of this study. By screening a chemical library, thiazolidine-2,4-diones have been identified that selectively inhibit ATX-mediated LPA production both *in vitro* and *in vivo*. Inhibitor potency was a 100-fold increased (IC_{50} ~30 nM, HA130) after the incorporation of a boronic acid moiety, designed to target the active site threonine (T210) in ATX. Intravenous injection of this inhibitor into mice resulted in a rapid decrease in plasma LPA levels, indicating that turnover of LPA in the circulation is much more dynamic than previously appreciated. Thus, boronic acid-based small molecules hold promise as candidate drugs to target ATX.

2.1 Introduction

Autotaxin (ATX or ENPP2) is a secreted ecto-nucleotide pyrophosphatase/ phosphodiesterase (ENPP) originally isolated as an autocrine motility factor from melanoma cells.[1] ATX, a ~120 kDa glycoprotein, is unique amongst the ENPPs in that it functions as a lysophospholipase D (lysoPLD) that converts extracellular lysophosphatidylcholine (LPC) into the lipid mediator lysophosphatidic acid (LPA).[2-5] LPA acts on specific G protein-coupled receptors and thereby stimulates the migration, proliferation and survival of many cell types (Figure 1).[6,7] ATX is produced by various tissues and is the major LPA-producing enzyme in the circulation. Newly produced LPA is subject to degradation by membrane-bound lipid phosphate phosphatases (LPPs).[8,9] However, little is known about the dynamic regulation of steady-state LPA levels *in vivo*.

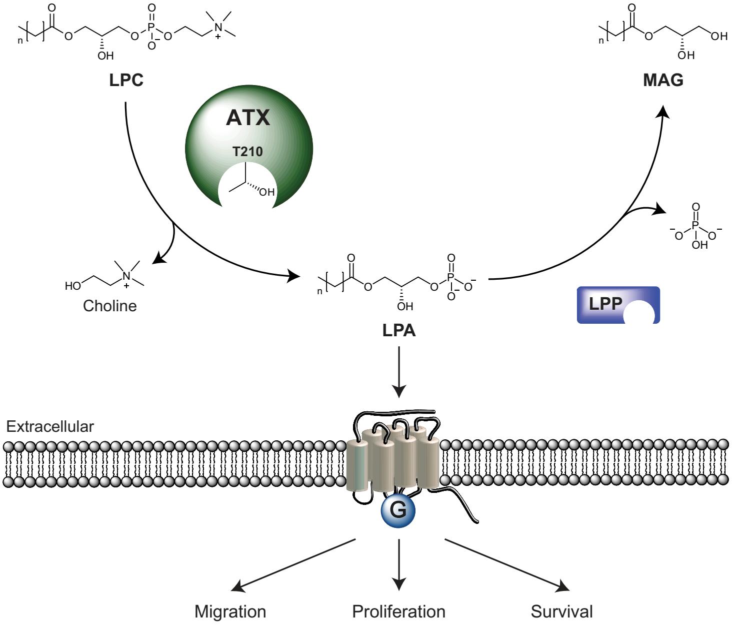

Figure 1: The ATX-LPA receptor signaling axis. Secreted ATX hydrolyzes extracellular LPC into LPA, a reaction catalyzed by active site residue T210. LPA signals through multiple G protein-coupled receptors to stimulate the proliferation, migration and survival of many cell types. LPA is degraded to monoacylglycerol (MAG) by lipid phosphate phosphatases (LPPs), which are membrane-bound ecto-enzymes.

ATX is essential for vascular development[10,11] and is found overexpressed in various human cancers.[12] Forced overexpression of ATX or individual LPA receptors promotes tumor progression in mouse models,[13-16] while LPA receptor deficiency protects from colon carcinogenesis.[17] In addition, to its role in cancer, ATX-LPA signaling has been implicated in lymphocyte homing and (chronic) inflammation,[18] fibrotic diseases[19,20] and thrombosis.[21] Therefore, the ATX-LPA axis qualifies as an attractive target for therapies.

Potent and selective ATX inhibitors are now needed as a starting point for the development of targeted anti-ATX/LPA therapy. Direct targeting of LPA receptors seems to be a less attractive strategy, since LPA acts on multiple receptors that show overlapping activities.[5,7] Since the initial finding that ATX is subject to product inhibition by LPA and sphingosine 1-phosphate (S1P),[22] various synthetic phosphate and phosphonate lipids have been explored as ATX inhibitors.[23-26] However, such lipid inhibitors have the inherent danger of inadvertently activating downstream LPA/S1P receptors, thereby inducing the opposite of the intended effect. Furthermore, lipids offer relatively few avenues for chemical diversification and usually have poor pharmacokinetic properties. Non-lipid inhibitors of ATX have recently been identified, but their potencies are low.[27]

In this study we screened small molecule libraries to search for novel ATX inhibitors. We identified thiazolidine-2,4-dione compounds that selectively inhibit ATX activity and are readily amenable to further chemical diversification. We have optimized these molecules by adopting an active site-targeted strategy that has proved successful for the development of the boronic acid-based proteasome inhibitor bortezomib,[28] which is in clinical use.[29] We show that a boronic acid-based inhibitor potently inhibits ATX both *in vitro* and *in vivo*. When administered to mice, our inhibitor (HA130) induces a remarkably rapid fall in plasma LPA levels, indicating that the turnover of circulating LPA is much more dynamic than previously appreciated. We conclude that boronic acid-based inhibitors hold promise as candidate drugs to target the ATX-LPA axis *in vivo*.

2.2 Discovery of small molecule inhibitors of ATX

The hydrolytic activity of ATX originates from a single catalytic site at threonine 210 (T210) in the central phosphodiester domain (Figure 1).[2] To discover novel ATX inhibitors, we screened a collection of ~40,000 drug-like small molecules using the hydrolysis of bis-*para*-nitrophenyl phosphate (bis-pNPP) by ATX as a readout. Among the most potent hits, we selected a

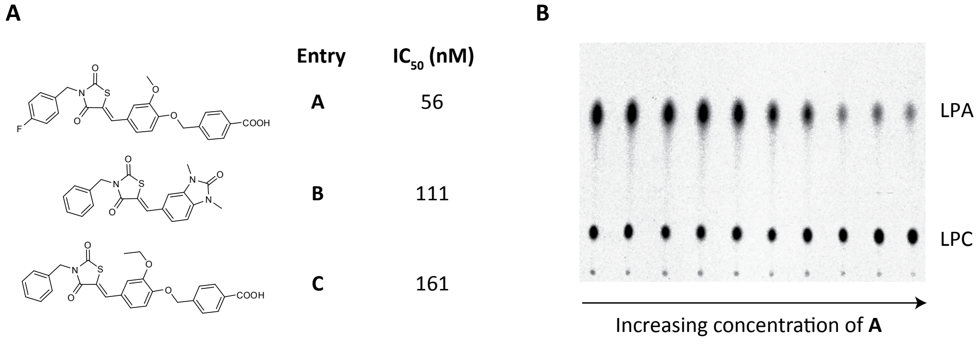

Entry	IC_{50} (nM)
A	56
B	111
C	161

Figure 2: ATX inhibitors discovered by high-throughput screening and validation of compound **A**. (A) IC_{50} values based on bis-pNPP (1 mM) hydrolysis. (B) TLC analysis of ^{14}C-LPC to ^{14}C-LPA conversion at different concentrations of **A** (range: 0-30 µM).

thiazolidine-2,4-dione series for optimization since the thiazolidine-2,4-dione core is readily amenable to chemical diversification (Figure 2A). Inhibitor **A** showed an IC_{50} value of 56 nM using 1 mM bis-pNPP as substrate. For validation of **A**, we measured the inhibition of the ATX-catalyzed release of choline from LPC. We established that recombinant ATX has a K_m value for LPC of 94 µM (Supporting Figure S1). Compound **A** inhibited ATX with an IC_{50} value of 2.5 µM using 40 µM LPC as a substrate (Figure 3A). However, it should be noted that **A** has a 35% residual ATX activity (Figure 3B). Inhibition of ATX-mediated LPA production was confirmed by measuring the conversion of ^{14}C-LPC to ^{14}C-LPA using thin-layer chromatography (Figure 2B).

2.3 Boronic acid-based optimization

Having identified compound **A** as a novel ATX inhibitor, we set out to improve its potency. We engineered a synthetic route (see Chapter 3), which allowed the synthesis and isolation of more than 100 derivatives of **A** in a short time frame.

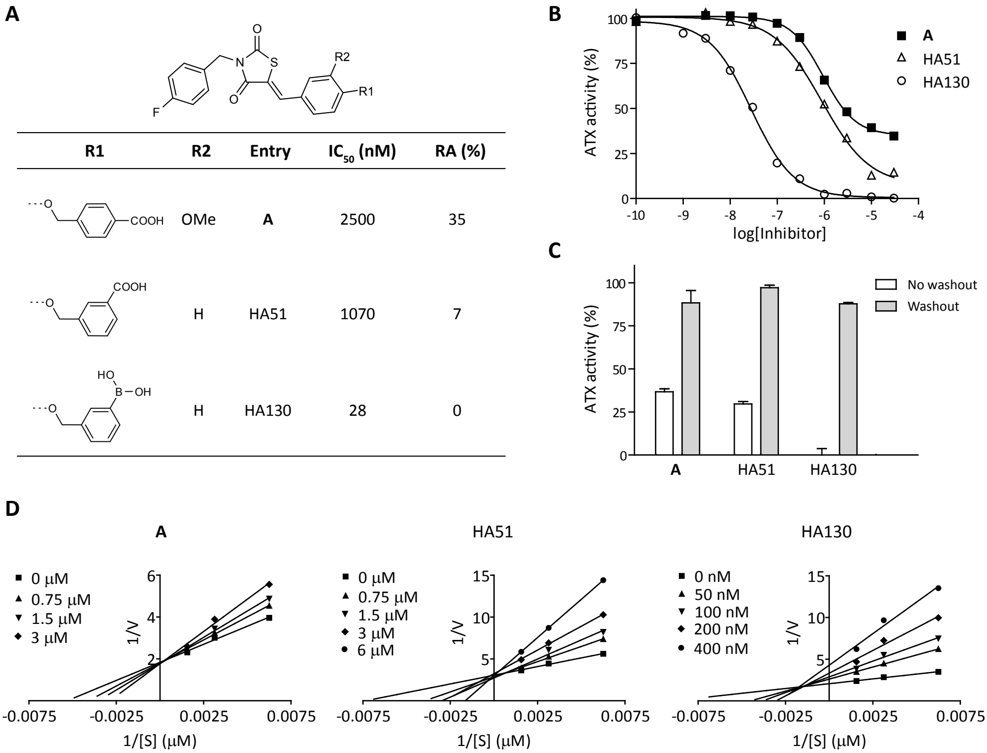

Figure 3: Analysis of ATX inhibition by compounds **A**, HA51 and boronic acid HA130, as measured by choline release from LPC (40 µM). (A) IC_{50} values and residual ATX activity (RA) for the three inhibitors tested. (B) Dose-inhibition curves for the inhibitors shown in (A). (C) Washout experiments showing that ATX inhibition is reversible. (D) Lineweaver-Burk plot analysis of ATX inhibition, showing competitive inhibition by **A** and HA51 and mixed-type inhibition by HA130.

All derivatives were tested in the ATX-mediated choline release assay. Figure 3A shows the IC_{50} values of the three most important molecules in the optimization process. Omitting the methoxy group and replacing the carboxylic acid to the *meta* position (HA51) resulted in a 2.5-fold increase in potency, concomitant with a significant drop in residual ATX activity, from 35 to 7% (Figure 3A and B). Lineweaver-Burk analysis revealed that **A** and HA51 act as competitive inhibitors (Figure 3D), suggesting that they bind at or close to the catalytic threonine residue (T210).

We next sought to target active site residue T210. We reasoned that the acid moiety of **A** and HA51 may bind to the phosphate ester acceptor site in ATX and that the T210 oxygen nucleophile could be targeted by a boronic acid moiety. Boronic acid is known for its high affinity for hard oxygen nucleophiles over soft nucleophiles, such as sulfur, which is found in many phosphate ester hydrolytic enzymes. This approach has an important precedent in the proteasome inhibitor and anti-cancer drug bortezomib (Velcade), which is a peptidyl boronic acid that targets the threonine oxygen nucleophile in the proteasome active site through its boronic acid moiety.[28,30] We adopted a similar approach to target the T210 oxygen nucleophile in ATX. This improves selectivity over phosphate ester hydrolyzing enzymes that depend on a sulfur (cysteine) nucleophile.

Replacing the carboxylic acid in HA51 by a boronic acid yielded compound HA130. This resulted in a ~100-fold increase in potency compared to screening hit **A** (IC_{50} = 28 nM) (Figure 3A). Furthermore, HA130 abolished the residual ATX activity observed with inhibitors **A** and HA51. Kinetic analysis revealed that HA130 is a mixed-type inhibitor, producing a reduction in V_{max} and an increase in K_m (Figure 3D). Thus, inhibition of ATX by HA130 results from a combination of a decreased turnover number and decreased affinity for its substrate. Washout of HA130 and the other inhibitors fully restored ATX activity, indicative of reversible inhibition (Figure 3C).

2.4 Selective inhibition of ATX

Since boronic acids can target the proteasome active site, we examined whether HA130 may affect proteasome activity. HA130 did not affect the chymotryptic, caspase and tryptic activities of the proteasome (Supporting Figure S2B). Conversely, bortezomib did not affect ATX activity. We next tested our inhibitors for selectivity against recombinant ENPP1, which is the closest relative of ATX, alkaline phosphatase (AP) and a broad-spectrum phosphodiesterase (PDE). None of these enzymes were affected by the ATX inhibitors at doses up to 10 µM (Supporting Figure S2A). Furthermore, cell viability was not compromised by HA130 (Supporting Figure S2C).

2.5 Inhibition of ATX-driven melanoma cell migration

ATX was originally identified as an autocrine motility factor for human A2058 melanoma cells.[1] We examined the ATX-mediated chemotactic migration of A2058 cells using a Boyden

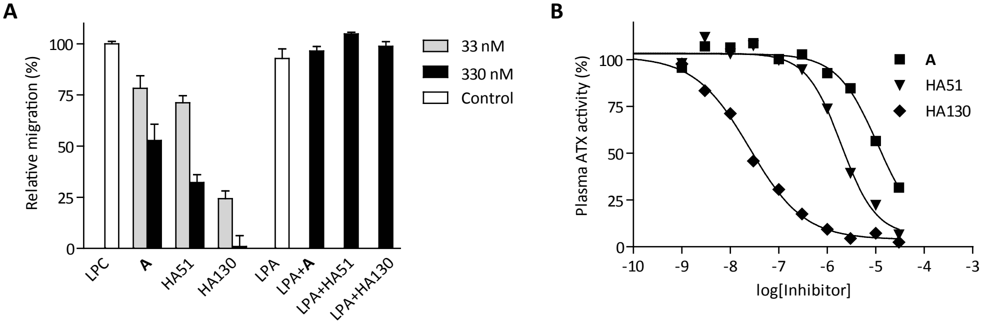

Figure 4: Effect of inhibitors on ATX-induced cell migration and on plasma ATX/lysoPLD activity. (A) ATX (1.2 nM), LPC (1 μM) and BSA (1 mg mL^{-1}) were added to the lower chambers of 48-wells Boyden chambers and the trans-well migration of A2058 melanoma cells was assayed after 4 h in the presence or absence of ATX inhibitors. None of the compounds inhibited LPA-induced cell migration (inhibitor and LPA added at 0.3 μM). (B) Inhibition of endogenous ATX/lysoPLD activity in human plasma *ex vivo*, as measured by choline release from LPC. Inhibition was maintained for at least 24 h (see Supporting Table S1).

chamber assay. ATX hydrolyzes exogenously added LPC into LPA, a potent chemoattractant for A2058 cells. As shown in Figure 4A, ATX inhibitors **A**, HA51 and HA130 inhibited ATX-mediated cell migration with increasing potencies. None of the inhibitors affected LPA-induced cell migration, indicating that they do not act on LPA receptor signaling pathways.

2.6 Inhibition of plasma ATX activity

ATX is identical to plasma lysoPLD[3,4] and responsible for virtually all LPA-producing activity in plasma and serum.[31] Inhibitors were tested for their ability to inhibit ATX/lysoPLD activity in human plasma *ex vivo*. As shown in Figure 4B, all three inhibitors were found to inhibit plasma ATX activity with the expected ranking order of potency. Inhibition of plasma ATX activity was long-lasting (24 h), indicating that HA130 is stable in plasma (Supporting Table S1).

2.7 HA130 decreases circulating LPA levels in mice

To investigate how ATX inhibition affects circulating plasma LPA levels, we administered HA130 (1 nmol g^{-1}) or vehicle as a single bolus injection into the jugular vein of anaesthetized mice. As a non-vehicle control we used compound HA51. Levels of HA130 or LPA in plasma samples rapidly isolated from venous blood were monitored before and after dosing. As shown in Figure 5A, intravenous administration of vehicle or HA51 (Supporting Figure S3) had little or no effect on plasma LPA levels. Following administration of HA130 (t = 10 min), plasma levels of the inhibitor rose rapidly to a concentration approaching 0.35 μM. This was accompanied by a parallel decrease in plasma LPA levels (3.8-fold) which returned slowly towards baseline as plasma levels of HA130 declined. Figure 5B shows summarized data from replicate experiments in which mice

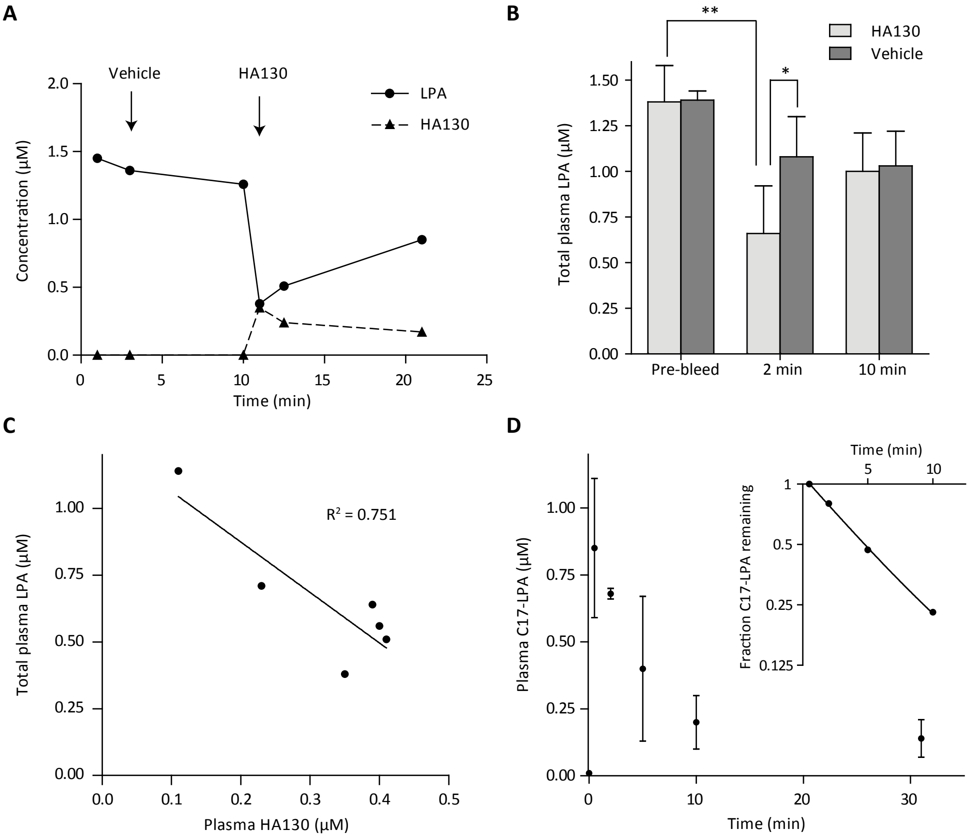

Figure 5: Effects of HA130 on circulating LPA levels in mice. (A) Vehicle or HA130 was administered intravenously into an anaesthetized mouse and plasma levels of the inhibitor or total LPA were determined at the indicated time points. Compound HA51 was used as a non-vehicle control (see Supporting Figure S3). (B) Plasma levels of LPA were determined at baseline and at 2 and 10 min post dosing of vehicle or HA130. The data shown are means +/- SD (6 mice treated with HA130; 5 mice treated with vehicle alone). The difference between baseline LPA levels and LPA levels at 2 min in HA130-treated mice are statistically significant ($p < 0.01$, **) by paired t-test. (C) Plasma levels of LPA and HA130 at 2 min post administration closely correlate ($R^2 = 0.751$). (D) C17-LPA (10 µL of a 10 mM solution in saline containing 0.1% fatty acid-free BSA) was injected into the jugular vein of anaesthetized mice and plasma levels of C17-LPA were determined at different time points. The inset shows a semi-log plot used to calculate the half-life for clearance of C17-LPA from the circulation. Data points are means +/- SD (n = 3).

were dosed with vehicle or HA130 while plasma LPA levels were measured before, 2 and 10 min post dosing (see also Supporting Figure S3). Administration of HA130 produced statistically significant decreases in plasma LPA levels compared to baseline, vehicle and HA51. The mean decrease in plasma LPA levels was 48% of the baseline control at 2 min post administration of HA130. Plasma HA130 levels correlated well ($R^2 = 0.751$) with plasma LPA levels (Figure

5C). Taken together, these findings suggest that continual production of LPA by ATX-catalyzed hydrolysis of circulating LPC is required to sustain plasma levels of LPA at their observed steady-state level. To confirm this, we injected C17-LPA and found that the levels of this unnatural LPA analog were elevated at the earliest measurable time point, but then decayed rapidly following pseudo first-order kinetics with a half-life of approximately 3 min (Figure 5D).

2.8 Discussion and conclusions

In this study we have identified and optimized a class of thiazolidine-2,4-dione compounds as potent and selective inhibitors of ATX that can reduce LPA plasma levels in mice. Our chemical optimization strategy was based on targeting the catalytic T210 residue in ATX by introducing a boronic acid moiety. Boronic acid has previously been shown to be instrumental in the anti-cancer drug bortezomib, which targets the threonine oxygen nucleophile in the active site of the proteasome.[30] Strikingly, replacing the carboxylic acid in HA51 by a boronic acid increased the potency for ATX inhibition by two orders of magnitude compared to the screening hit **A**. This boronic acid inhibitor named HA130 did not affect either ENPP1 or proteasome activity, which have both a catalytic threonine residue. Injection of HA130 into mice resulted in a rapid fall in circulating LPA levels, which is in keeping with the rapid degradation of intravenous administered C17-LPA observed in these animals. This result indicates that maintenance of steady-state LPA levels in plasma involves a highly dynamic balance between its ATX-mediated synthesis and its degradation by LPPs. Consistent with this, LPP1-deficient mice show a significantly reduced rate of [^{32}P]LPA degradation in the bloodstream.[32] Thus, ATX and LPPs are key determinants of LPA turnover *in vivo* and their activity balance sets the steady-state level of LPA in the circulation and, most likely, in the interstitial space.

Several questions concerning circulating ATX remain to be answered, including its tissue origin and metabolic fate, although recent evidence indicates that ATX is rapidly cleared from the circulation by liver sinusoidal endothelial cells.[33] Circulating ATX and LPA do not, of course, reflect the levels in intercellular spaces, since ATX is produced locally by many different cell types while the LPC substrate level in interstitial fluids is much lower than that in plasma. Another key question concerns how ATX activity is regulated under (patho) physiological conditions. Interestingly, ATX binds to activated lymphocytes and platelets in an integrin-dependent manner,[18,21] which could lead to altered catalytic activity and serve as a mechanism for localized LPA production at sites of inflammation and injury.

In conclusion, we have used a boronic acid-based inhibitor to demonstrate that ATX is a valid target for manipulating LPA levels *in vivo*. Further development of boronic acid inhibitors of ATX holds promise for therapeutic use in ATX/LPA-dependent pathologies, including chronic inflammation, tumor progression and fibrotic diseases.

2.9 Experimental section

Chemicals and enzymes. Small molecule libraries were obtained from the NCI and purchased from SPECS (Delft, The Netherlands). The compounds AN-988/40680277, AN-989/41697944 and AN-989/40746701 are all from the SPECS collection and are abbreviated by **A**, **B** and **C**, respectively. 1-Oleoyl-2-hydroxy-*sn*-glycero-3-phosphocholine (LPC, 18:1) and 1-heptadecanoyl-*sn*-glycero-3-phosphate (C17-LPA) were purchased from Avanti Polar Lipids. Horseradish peroxidase (HRP), choline oxidase and phosphodiesterase I from *Crotalus atrox* were obtained from Sigma-Aldrich. Alkaline phosphatase from calf intestine was from Roche. Radiolabeled LPC (1-[1-^{14}C]palmitoyl) was from Amersham Biosciences UK (specific activity 925 kBq mL^{-1}).

Recombinant ATX. HEK293 cells were transfected with the pcDNA3 vector containing a 6xHis-tagged human teratocarcinoma ATX sequence. After transfection, cells were washed and serum-free medium was added and cells were allowed to secrete His-tagged ATX into the culture medium for 48 h. Medium was collected and ATX was purified using TALON-affinity beads (Clontech) as described. Imidazole was removed by dialysis against Tris-buffered saline (140 mM NaCl, 5 mM KCl, 1 mM $CaCl_2$, 1 mM $MgCl_2$ and 50 mM Trizma, pH 8.0). Purity was verified by SDS-PAGE and Coomassie blue staining.

ATX/lysoPLD activity assay.[34] ATX/lysoPLD activity was measured by choline release from LPC (18:1) (40 µM) in 96-well plates. Inhibitors in DMSO were added to recombinant ATX (20 nM) in Tris-HCl buffer (pH 7.4) at 310 K. After 3 h of incubation, 50 µL ABTS (2 mM) and horseradish peroxidase (10 U mL^{-1}) were added to 50 µL of the reaction mixture. Choline oxidase (50 µL, 10 U mL^{-1}) was added for the colorimetric reaction. Absorbance was measured at 405 nm and data were analyzed using Graphpad Prism software. For a more detailed description of this assay see Experimental section Chapter 3.

Phosphodiesterase activity assays.[22] ATX activity toward bis-pNPP hydrolysis was determined as follows. Inhibitors in 2 µL DMSO were added to a 384-wells plate containing 24 µL ATX (~40 nM) in buffer (140 mM NaCl, 5 mM KCl, 1 mM $CaCl_2$, 1 mM $MgCl_2$, 50 mM Tris, pH 7.8) containing fatty acid-free BSA (0.2 mg mL^{-1}). Finally, 24 µL bis-pNPP (2 mM) was added to each well and the plate was incubated for 3 h at room temperature. Percentage inhibition (PI) was determined at a final concentration of 5 µM inhibitor. Absorbance was determined using a Perkin Elmer Envision plate reader (λ = 405 nm). ENPP1 activity was measured at an ENPP1 concentration of 180 nM. Reaction was carried out in 100 µL reaction buffer as described above and incubated at room temperature for 90 min. For PDE activity the same protocol was handed using 6 mU mL^{-1} of PDE incubating the reaction mixture at room temperature for 20 min. Graphpad Prism software was used for data analysis.

^{14}C-LPA formation. Incubations were carried out essentially as described in the choline release assay in the presence of 0.5 µM 1-[1-^{14}C]palmitoyl-LPC. Reactions were terminated by adding 150 µL 0.01 M acetic acid and 250 µL 1-butanol. After mixing and centrifugation, the 1-butanol phase was removed and the remaining water phase extracted with 1-butanol. The pooled butanol phases were washed and concentrated to dryness under vacuum. Reaction products were analyzed by thin layer chromatography (TLC). TLC plates were developed with $CHCl_3/MeOH/CH_3COOH/H_2O$ (50:30:8:4). Retardation factors for LPA and LPC were 0.5 and 0.13, respectively. Lipids were visualized by autoradiography.

Selectivity and toxicity. Alkaline phosphatase activity was determined by hydrolysis of bis-*para*-nitrophenyl phosphate (bis-pNPP). Inhibitors were added to 50 µl alkaline phosphate (0.4 U mL^{-1}) in 50 mM Tris-HCl (pH 8.5) containing 0.1 mM EDTA. 50 µL bis-pNPP (0.6 mM) was added to each well and the plate was incubated at room temperature for 1.5 h. Absorbance was determined at a wavelength of 405 nm.

Cell toxicity was determined using the CellTiter-Blue assay. Cells ($1.5x10^5$ mL^{-1}) were incubated with or without inhibitors for 24 h. Phenylarsine oxide (PAO) was used as a control for cell death. After 19 h of incubation, 20 µL of resazurin (0.125 mg mL^{-1}) was added for 5 h. Fluorescence was measured at $\lambda_{ex}/\lambda_{em}$ = 544/560 nm.

Proteasome activity. Purified bovine proteasome was preincubated with inhibitors for 30 min, followed by addition of AMC substrate.[35] Fluorescence was measured every 10 min during 1 hr after substrate addition at 310 K. 1 µg of bovine proteasome was added to assay buffer (25 mM Tris pH 7.4, 5 mM $MgCl_2$, 1 mM DTT, 1 mM ATP). AMC substrates used: 100 µM LLVY-AMC (chymotryptic activity), 40 µM LLE-AMC (caspase-like activity) and 60 µM VGR-AMC (tryptic activity). Controls used for proteasome inhibition were MG132 (25 µM) and epoxomicin (1 µM).

Human plasma ATX activity. Plasma ATX activity was measured in 96-wells plates using LPC (18:1) as a substrate. Heparin-treated human plasma (2 µL) was added to 38 µL Tris-HCl buffer (100 mM Tris-HCl, pH 9, 500 mM NaCl, 5 mM $MgCl_2$ and 0.05% Triton X-100). Subsequently, 0.8 µL inhibitor in DMSO was added. Finally, 40 µL of 2 mM LPC (18:1) in Tris-HCl buffer was added to each well and the plate was incubated at 310 K. The mixture with DMSO alone was used as a control. Plasma without added LPC was taken as control for endogenous LPA production. After 1.5 h of incubation, 150 µL homovanillic acid (2 mM) and horseradish peroxidase (1.6 U mL^{-1}) in Tris-HCl (0.01% Triton X-100, 20 mM $CaCl_2$ and 50 mM Tris-HCl, pH = 7.4) was added to 20 µL of the reaction mixture. Choline oxidase was added (40 µL, 4 U ml^{-1}) and fluorescence was determined at $\lambda_{ex}/\lambda_{em}$ = 320/450nm.

ATX-mediated cell migration. A2058 melanoma cell chemotaxis was assayed using 48-well Boyden chambers. Fibronectin-coated polycarbonate membranes (8 µM pores, NeuroProbe Inc.) were used to separate the upper from the lower chamber. The lower chamber contained DMEM with BSA (1 mg mL^{-1}), ATX (1.2 nM) and LPC (1 µM). Cells (0.75 x 10^6 mL^{-1}) were loaded in the upper wells and the chamber was incubated at 310 K for 4 h. Non-migrated cells were removed from the membrane and migrated cells were fixed and stained in Diff-Quick (Medion Diagnostics AG, Switzerland). The membrane was mounted on a glass slide and migrated cells were quantified.

Quantitation of HA130 by HPLC tandem mass spectrometry. HA130 was quantitated by HPLC tandem mass spectrometry using an ABI 4000 Q-Trap hybrid linear ion trap triple quadrupole mass spectrometer operating in triple quadrupole mode. The ion source settings were ion spray voltage +5500 V, declustering potential 126 V entrance potential 10 V ion spray voltage 5500 V, ion source temperature 823 K. Material was separated by reverse phase HPLC on an Agilent Eclipse XDB C8 column (4.6 × 150 mm, 5 µM), flow rate 0.5 mL min^{-1} with a step gradient of solvent A 75/25 methanol/water containing 0.5% formic acid and 0.1% ammonium formate, solvent B 99/1 methanol water containing 0.5% formic acid and 0.1% ammonium formate. HA130 was quantitated by selective reaction monitoring of precursor/product ion pairs with m/z 464/109, 464/135.1, 464/117.1 with optimized collision energies and colllision cell exit potentials for each ion pair. For analysis of HA130 in mouse plasma, material was extracted/deproteinated using acidified organic solvents as detailed below. Recovery of HA130 was estimated to be ~70%; values were corrected for recovery of the C17-LPA internal standard (see below).

Quantitation of LPA molecular species by HPLC tandem mass spectrometry. Whole blood was sampled and transferred directly into anticoagulant, centrifuged and plasma added directly to acidified organic solvents. After extraction, organic solvent soluble material was separated by reverse phase HPLC and 16 abundant LPA molecular species quantitated by tandem mass spectrometry using an ABI 4000 Q-Trap hybrid linear ion trap triple quadrupole mass spectrometer. Recovery was determined using C17-LPA as an internal standard and quantitation accomplished by reference to calibration curves determined using a series of synthetic LPAs that were independently quantitated by phosphorous analysis following wet digestion in perchloric acid.

Studies in mice. For intravenous administration, HA130 and HA51 in DMSO were diluted 10-fold into saline to give a drug concentration solution of 1 mM and a final DMSO concentration of 10%. This material was kept at 310 K and bath sonicated for 30 s immediately prior to intravenous administration. Male FVB mice were anaesthetized with isofluorane and dissected to expose the jugular vein. HA130 (1 µL g^{-1}, 1 mM) or vehicle were injected intravenously. HA51 served as a non-vehicle control. Whole blood was sampled from the jugular vein and collected directly into anticoagulant, mixed, centrifuged and plasma transferred to glass tubes containing acidified solvents for extraction of HA130 and LPA. All animal experiments conformed to the recommendations of the "Guide for the Care and Use of Laboratory Animals" (Department of Health, Education, and Welfare publication number NIH 78-23, 1996) and were approved by the institutional Animal Care and Use Committee.

Chemical synthesis inhibitors. See Chapter 3.

2.10 References

1. Stracke, M. L. et al. Identification, purification, and partial sequence analysis of autotaxin, a novel motility-stimulating protein. *J. Biol. Chem.* **267**, 2524-2529 (1992).
2. Stefan, C. Jansen, S. & Bollen, M. NPP-type ectophosphodiesterases: unity in diversity. *Trends Biochem. Sci.* **30**, 542-550 (2005).
3. Tokumura, A. et al. Identification of human plasma lysophospholipase D, a lysophosphatidic acid-producing enzyme, as autotaxin, a multifunctional phosphodiesterase. *J. Biol. Chem.* **277**, 39436-39442 (2002).
4. Umezu-Goto, M. et al. Autotaxin has lysophospholipase D activity leading to tumor cell growth and motility by lysophosphatidic acid production. *J. Cell Biol.* **158**, 227-233 (2002).
5. van Meeteren, L. & Moolenaar, W. Regulation and biological activities of the autotaxin-LPA axis. *Prog. Lipid Res.* **46**, 145-160 (2007).
6. Moolenaar, W. H. van Meeteren, L. A. & Giepmans, B. N. The ins and outs of lysophosphatidic acid signaling. *BioEssays* **26**, 870-881 (2004).
7. Noguchi, K. Herr, D. Mutoh, T. & Chun, J. Lysophosphatidic acid (LPA) and its receptors. *Curr. Opin. Pharmacol.* **9**, 15-23 (2009).
8. Brindley, D. & Pilquil, C. Lipid phosphate phosphatases and signaling. *J. Lipid Res.* **50**, S225-S230 (2009).
9. Sciorra, V. & Morris, A. Roles for lipid phosphate phosphatases in regulation of cellular signaling. *Biochim. Biophys. Acta, Mol. Cell Biol. Lipids* **1582**, 45-51 (2002).
10. Tanaka, M. et al. Autotaxin Stabilizes Blood Vessels and Is Required for Embryonic Vasculature by Producing Lysophosphatidic Acid. *J. Biol. Chem.* **281**, 25822-25830 (2006).

11. van Meeteren, L. A. et al. Autotaxin, a secreted lysophospholipase D, is essential for blood vessel formation during development. *Mol. Cell Biol.* **26**, 5015-5022 (2006).
12. Mills, G. B. & Moolenaar, W. H. The emerging role of lysophosphatidic acid in cancer. *Nat. Rev. Cancer* **3**, 582-591 (2003).
13. Boucharaba, A. et al. Platelet-derived lysophosphatidic acid supports the progression of osteolytic bone metastases in breast cancer. *J. Clin. Invest.* **114**, 1714-1725 (2004).
14. Liu, S. et al. Expression of Autotaxin and Lysophosphatidic Acid Receptors Increases Mammary Tumorigenesis, Invasion, and Metastases. *Cancer Cell* **15**, 539-550 (2009).
15. Nam, S. W. et al. Autotaxin (ATX), a potent tumor motogen, augments invasive and metastatic potential of ras-transformed cells. *Oncogene* **19**, 241-247 (2000).
16. Taghavi, P. et al. In vitro genetic screen identifies a cooperative role for LPA signaling and c-Myc in cell transformation. *Oncogene* **27**, 6806-6816 (2008).
17. Lin, S. et al. The Absence of LPA2 Attenuates Tumor Formation in an Experimental Model of Colitis-Associated Cancer. *Gastroenterology* **136**, 1711-1720 (2009).
18. Kanda, H. et al. Autotaxin, an ectoenzyme that produces lysophosphatidic acid, promotes the entry of lymphocytes into secondary lymphoid organs. *Nat. Immunol.* **9**, 415-423 (2008).
19. Pradère, J. et al. LPA1 Receptor Activation Promotes Renal Interstitial Fibrosis. *J. Am. Soc. Nephrol.* **18**, 3110-3118 (2007).
20. Tager, A. et al. The lysophosphatidic acid receptor LPA1 links pulmonary fibrosis to lung injury by mediating fibroblast recruitment and vascular leak. *Nat. Med.* **14**, 45-54 (2008).
21. Pamuklar, Z. et al. Autotaxin/lysopholipase D and Lysophosphatidic Acid Regulate Murine Hemostasis and Thrombosis. *J. Biol. Chem.* **284**, 7385-7394 (2009).
22. van Meeteren, L. A. et al. Inhibition of autotaxin by lysophosphatidic acid and sphingosine 1-phosphate. *J. Biol. Chem.* **280**, 21155-21161 (2005).
23. Cui, P. McCalmont, W. Tomsig, J. Lynch, K. & Macdonald, T. α- and β-Substituted phosphonate analogs of LPA as autotaxin inhibitors. *Bioorg. Med. Chem.* **16**, 2212-2225 (2008).
24. Ferry, G. et al. S32826, A Nanomolar Inhibitor of Autotaxin: Discovery, Synthesis and Applications as a Pharmacological Tool. *J. Pharmacol. Exp. Ther.* **327**, 809-819 (2008).
25. van Meeteren, L. Brinkmann, V. Saulnier-Blache, J. Lynch, K. & Moolenaar, W. Anticancer activity of FTY720: Phosphorylated FTY720 inhibits autotaxin, a metastasis-enhancing and angiogenic lysophospholipase D. *Cancer Lett.* **266**, 203-208 (2008).
26. Baker, D. et al. Carba Analogs of Cyclic Phosphatidic Acid Are Selective Inhibitors of Autotaxin and Cancer Cell Invasion and Metastasis. *J. Biol. Chem.* **281**, 22786-22793 (2006).
27. Parrill, A. et al. Virtual screening approaches for the identification of non-lipid autotaxin inhibitors. *Bioorg. Med. Chem.* **16**, 1784-1795 (2008).
28. Adams, J. et al. Potent and selective inhibitors of the proteasome: Dipeptidyl boronic acids. *Bioorg. Med. Chem. Lett.* **8**, 333-338 (1998).
29. Kropff, M. et al. Bortezomib in combination with intermediate-dose dexamethasone and continuous low-dose oral cyclophosphamide for relapsed multiple myeloma. *Br. J. Haematol.* **138**, 330-337 (2007).
30. Groll, M. Berkers, C. Ploegh, H. & Ovaa, H. Crystal Structure of the Boronic Acid-Based Proteasome Inhibitor Bortezomib in Complex with the Yeast 20S Proteasome. *Structure* **14**, 451-456 (2006).

31. Nakasaki, T. et al. Involvement of the Lysophosphatidic Acid-Generating Enzyme Autotaxin in Lymphocyte-Endothelial Cell Interactions. *Am. J. Pathol.* **173**, 1566-1576 (2008).
32. Tomsig, J. L. et al. Lipid phosphate phosphohydrolase type 1 (LPP1) degrades extracellular lysophosphatidic acid in vivo. *Biochem. J.* **419**, 611-618 (2009).
33. Jansen, S. et al. Rapid clearance of the circulating metastatic factor autotaxin by the scavenger receptors of liver sinusoidal endothelial cells. *Cancer Lett.* **284**, 216-221 (2009).
34. Cui, P. et al. Synthesis and biological evaluation of phosphonate derivatives as autotaxin (ATX) inhibitors. *Bioorg. Med. Chem. Lett.* **17**, 1634-1640 (2007).
35. Elliott, P. J. Soucy, T. A. Pien, C. S. Adams, J. & Lightcap, E. S. Assays for proteasome inhibition. *Methods Mol. Med.* **85**, 163-172 (2003).

2.11 Supporting information

Supporting Table S1: Inhibition of ATX activity in human plasma over time.

	PI (%) [a]			
	2h	**4h**	**8h**	**24h**
A	23	26	20	20
HA51	79	83	78	73
HA130	94	100	100	95

[a] Percentage inhibition (PI) by the three inhibitors (5 µM) was measured at the indicated time points. ATX inhibition was constant over 24 h.

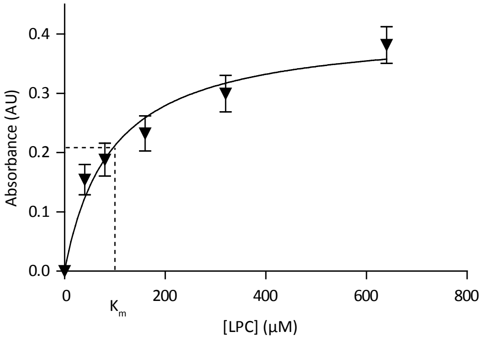

Supporting Figure S1: Saturation kinetics of ATX. Rates of choline release from LPC are plotted against increasing concentration of LPC. ATX activity data points (absorbance; arbitrary units (AU)) were fitted to the Michaelis-Menten equation, yielding an apparent K_m value for LPC of 95 µM (n=5).

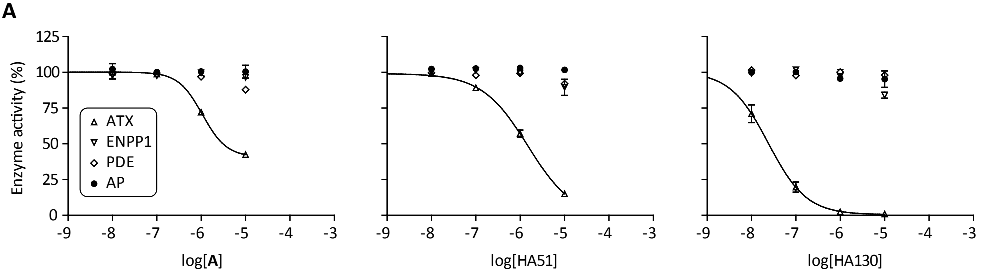

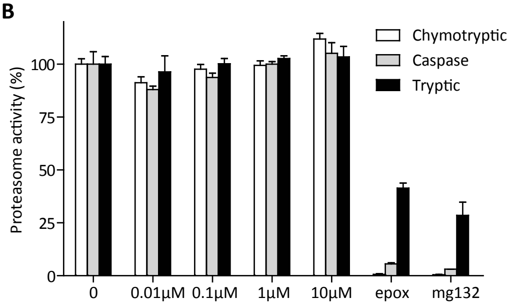

C

	TD$_{50}$ (µM)		
	A2058	**HEK293T**	**HepG2**
A	nt	nt	nt
HA51	nt	nt	nt
HA130	105	83	2056
PAO	0.22	0.16	0.39

Supporting Figure S2: Enzyme selectivity and toxicity of ATX inhibitors. (A) Lack of effect of ATX inhibitors on ENPP1, PDE and AP activity. (B) Lack of effect of HA130 (up to 10 µM) on the indicated proteasome activities. Proteasome inhibitors epoxomicin (epox) and MG132 were used as controls. (C) Toxic dose (TD$_{50}$) of ATX inhibitors for human A2058, HEK293T and HepG2 cells. Phenylarsine oxide (PAO) was used as a control for cell death (nt: no toxicity below 100 µM).

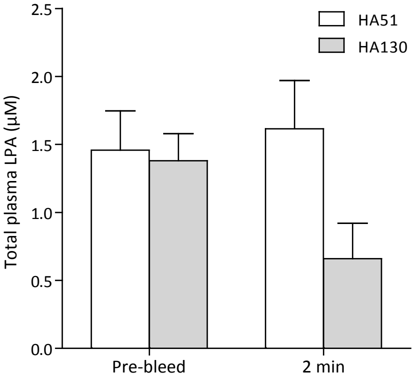

Supporting Figure S3: Plasma levels of LPA were determined before and 2 min post dosing of mice treated with HA51 (n=4) and HA130 (n=6). The data shown are means +/- SEM.

CHAPTER 3

Discovery and optimization of boronic acid-based inhibitors of autotaxin: *How did we exactly arrive at these inhibitors?*

Harald M.H.G. Albers, Laurens A. van Meeteren, David A. Egan, Erica W. van Tilburg, Wouter H. Moolenaar and Huib Ovaa, *Journal of Medicinal Chemistry* **2010**, *53*, 4958-4967.

Abstract. Autotaxin (ATX) is an extracellular enzyme that hydrolyzes lysophosphatidylcholine (LPC) to produce the lipid mediator lysophosphatidic acid (LPA). The ATX-LPA signaling axis has been implicated in diverse physiological and pathological processes, including vascular development, inflammation, fibrotic disease and tumor progression. Therefore, targeting ATX with small molecule inhibitors is an attractive therapeutic strategy. The previous chapter describes thiazolidine-2,4-diones that inhibit ATX activity in the micromolar range. Interestingly, inhibitory potency was dramatically increased by introduction of a boronic acid moiety, designed to target the active site threonine in ATX. Here the discovery and further optimization of boronic acid-based ATX inhibitors is described. The most potent of these compounds inhibits ATX-mediated LPC hydrolysis in the nanomolar range (IC_{50} = 6 nM). The finding that ATX can be targeted by boronic acids may aid the development of ATX inhibitors for therapeutic use.

3.1 Introduction

Autotaxin (ATX or ENPP2), originally isolated as an autocrine motility factor from melanoma cells, belongs to the ecto-nucleotide pyrophosphatase and phosphodiesterase (ENPP) family.[1-3] This extracellular enzyme acts as a lysophospholipase D, hydrolyzing lysophosphatidylcholine (LPC) into the lipid mediator lysophosphatidic acid (LPA), as depicted in Scheme 1.[4,5] Hydrolytic activity of ATX originates from a threonine (T210) residue in the active site.[1] LPA activates specific G protein-coupled receptors and thereby stimulates the migration, proliferation and survival of many cell types.[6]

The ATX-LPA axis has a vital role in vascular development.[7,8] Furthermore, it has been implicated in various pathologies including tumor progression[9] and metastasis,[10] inflammation[11] and fibrotic disease.[12] Given its role in human disease, the ATX-LPA axis is an obvious target for therapy. The fact that ATX is an extracellular enzyme makes it even more attractive as a drug target. Since there are at least six distinct LPA receptors, direct targeting of LPA receptors seems to be a less attractive strategy.[13,14] On the basis of the initial discovery that ATX is inhibited by LPA and sphingosine 1-phosphate (S1P) under certain conditions,[15] various synthetic phospholipid analogs have been explored as ATX inhibitors.[16-20] However, lipid-based inhibitors have the disadvantage that they could act as agonists or antagonists for any of the LPA/S1P receptors, thereby resulting in an effect opposite of the one intended. In addition, non-lipid ATX inhibitors have been identified, but their inhibitory potential is low ($IC_{50} \geq 1$ µM).[21-23]

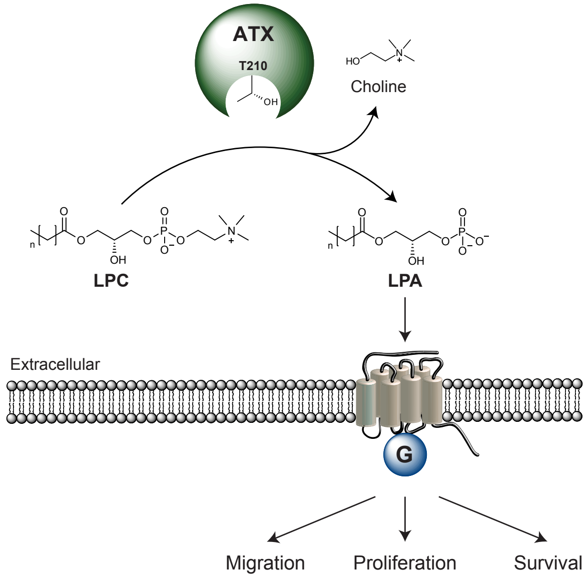

Scheme 1. The hydrolysis of LPC by ATX into LPA and choline. The lysoPLD reaction is catalyzed by a threonine oxygen nucleophile (T210). Newly produced LPA triggers subsequent biological events *via* activation of specific G protein-coupled receptors.

The previous chapter describes a non-lipid ATX inhibitor (HA130)[24] that rapidly lowers plasma LPA levels upon intravenous injection in mice. Using HA130 we found that the turnover of circulating LPA is much faster than expected, showing the usefulness of ATX inhibitors as tools to elucidate the role of ATX and LPA *in vivo*.

Here we describe the discovery and optimization of boronic acid-based inhibitors of ATX. We screened ~40,000 small molecules and identified thiazolidine-2,4-dione as ATX

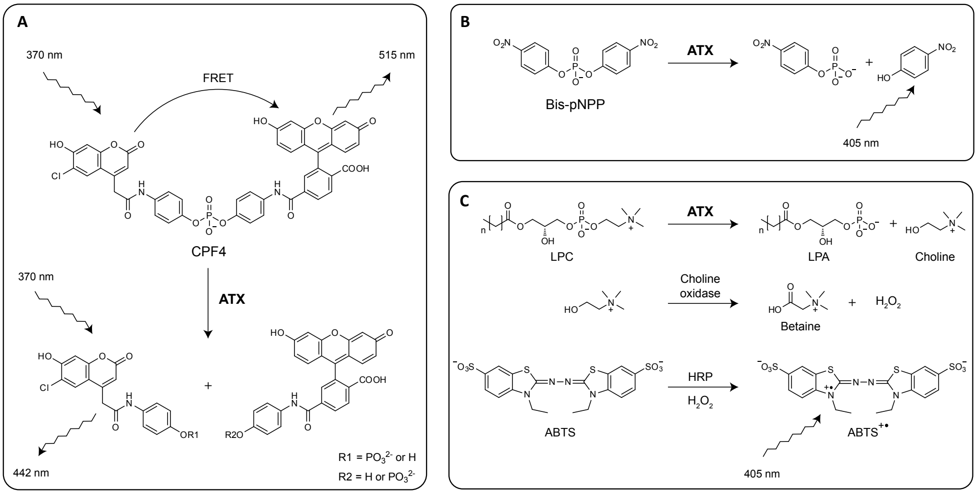

Figure 1. Three ATX assays used for screening and validation of ATX inhibitors. (A) CPF4 assay; This assay is based on Förster resonance energy transfer (FRET) between coumarin and fluorescein moieties of CPF4. (B) Bis-pNPP assay; In this assay bis-*para*-nitrophenyl phosphate (bis-pNPP) is hydrolyzed by ATX into the chromophore *para*-nitrophenol. (C) Choline release assay; The physiological substrate of ATX, LPC, is hydrolyzed by ATX to give LPA and choline. The release of choline can be detected in a two-step enzymatic coloring reaction.

inhibitors, which proved to be suitable to further chemical optimization. In particular, we optimized these molecules by first introducing small systematic variations in the structure of a screening hit, followed by the introduction of more random variations. Finally, by targeting the T210 oxygen nucleophile in ATX through a boronic acid, the potency of the original thiazolidine-2,4-dione screening hit was increased over 400-fold (IC_{50} = 6 nM).

3.2 ATX inhibitor screen

To identify ATX inhibitors, a small molecule screen was carried out. We first used a collection of 17,500 molecules from the National Cancer Institute (NCI) to optimize our screening protocol. This NCI library was initially screened using CPF4, an ATX activity reporter based on Förster resonance energy transfer (FRET) (Figure 1A).[15,25] The phosphodiester bond which links the coumarin and fluorescein moieties in CPF4 is hydrolyzed by ATX, resulting in the loss of FRET. Since we have shown that LPA can inhibit ATX activity in this assay, it was used as a positive control for ATX inhibition.[15] Approximately 250 active molecules were retested in a second assay using bis-*para*-nitrophenyl phosphate (bis-pNPP) as reporter substrate (Figure 1B).[15] In Supporting Figure S1 the results of both assays are compared. Only a few compounds remained after retesting in the bis-pNPP assay. Since the CPF4 assay resulted in many false positives, we decided to reverse the assay order. The same NCI library was tested in the bis-pNPP assay using CPF4 as confirmation tool which led to reproducible hits corresponding to the findings of Saunders *et al*.[26] Top three actives of the NCI screen can be found in Supporting Figure S2.

Structure	Entry	PI (%)		IC_{50} (nM)
		Bis-pNPP	*CPF4*	*Bis-pNPP*
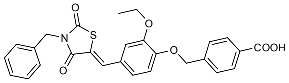	**1**	92	89	161
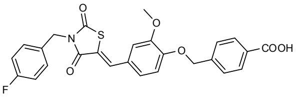	**2** (**A**)	91	85	56
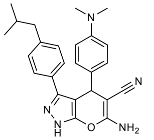	**3**	87	77	46
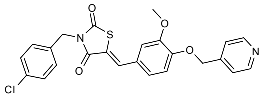	**4**	83	85	68
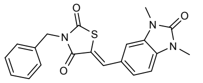	**5**	75	55	111
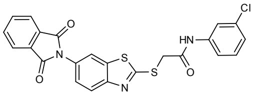	**6**	71	66	261
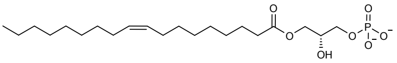	LPA	80	67	442

Figure 2. ATX inhibitors discovered by high-throughput screening. Percentage inhibition (PI) at 5 µM is based on the bis-pNPP or CPF4 assay. IC_{50} values are obtained using the bis-pNPP assay. LPA was used as a control for ATX inhibition.

After setting up our screening protocol, we used a commercial library (SPECS) consisting of 23,000 small molecules with predicted drug-like properties. For active molecules in this screen the percentage inhibition (PI) at 5 µM and IC_{50} values (bis-pNPP assay) are shown in Figure 2. These actives were confirmed by the CPF4 assay (Figure 2). Among the confirmed active molecules were several thiazolidine-2,4-diones (**1**, **2**, **4** and **5**), a pyrano pyrazole (**3**) and a benzothiazole (**6**). Because the thiazolidine-2,4-diones are well represented among the positive hits and their amenability to fast chemical diversification, the most potent thiazolidine-2,4-dione **2** (IC_{50} = 56 nM) was selected for further optimization.

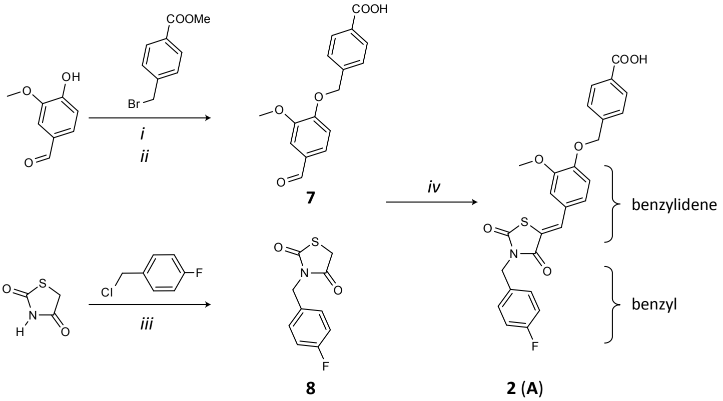

Scheme 2. Convergent synthetic route towards thiazolidine-2,4-dione **2** (**A**). *Reagents (i) KOH, DMSO, rt, 30 min. (ii) NaOH, DMSO/H_2O (1:3, v/v), reflux, 4 h, 91%. (iii) NaH, DMF, rt, 22 h, 74%. (iv) Piperidine, EtOH, reflux, 20 h, 63%.*

3.3 Chemistry

We next explored how to improve the potency of thiazolidine-2,4-dione **2** (compound **A** in Chapter 2) as an ATX inhibitor. We designed the convergent synthetic route toward inhibitor **2** depicted in Scheme 2. The synthesis requires benzoic acid **7** which can be obtained *via* a one-pot-synthesis. First, vanillin was *O*-alkylated with methyl-4-(bromomethyl) benzoate.[27] The resulting benzoate was hydrolyzed to give benzoic acid **7**. To afford the precursor **8**, thiazolidine-2,4-dione was dissolved in DMF and *N*-alkylated with 4-fluorobenzyl chloride in the presence of sodium hydride. Finally, monosubstituted thiazolane-2,4-dione **8** was reacted *via* a Knoevenagel condensation with benzoic acid **7**.[28] *Z*-isomer **2** precipitated during reaction and washing the precipitate with ethanol resulted in homogeneous product (For ^{1}H NMR and HPLC spectra see Supporting Figure S3). The synthetic route toward **2** appeared to be applicable for the fast parallel synthesis and purification of many analogs without the need for chromatography.

3.4 Systematic optimization

Inhibitor **2** contains two side chains attached to the thiazolidine-2,4-dione core, a benzyl and a benzylidene moiety (Scheme 2). To explore structure-activity relationships (SAR), we first generated a small library before embarking on a bigger effort. This resulted in the molecules listed in Table 1. LPA was used as a control that it inhibits the ATX-mediated hydrolysis of bis-pNPP by ATX (IC_{50} = 0.4 µM).[15]

The best series of inhibitors are the benzoic acids (**2** and **9**-**11**), where the fluorinated compound **2** has the highest activity (IC_{50} = 56 nM) in the bis-pNPP assay (Table 1). Replacement of the 4-fluorine atom (**2**) for hydrogen (**9**), nitro- (**10**) or a *tert*-butyl group (**11**) reduced the potency of the inhibitor with increasing size of the functional group. With the replacement of the carboxylic acid in molecules **2** and **9**-**11** by a methyl ester (**12**-**15**), potency

Table 1. Structure-activity data for molecules of the systematic optimization. IC$_{50}$ values and residual ATX activity (RA) of the synthesized thiazolidine-2,4-dione derivatives using the artificial ATX substrate bis-pNPP (na: not active at 5 µM).

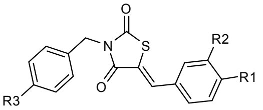

R1	R2	R3	Entry	IC$_{50}$ (µM)	RA (%)
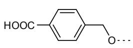	OMe	H	**9**	0.248	9
	OMe	F	**2**	0.056	10
	OMe	NO_2	**10**	0.442	33
	OMe	$C(CH_3)_3$	**11**	18.2	33
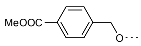	OMe	H	**12**	2.69	24
	OMe	F	**13**	>100	-
	OMe	NO_2	**14**	60.9	31
	OMe	$C(CH_3)_3$	**15**	>100	-
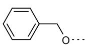	OMe	H	**16**	>100	-
	OMe	F	**17**	5.87	12
	OMe	NO_2	**18**	>100	-
	OMe	$C(CH_3)_3$	**19**	na	-
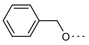	H	H	**20**	2.69	32
	H	F	**21**	0.700	37
	H	NO_2	**22**	>100	-
	H	$C(CH_3)_3$	**23**	>100	-
H	H	H	**24**	>100	-
	H	F	**25**	>100	-
	H	NO_2	**26**	na	-
	H	$C(CH_3)_3$	**27**	na	-
-	-	-	LPA	0.442	39

is largely lost. Omitting the carboxylic acid (**16**-**19**) has the same effect. With removal of the methoxy group (R2) in molecules **16**-**19**, activity is regained (compare **16-19** with **20-23**). SAR analysis showed that the optimal combination of groups would be R1 = -OCH$_2$-Ph-COOH, R2 = H and R3 = F.

Encouraged by the SAR results suggesting that the methoxy and carboxylic acid groups are important moieties, molecules **28**-**30** were synthesized (Figure 3A). Molecules **2**, **9**-**11** and **28**-**30** were validated in the physiologically more relevant LPC hydrolysis (choline release) assay.[17] The ATX-mediated release of choline from LPC is detected by a two-step enzymatic colorimetric reaction (Figure 1C). In the first step choline is oxidized by choline oxidase into betaine (trimethylglycine) and hydrogen peroxide. Horseradish peroxidase (HRP) then consumes hydrogenperoxide to oxidize 2,2'-azino-bis(3-ethylbenzothiazoline-6-sulfonic acid) (ABTS) to a radical cation species which absorbs at 405 nm.

The data obtained from the choline release assay are summarized in Figure 3A. The IC$_{50}$ values obtained were some 10-fold higher than observed in with bis-pNPP as a substrate. It is noteworthy that compound **10** is incapable of fully inhibiting ATX at high concentrations (Figure 3B). This residual ATX activity for **10** is about 60%. However, **10** shows inhibition at a lower concentration than **11** which was also observed in the bis-pNPP assay. LPA did not inhibit ATX in the choline release assay as observed by Ferry *et al.*[19]

The established SAR was confirmed by the more active molecule **28** (IC$_{50}$ = 1.63 µM) in which the methoxy group in **2** (IC$_{50}$ = 2.50 µM) is omitted. Changing the carboxylic acid of **2** from *para* to the *meta* position results in the more potent inhibitor **29** (IC$_{50}$ = 2.05 µM) but less potent than **28**. Changing the carboxylic acid in **28** from *para* to *meta* (**30** (HA51), IC$_{50}$ = 1.07 µM) results in the most active molecule in this systematic optimization with a 2.5-fold reduction in IC$_{50}$ value compared to **2** and also to a further reduction in residual ATX activity (from 35 to 7%) in the choline release assay.

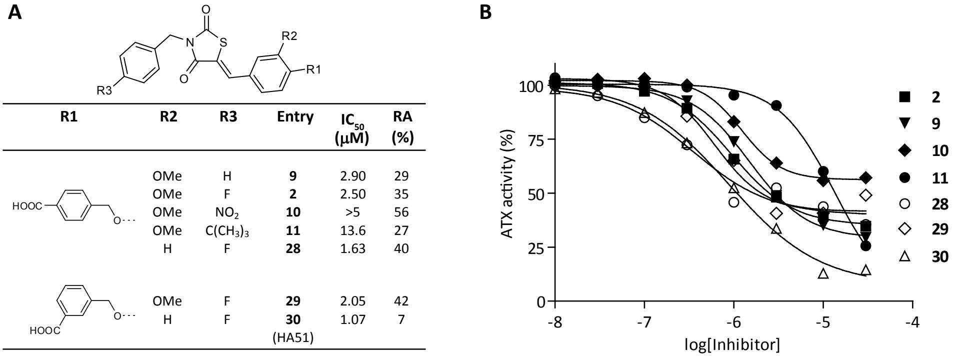

R1	R2	R3	Entry	IC_{50} (μM)	RA (%)
	OMe	H	**9**	2.90	29
	OMe	F	**2**	2.50	35
	OMe	NO_2	**10**	>5	56
	OMe	$C(CH_3)_3$	**11**	13.6	27
	H	F	**28**	1.63	40
	OMe	F	**29**	2.05	42
	H	F	**30** (HA51)	1.07	7

Figure 3. Validation of screening hit **2** and the benzoic acids of the systematic optimization in the choline release assay. (A) Structure-activity data of the systematic optimization. Residual ATX activity is abbreviated by RA (%). (B) Dose-response curves for the benzoic acids.

3.5 Variation in the benzyl moiety

Since our initial systematic optimization of **2** provided good structure-activity correlations we varied either the benzyl or the benzylidene moiety (Scheme 2). In this approach, either the benzyl or the benzylidene moiety corresponds to the screening hit **2** while the other part is alternated. First, the effect of changes in the benzyl part of the molecule was investigated by introducing halogens. The percentage inhibition (PI) values at 5 μM of compounds **31**-**40**, as measured by the choline release assay, are listed in Table 2. The most potent inhibitor was bromo compound **39** (PI = 73%). However, its IC_{50} (2.80 μM) is similar to that of screening hit **2** (IC_{50} = 2.50 μM). Other substituents (**41**-**71**) that were explored did not result in significant improvements.

3.6 Variation in the benzylidene moiety.

Next, variations were incorporated into the benzylidene moiety, resulting in molecules shown in Supporting Table S1. In contrast to the variation in the benzyl moiety, few molecules were active; only 30% of the compounds tested showed inhibition (PI_{max} = 12%). This indicates that variations in the benzylidene moiety of screening hit **2** are not well tolerated.

3.7 Boronic acid introduction and optimization

Because the benzyl and benzylidene moiety variations did not improve inhibition, we modified inhibitor **30** that resulted from the systematic optimization. Replacing the carboxylic acid in molecule **30** by a boronic acid resulted in molecule **72** (HA130, Table 3). We recently characterized **72** as a potent ATX inhibitor both *in vitro* and *in vivo*.[24] We reasoned that the carboxylic acid moiety in molecule **30** could act as a phosphate mimic that binds near or at the active site threonine (T210). Replacing the carboxylic acid in molecule **30** by a boronic

Table 2. Derivatives of screening hit **2** with a structural variation in the benzyl moiety (R). Percentage inhibition (PI, %) has been determined in the choline release assay at 5 µM. Molecules that show more than 50% inhibition are in bold (**compound** / PI).

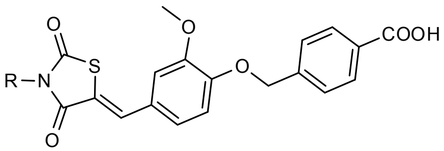

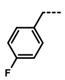 **2** / 55%	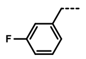 **31** / 64%	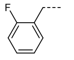 **32** / 41%	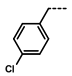 **33** / 57%	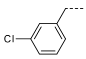 **34** / 29%	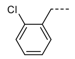 **35** / 57%
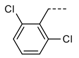 **36** / 38%	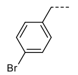 **37** / 23%	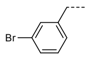 **38** / 26%	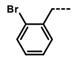 **39** / 72%	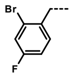 **40** / 51%	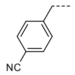 **41** / 21%
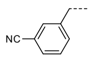 **42** / 44%	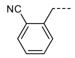 **43** / 17%	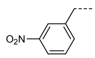 **44** / 48%	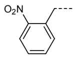 **45** / 38%	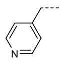 **46** / 13%	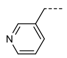 **47** / 17%
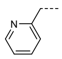 **48** / 10%	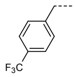 **49** / 32%	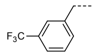 **50** / 46%	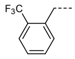 **51** / 28%	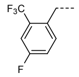 **52** / 13%	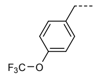 **53** / 12%
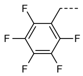 **54** / 10%	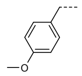 **55** / 11%	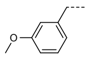 **56** / 20%	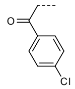 **57** / 35%	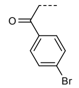 **58** / 23%	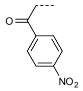 **59** / 17%
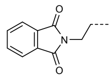 **60** / 0%	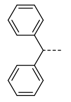 **61** / 4%	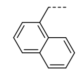 **62** / 13%	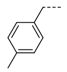 **63** / 11%	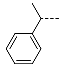 **64** / 5%	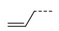 **65** / 19%
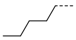 **66** / 15%	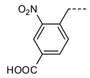 **67** / 31%	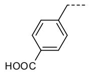 **68** / 49%	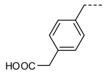 **69** / 42%	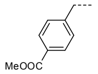 **70** / 31%	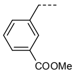 **71** / 30%

acid could well be a good ATX targeting strategy. This strategy was inspired by the proteasome inhibitor bortezomib, which targets the N-terminal threonine oxygen nucleophile in the proteasome through a boronic acid.[29] Furthermore, boronic acids have been reported to inhibit β-lactamases through targeting of the active site serine residue.[30]

The boronic acid modification resulted in a 100-fold more potent inhibitor (IC_{50} = 28 nM) compared to screening hit **2** (IC_{50} = 2.50 µM). When the position of the boronic acid was changed from *meta* (**72**) to the *para* (**73**) position, potency increased by another 5-fold (IC_{50} = 5.7 nM), while the potency of the *ortho* boronic acid **74** dropped (IC_{50} > 5.00 µM). Next, the

Table 3. Potent ATX inhibitors of the boronic acid optimization. For the boronic acids percentage inhibition (PI, %) at 5 µM and IC_{50} values have been determined in the choline release assay (PI / IC_{50}).

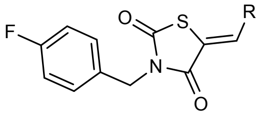

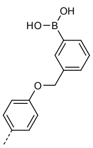	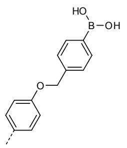	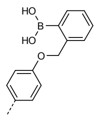	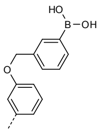	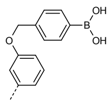	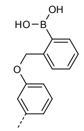
72 (HA130)	**73** (HA155)	**74**	**75**	**76**	**77**
99% / 28.3 nM	99% / 5.67 nM	36% / >5.00 µM	100% / 11.9 nM	100% / 29.6 nM	11% / >5.00 µM

3-benzyloxy boronic acids analogs **75**-**77** were synthesized. The *meta* boronic acid (**75**) proved to be more potent than the *para* (**76**) and the *ortho* boronic acid (**77**) has a low potency.

3.8 Effect inhibitors on readout choline release assay

An inherent danger of the choline release assay is that small molecules can interfere with the readout by inhibiting the enzymes (horseradish peroxidase or choline oxidase) used in the coloring reaction, resulting in false positives. Another way to interfere with the choline release assay is that compounds can react with the ABTS or hydrogen peroxide generated during the coloring reaction. The latter could be an issue for the boronic acids reported here because aliphatic and aryl boronic acids have the ability to react with hydrogen peroxide.[31-33] We investigated the effect of the inhibitors **72**, **73**, **75** and **76** on the coloring reaction, and no effect was observed (Supporting Figure S4). Therefore, the choline release assay is a valid way to test the synthesized compounds here on ATX inhibition.

3.9 Mode of inhibition

For inhibitors **2**, **30**, **72** and **73**, the mode of inhibition was determined from a Lineweaver-Burk plot (Supporting Figure S5). Inhibitors **2** and **30** inhibit in a competitive manner using LPC as substrate. Kinetic analysis for boronic acids **72** and **73** revealed a mixed type inhibition.

Because these inhibitors contain a Michael acceptor, it could be that these inhibitors react irreversibly with ATX (or other enzymes), which is undesirable. When ATX is incubated with 5 µM inhibitor **2**, **30**, **72** or **73** for 20 min at 310 K and these solutions are then washed with ethyl acetate, ATX activity is restored up to 97% of its original activity in the choline release assay (Supporting Figure S6). This indicates that these inhibitors reversible bind to ATX.

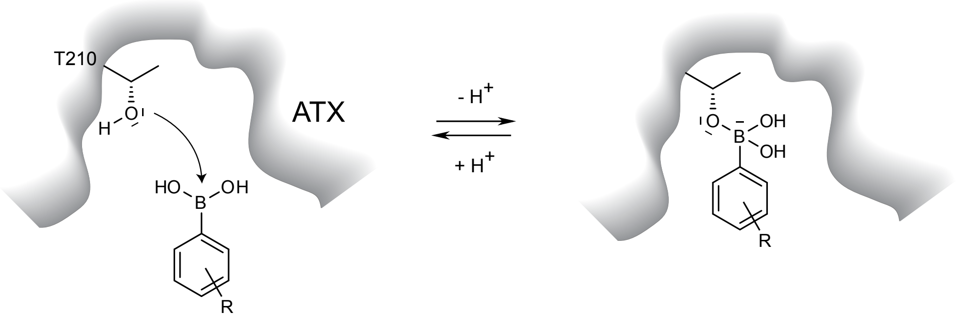

Figure 4. Our hypothesis on the binding of boronic acid-based ATX inhibitors with the T210 oxygen nucleophile in the ATX active site.

3.10 Discussion and conclusions

This study shows that ATX can be targeted efficiently by boronic acid inhibitors. We discovered thiazolidine-2,4-diones as potent non-lipid ATX inhibitors. Replacing the carboxylic acid by a boronic acid in thiazolidine-2,4-dione screening hit **2** resulted in a 440-fold more active inhibitor (IC_{50} = 2.50 µM → 6 nM).

We handed three different approaches for optimization of screening hit **2**. The first is the systematic optimization of **2**, which led to a 2.5-fold increase in potency in the choline release assay. The second is a randomized approach, changing separately the benzyl and the benzylidene parts of the molecule. This did not result in significantly more potent molecules. Finally, we replaced the carboxylic acid in screening hit **2** by a boronic acid. Our rationale was that the carboxylic acid could function as a phosphate mimic and thereby bind near or at the T210 oxygen nucleophile. In that case, the T210 oxygen nucleophile in ATX can be targeted *via* a boronic acid. A similar strategy has proven successful for the proteasome inhibitor bortezomib which binds to threonine oxygen nucleophile in the proteasome active site through the boronic acid moiety.[29] Replacing the carboxylic acid moiety in screening hit **2** (IC_{50} = 2.50 µM) by a boronic acid resulted in molecule **73** (IC_{50} = 6 nM), which is over 400-fold more potent than inhibitor **2**. These results demonstrate that ATX activity can be targeted by boronic acids. Next, to their increased affinity for ATX, the boronic acids are also expected to improve selectivity over hydrolytic enzymes that depend on a sulfur (cysteine) nucleophile, as is commonly found in phosphate ester hydrolyzing enzymes.

Kinetic analysis showed that inhibitors **2** and **30** inhibit in a competitive manner indicating that they bind at the active site of ATX. The acid moiety of these inhibitors likely mimics the phosphate group, facilitating inhibition. Boronic acids **72** and **73** show a mixed-type inhibition. It is expected that the boronic acids have the same binding site as their carboxylic acid equivalents **2** and **30** based on their structural similarity. Binding of the boronic acid to the T210 oxygen nucleophile likely results in the Lineweaver-Burk plot observed. The washout experiment reveals that inhibitors **2**, **30**, **72** and **73** all bind to ATX in a reversible manner. Figure 4 shows how the boronic acid inhibitors may bind to the T210 oxygen nucleophile of ATX.

In summary, we have identified thiazolidine-2,4-diones as ATX inhibitors and have found that targeting ATX with a boronic acid moiety resulted in a >400-fold increase in potency. This strategy to target ATX with a boronic acid should assist the development of future ATX inhibitors.

3.11 Experimental section

Chemicals and enzymes. Small molecule libraries were obtained from the National Cancer Institute (NCI) and purchased from SPECS, Delft, the Netherlands. NCI compounds NSC101794, NSC148368 and NSC48300 are abbreviated in the text of the Supporting information by **I**, **II** and **III** respectively. SPECS compounds AN-989/40746701, AN-988/40680277, AJ-292/40674401, AN-989/41697652, AN-989/41697944 and AQ-088/4201464 are abbreviated in the text by **1**, **2**, **3**, **4**, **5** and **6** respectively. 1-Oleoyl-2-Hydroxy-*sn*-Glycero-3-Phosphocholine (LPC, 18:1) was purchased from Avanti Polar Lipids. Oleoyl-L-α-lysophosphatidic acid sodium salt (LPA, 18:1), horseradish peroxidase (HRP), choline oxidase, and all other chemicals were obtained from Sigma-Aldrich and used as received.

Recombinant ATX. See Experimental section Chapter 2.

Bis-pNPP assay.[15] ATX activity toward bis-pNPP was determined as follows. In an opaque flat-bottom 384-well plate an amount of 2 μL DMSO containing inhibitor was added to 24 μL recombinant ATX (~20 nM) in Tris-buffered saline (140 mM NaCl, 5 mM KCl, 1 mM $CaCl_2$, 1 mM $MgCl_2$ and 50 mM Tris-HCl, pH 7.8) which contained albumin from bovine serum fatty acid free (BSA-FAF) (0.2 mg ml^{-1}). Finally, 24 μL of bis-pNPP (2 mM) was added to each well and the plate was incubated for 3 h at room temperature. This mixture with DMSO alone was used as a control. For each inhibitor ten concentrations were measured covering a range of 0.025 to 100 μM to determine IC_{50} values. Percentage inhibition was determined for a final concentration of 5 μM of inhibitor. Absorbance was measured in a Perkin-Elmer Envision plate reader (λ = 405 nm). The absorbance at 0 h was used to correct for molecules that absorb at 405 nm. Data were analyzed using Graphpad Prism software. IC_{50} values and percentage inhibition were determined in three independent experiments for each inhibitor. Percentage of residual activity (RA) is given as bottom value for curve fit.

CPF4 assay.[15] This assay was carried out in the same manner as the bis-pNPP assay using a substrate concentration of 2 μM. Fluorescence was monitored in a BMG Fluorstar 96-well plate reader (λ_{ex} = 355 nm, λ_{em} = 460 and 520 nm).

Choline release assay.[17] Measuring ATX activity using LPC (18:1) as substrate was determined as follows. In an opaque flat-bottom 96-wells plate (Greiner) 1 μL of DMSO containing inhibitor was added to 49 μL of recombinant ATX (~20 nM) in Tris-HCl buffer (0.01% Triton X-100 and 50 mM Tris-HCl, pH 7.4). Finally, 50 μL of 80 μM LPC (18:1) in Tris-HCl buffer (10 mM $MgCl_2$, 10 mM $CaCl_2$, 0.01% Triton X-100 and 50 mM Tris-HCl, pH 7.4) was added to each well and the plate was incubated at 310 K. The above-described mixture with DMSO alone was used as a control. LPC without ATX was taken as control for autohydrolysis of LPC. For each inhibitor ten concentrations were measured covering a range of 0.01 to 30 μM to determine IC_{50} values. Percentage inhibition (PI) was determined for a final concentration of 5 μM of inhibitor. After 3 h of incubation, 50 μL of ABTS (2 mM) and horseradish peroxidase (5 U mL^{-1}) was added to 50 μL of the reaction mixture and absorbance was measured and used to correct for absorbance of the molecules. Finally, 50 μl choline oxidase (5 U mL^{-1}) in Tris-HCl (0.01% Triton X-100 and 50 mM Tris-HCl, pH 7.4) was added for colorimetric reaction. Absorbance was measured in a Perkin-Elmer Envision plate reader (λ = 405 nm). Data were analyzed using Graphpad Prism software.

In addition, the effect of the inhibitors on the enzymatic coloring reaction was investigated using 40 μM choline at 30 μM inhibitor using the above-described coloring reagents. No inhibition of the enzymatic reaction by inhibitors was observed.

Washout of inhibitors. ATX (~20 nM) in the same buffer used for the choline release assay was incubated with (5 μM) and without inhibitors at 310 K. After 20 min the incubation mixtures were washed out with ethyl acetate with 9 times the volume of the ATX solution. The ATX activity of these solutions was determined using the choline release assay.

Chemistry. All chemicals were obtained from Sigma-Aldrich and used without further purification. Dry *N,N*-dimethylformamide (DMF) from Biosolve was obtained by treatment with molecular molsieves (4 Å). Analytical thin layer chromatography was performed on aluminum sheets precoated with silica gel 60 F_{254}. Column chromatography was carried out on silica gel (0.035-0.070, 90 Å, Acros).

For isolation by centrifugation a Heraeus Multifuge 3 $_{S-R}$ centrifuge was used. Products were spun at 4400*g* at 277 K for 5 min. Nuclear magnetic resonance spectra (^{1}H NMR and COSY) were determined in deuterated dimethyl sulfoxide (d_6-DMSO) using a Bruker ARX 400 Spectrometer (^{1}H: 400 MHz) at 298 K, unless indicated otherwise. Peak shapes in the NMR spectra are indicated with the symbols 'd' (doublet), 'dd' (double doublet), 's' (singlet), 'bs' (broad singlet) and 'm' (multiplet). Chemical shifts (δ) are given in ppm and coupling constants *J* in Hz. DMSO (δ = 2.50 ppm) was used as internal reference.

HPLC-MS measurements were performed on a system equipped with a Waters 2795 Seperation Module (Alliance HT), Waters 2996 Photodiode Array Detector (190-750 nm), Waters Alltima C18 Column (2.1 mm x 100 mm) and an LCT™ Orthogonal Acceleration Time of Flight Mass Spectrometer. Samples were run at a flowrate of 0.40 mL min^{-1} using gradient elution (water/acetonitrile/formic acid) from 950/50/10 (*v/v/v*) to 50/950/10 (*v/v/v*). Purity of all compounds was verified by HPLC-MS. The purity of all tested compounds was determined by HPLC-MS analyses and was greater than 95%.

4-[(4-formyl-2-methoxyphenoxy)methyl]benzoic acid (7).

To a solution of vanillin (1.41 g, 9.24 mmol) and KOH (0.640 g, 11.4 mmol) in DMSO (10 mL), methyl-4-(bromomethyl)benzoate (2.00 g, 8.73 mmol) was added. The reaction mixture was stirred at room temperature and after 30 min, water (50 mL) was added and the solution was heated at 393 K for 2 h. Subsequently, 1M NaOH (aq) (10 mL) was added under relfux till solution becomes clear. Finally, the reaction mixture was poured into water and was acidified with 1 M HCl to pH 2. The precipitate was isolated by centrifugation, washed with water, and lyophilized resulting in the title compound. **Yield:** 91%. **^{1}H NMR**: δ = 12.99 (bs, 1H, OH), 9.85 (s, 1H), 7.98 (d, *J* 8.3, 2H), 7.58 (d, *J* 8.3, 2H), 7.55 (dd, *J* 1.9 and 8.3, 1H), 7.44 (d, *J* 1.8, 1H), 7.26 (d, *J* 8.3, 1H), 5.32 (s, 2H), 3.86 (s, 3H). **MS**: m/z $[M+H]^+$ calc. 287.09, obs. 287.11.

Synthesis of 3-(4-fluorobenzyl)-1,3-thiazolane-2,4-dione (8).

To a cooled solution (273 K) of thiazolidine-2,4-dione (5.87 g, 50 mmol) in DMF (100 ml) sodium hydride (60% in oil, 1.8 g, 45 mmol) was added. A solution of 1-(chloromethyl)-4-fluorobenzene (4.3

ml, 36.8 mmol) in DMF (25 ml) was added to the reaction mixture. The mixture was allowed to warm up to room temperature and was stirred for 4 h. Then the mixture was poured in ice water (250 ml) and hexane (100 ml) was added. After a night at 277 K the precipitated crystals were filtrated and dried to give a white solid. **Yield:** 74%. **^{1}H NMR**: δ = 7.34-7.14 (m, 4H), 4.65 (s, 2H), 4.26 (s, 2H). **MS**: m/z $[M+H]^+$ calc. 226.03, obs. 226.04.

Experimental details on compounds 9-30. This data is available free of charge *via* the Internet at http://pubs.acs.org.

General method for the synthesis of (2,4-dioxo-1,3-thiazolan-5-yliden) benzoic acids and benzene boronic acids.
To a solution of 1,3-thiazolane-2,4-dione **8** (0.293 mmol) in ethanol (2.5 mL), piperidine (12 μL, 0.207 mmol) and the appropriate aldehyde (0.352 mmol) were added and the solution was refluxed for 22 h. Upon cooling to room temperature the product precipitated out of solution. Centrifugation and washing with ethanol gave homogeneous compound.

4-[(4-{[3-(4-fluorobenzyl)-2,4-dioxo-1,3-thiazolan-5-yliden]methyl}-2-methoxy-phenoxy)-methyl]benzoic acid (2). Yield: 63%. COSY was used to assign chemical shifts. **^{1}H NMR**: δ = 12.99 (bs, 1H, OH), 7.97 (d, *J* 8.3, 2H), 7.92 (s, 1H), 7.56 (d, *J* 8.3, 2H), 7.38-7.16 (m, 7H), 5.27 (s, 2H), 4.82 (s, 2H), 3.84 (s, 3H). **MS**: m/z $[M-H]^-$ calc. 492.10, obs. 492.10.

3-[(4-{[3-(4-fluorobenzyl)-2,4-dioxo-1,3-thiazolan-5-yliden]methyl}phenoxy)methyl] benzene boronic acid (72). Yield: 64%. **^{1}H NMR**: δ = 8.08 (s, 2H, OH), 7.92 (s, 1H), 7.87 (s, 1H), 7.76 (d, *J* 7.4, 1H), 7.60 (d, *J* 7.1, 2H), 7.50-7.16 (m, 10H), 5.18 (s, 2H), 4.82 (s, 2H). **MS**: m/z $[M +H]^+$ calc. 464.11, obs. 464.25.

4-[(4-{[3-(4-fluorobenzyl)-2,4-dioxo-1,3-thiazolan-5-yliden]methyl}phenoxy)methyl] benzene boronic acid (73). Yield: 81%. **^{1}H NMR**: δ = 8.05 (s, 2H, OH), 7.93 (s, 1H), 7.81(d, *J* 8.0, 2H), 7.61 (d, *J* 8.9, 2H), 7.42 (d, *J* 8.3, 2H), 7.41-7.16 (m, 6H), 5.21 (s, 2H), 4.82 (s, 2H). **MS**: m/z $[M+H]^+$ calc. 464.11, obs. 464.21.

2-[(4-{[3-(4-fluorobenzyl)-2,4-dioxo-1,3-thiazolan-5-yliden]methyl}phenoxy)methyl] benzene boronic acid (74). Yield: 48%. **^{1}H NMR**: δ = 8.10 (s, 2H, OH), 7.93 (s, 1H), 7.62-7.13 (m, 12H), 5.32 (s, 2H), 4.82 (s, 2H). **MS**: m/z $[M+H]^+$ calc. 464.11, obs. 464.12.

3-[(3-{[3-(4-fluorobenzyl)-2,4-dioxo-1,3-thiazolan-5-yliden]methyl}phenoxy)methyl] benzene boronic acid (75). Yield: 40%. **^{1}H NMR**: δ = 8.10 (bs, 2H, OH), 7.94 (s, 1H), 7.87 (s, 1H), 7.76 (d, *J* 7.3, 1H), 7.51-7.16 (m, 10H), 5.16 (s, 2H), 4.82 (s, 2H). **MS**: m/z $[M +H]^+$ calc. 464.11, obs. 464.13.

4-[(3-{[3-(4-fluorobenzyl)-2,4-dioxo-1,3-thiazolan-5-yliden]methyl}phenoxy)methyl] benzene boronic acid (76). Yield: 26%. **^{1}H NMR**: δ = 8.07 (s, 2H, OH), 7.93 (s, 1H), 7.81(d, *J* 8.0, 2H), 7.49-7.16 (m, 10H), 5.19 (s, 2H), 4.82 (s, 2H). **MS**: m/z $[M+H]^+$ calc. 464.11, obs. 464.12

2-[(3-{[3-(4-fluorobenzyl)-2,4-dioxo-1,3-thiazolan-5-yliden]methyl}phenoxy)methyl] benzene boronic acid (77). Yield: 32%. **^{1}H NMR**: δ = 8.09 (s, 2H, OH), 7.94 (s, 1H), 7.57-7.12 (m, 12H), 5.29 (s, 2H), 4.83 (s, 2H). **MS**: m/z $[M+H]^+$ calc. 464.11, obs. 464.13.

3.12 References

1. Gijsbers, R. Aoki, J. Arai, H. & Bollen, M. The hydrolysis of lysophospholipids and nucleotides by autotaxin (NPP2) involves a single catalytic site. *FEBS Lett.* **538**, 60-64 (2003).
2. Clair, T. Lee, H. Y. Liotta, L. A. & Stracke, M. L. Autotaxin is an exoenzyme possessing 5'-nucleotide phosphodiesterase/ATP pyrophosphatase and ATPase activities. *J. Biol. Chem.* **272**, 996-1001 (1997).
3. Bollen, M. Gijsbers, R. Ceulemans, H. Stalmans, W. & Stefan, C. Nucleotide pyrophosphatases/phosphodiesterases on the move. *Crit. Rev. Biochem. Mol. Biol.* **35**, 393-432 (2000).
4. Tokumura, A. et al. Identification of human plasma lysophospholipase D, a lysophosphatidic acid-producing enzyme, as autotaxin, a multifunctional phosphodiesterase. *J. Biol. Chem.* **277**, 39436-39442 (2002).
5. Umezu-Goto, M. et al. Autotaxin has lysophospholipase D activity leading to tumor cell growth and motility by lysophosphatidic acid production. *J Cell Biol* **158**, 227-233 (2002).
6. Moolenaar, W. H. van Meeteren, L. A. & Giepmans, B. N. The ins and outs of lysophosphatidic acid signaling. *BioEssays* **26**, 870-881 (2004).
7. van Meeteren, L. A. et al. Autotaxin, a secreted lysophospholipase D, is essential for blood vessel formation during development. *Mol. Cell Biol.* **26**, 5015-5022 (2006).
8. Tanaka, M. et al. Autotaxin Stabilizes Blood Vessels and Is Required for Embryonic Vasculature by Producing Lysophosphatidic Acid. *J. Biol. Chem.* **281**, 25822-25830 (2006).
9. van Meeteren, L. & Moolenaar, W. Regulation and biological activities of the autotaxin-LPA axis. *Prog. Lipid Res.* **46**, 145-160 (2007).
10. David, M. et al. Cancer cell expression of autotaxin controls bone metastasis formation in mouse through lysophosphatidic acid-dependent activation of osteoclasts. *PLoS One* **5**, e9741 (2010).
11. Kanda, H. et al. Autotaxin, an ectoenzyme that produces lysophosphatidic acid, promotes the entry of lymphocytes into secondary lymphoid organs. *Nat. Immunol.* **9**, 415-423 (2008).
12. Tager, A. et al. The lysophosphatidic acid receptor LPA1 links pulmonary fibrosis to lung injury by mediating fibroblast recruitment and vascular leak. *Nat. Med.* **14**, 45-54 (2008).
13. Meyer zu Heringdorf, D. & Jakobs, K. H. Lysophospholipid receptors: signalling, pharmacology and regulation by lysophospholipid metabolism. *Biochim. Biophys. Acta* **1768**, 923-940 (2007).
14. Murakami, M. Shiraishi, A. Tabata, K. & Fujita, N. Identification of the orphan GPCR, P2Y10 receptor as the sphingosine-1-phosphate and lysophosphatidic acid receptor. *Biochem. Biophys. Res. Commun.* **371**, 707-712 (2008).
15. van Meeteren, L. A. et al. Inhibition of autotaxin by lysophosphatidic acid and sphingosine 1-phosphate. *J. Biol. Chem.* **280**, 21155-21161 (2005).
16. Gajewiak, J. Tsukahara, R. Fujiwara, Y. Tigyi, G. & Prestwich, G. D. Synthesis, Pharmacology, and Cell Biology of sn-2-Aminooxy Analogues of Lysophosphatidic Acid. *Org. Lett.* (2008).
17. Cui, P. et al. Synthesis and biological evaluation of phosphonate derivatives as autotaxin (ATX) inhibitors. *Bioorg. Med. Chem. Lett.* **17**, 1634-1640 (2007).
18. Jiang, G. et al. α-Substituted Phosphonate Analogues of Lysophosphatidic Acid (LPA) Selectively Inhibit Production and Action of LPA. *ChemMedChem* **2**, 679-690 (2007).
19. Ferry, G. et al. S32826, A Nanomolar Inhibitor of Autotaxin: Discovery, Synthesis and Applications as a Pharmacological Tool. *J. Pharmacol. Exp. Ther.* **327**, 809-819 (2008).
20. van Meeteren, L. Brinkmann, V. Saulnier-Blache, J. Lynch, K. & Moolenaar, W. Anticancer activity

of FTY720: Phosphorylated FTY720 inhibits autotaxin, a metastasis-enhancing and angiogenic lysophospholipase D. *Cancer Lett.* **266**, 203-208 (2008).

21. Moulharat, N. Fould, B. Giganti, A. Boutin, J. & Ferry, G. Molecular pharmacology of adipocyte-secreted autotaxin. *Chem.-Biol. Interact.* **172**, 115-124 (2008).
22. Parrill, A. et al. Virtual screening approaches for the identification of non-lipid autotaxin inhibitors. *Bioorg. Med. Chem.* **16**, 1784-1795 (2008).
23. Hoeglund, A. et al. Optimization of a Pipemidic Acid Autotaxin Inhibitor. *J. Med. Chem.* **53**, 1056-1066 (2009).
24. Albers, H. M. et al. Boronic acid-based inhibitor of autotaxin reveals rapid turnover of LPA in the circulation. *Proc. Natl. Acad. Sci. USA* **107**, 7257-7262 (2010).
25. Takakusa, H. et al. Design and Synthesis of an Enzyme-Cleavable Sensor Molecule for Phosphodiesterase Activity Based on Fluorescence Resonance Energy Transfer. *J. Am. Chem. Soc.* **124**, 1653-1657 (2002).
26. Saunders, L. P. et al. Identification of small-molecule inhibitors of autotaxin that inhibit melanoma cell migration and invasion. *Mol. Cancer Ther.* **7**, 3352-3362 (2008).
27. Johnstone, R. & Rose, M. A rapid, simple, and mild procedure for alkylation of phenols, alcohols, amides and acids. *Tetrahedron* **35**, 2169-2173 (1979).
28. Bruno, G. et al. Synthesis and aldose reductase inhibitory activity of 5-arylidene-2,4-thiazolidinediones. *Bioorg. Med. Chem.* **10**, 1077-1084 (2002).
29. Groll, M. Berkers, C. Ploegh, H. & Ovaa, H. Crystal Structure of the Boronic Acid-Based Proteasome Inhibitor Bortezomib in Complex with the Yeast 20S Proteasome. *Structure* **14**, 451-456 (2006).
30. Crompton, I. E. Cuthbert, B. K. Lowe, G. & Waley, S. G. β-lactamase inhibitors. The inhibition of serine β-lactamases by specific boronic acids. *Biochem. J.* **251**, 453-459 (1988).
31. Kuivila, H. & Armour, A. Electrophilic Displacement Reactions. IX. Effects of Substituents on Rates of Reactions between Hydrogen Peroxide and Benzeneboronic Acid1-3. *J. Am. Chem. Soc.* **79**, 5659-5662 (1957).
32. Kuivila, H. Electrophilic Displacement Reactions. VI. Catalysis by Strong Acids in the Reaction between Hydrogen Peroxide and Benzeneboronic Acid1,2. *J. Am. Chem. Soc.* **77**, 4014-4016 (1955).
33. Snyder, H. R. Kuck, J. A. & Johnson, J. Organoboron Compounds, and the Study of Reaction Mechanisms. Primary Aliphatic Boronic Acids1. *J. Am. Chem. Soc.* **60**, 105-111 (1938).

3.13 Supporting information

ATX inhibitor screen NCI library

Screening a small molecule library of the National Cancer Institute (NCI) we identified xanthine and arsonate derivatives as moderate ATX inhibitors as depicted in Figure S2 using the bis-pNPP assay. Interestingly, aryl xanthines are known as phosphodiesterase 5 inhibitors.[1] The structure of arsonate **II** is related to a phenyldiazenylphenyl ATX inhibitors reported by Parrill *et al*.[2] Arsonate **III**, also known as NSC48300, was recently reported as ATX inhibitor and we also found it as screening hit.[3] However, in our hands quality control of different independent batches of arsonate **III** by HPLC-MS revealed that it contains mainly impurities while the presence of arsonate **III** could not be confirmed.

Supporting references

1. Arnold, R. et al. 8-Aryl xanthines potent inhibitors of phosphodiesterase 5. *Bioorg. Med. Chem. Lett.* **12**, 2587-2590 (2002).
2. Parrill, A. et al. Virtual screening approaches for the identification of non-lipid autotaxin inhibitors. *Bioorg. Med. Chem.* **16**, 1784-1795 (2008).
3. Saunders, L. P. et al. Identification of small-molecule inhibitors of autotaxin that inhibit melanoma cell migration and invasion. *Mol. Cancer Ther.* **7**, 3352-3362 (2008).

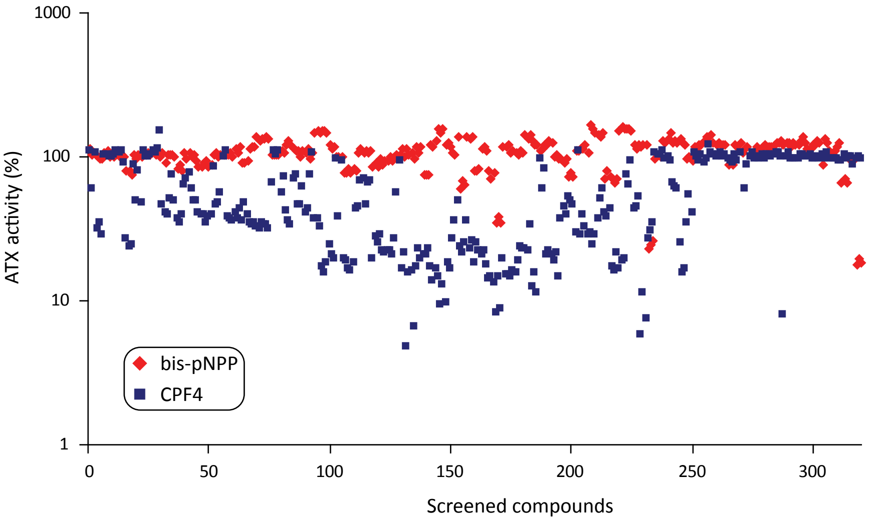

Supporting Figure S1. Primary hits obtained after screening 17,500 molecules from the NCI library using the ATX activity reporter CPF4. Bis-pNPP was used as a secondary assay to confirm the obtained hits from the initial screen. Significantly more inhibitors were identified with the CPF4 probe compared to the bis-pNPP assay. Interference with the CPF4 probe by small molecules likely leads to the many false positives observed. For this reason the bis-pNPP assay was used for further screening and the CPF4 assay for confirmation of screening hits.

Xanthine derivative

Arsonate derivatives

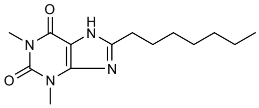

I (21%)

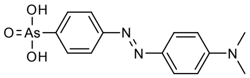

II (25%)

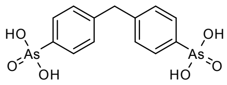

III (75%)

Supporting Figure S2. Structures of the identified inhibitor classes of the NCI library screen using the bis-pNPP assay. Xanthine and arsonate derivatives were identified as ATX inhibitors in the bis-pNPP assay. For each structure the percentage of ATX inhibition (PI, %) is given at an inhibitor concentration of 5 µM.

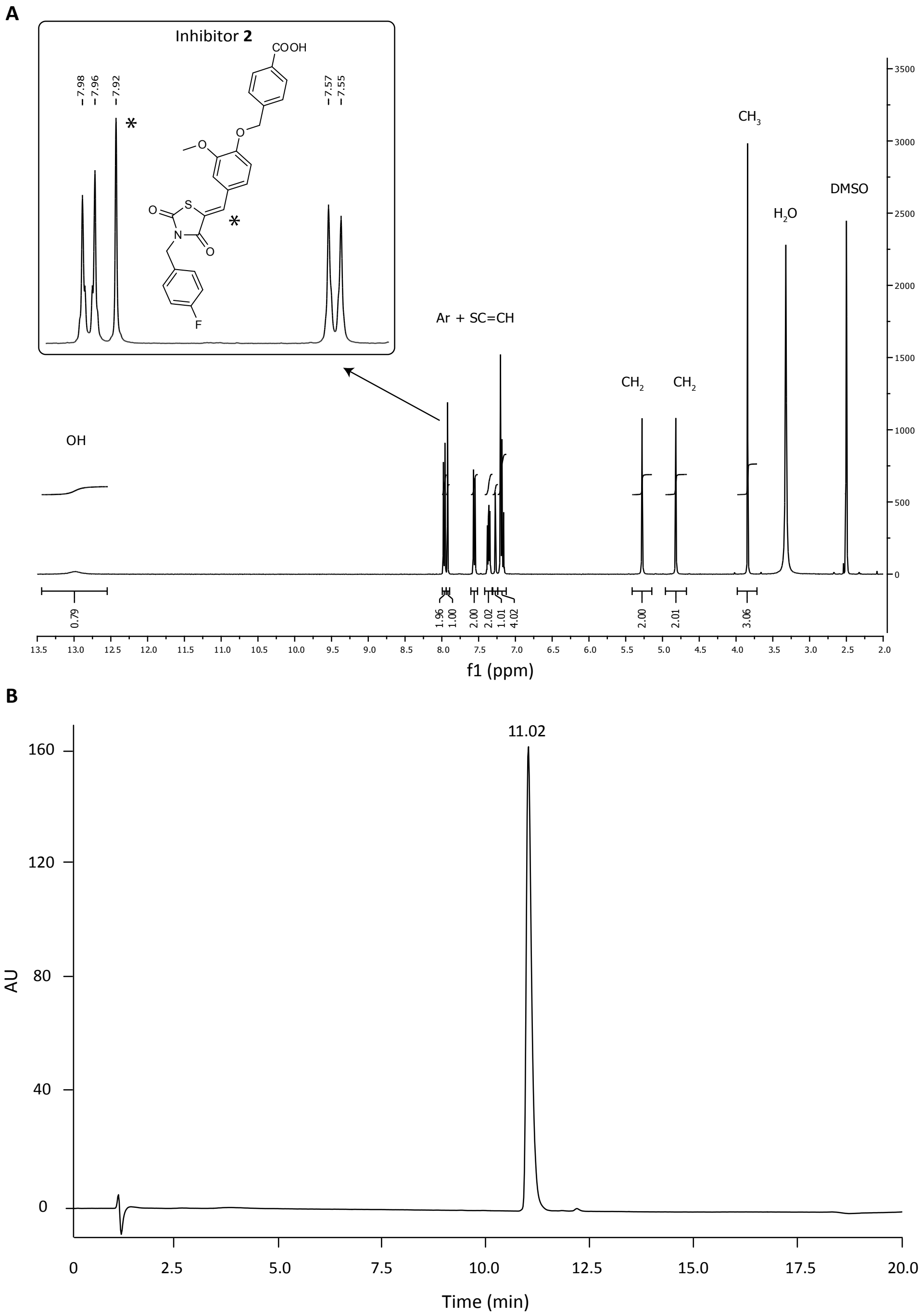

Supporting Figure S3. (A) ^{1}H NMR spectrum (d_6-DMSO) of inhibitor **2**. Inset shows the methylidene hydrogen (∗) at 7.92 ppm which is indicative for the *Z*-isomer.[28] (B) HPLC-chromatogram confirming the purity of inhibitor **2**.

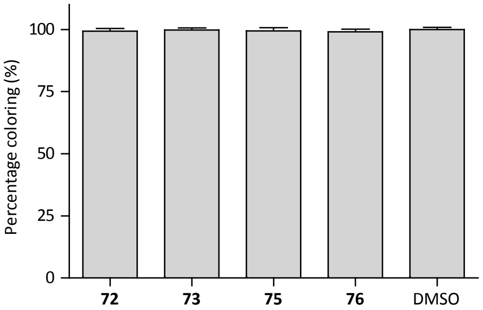

Supporting Figure S4. Effect of the active boronic acids on the readout of the choline release assay. No effect was observed on the readout using 40 µM choline at a concentration of 30 µM inhibitor.

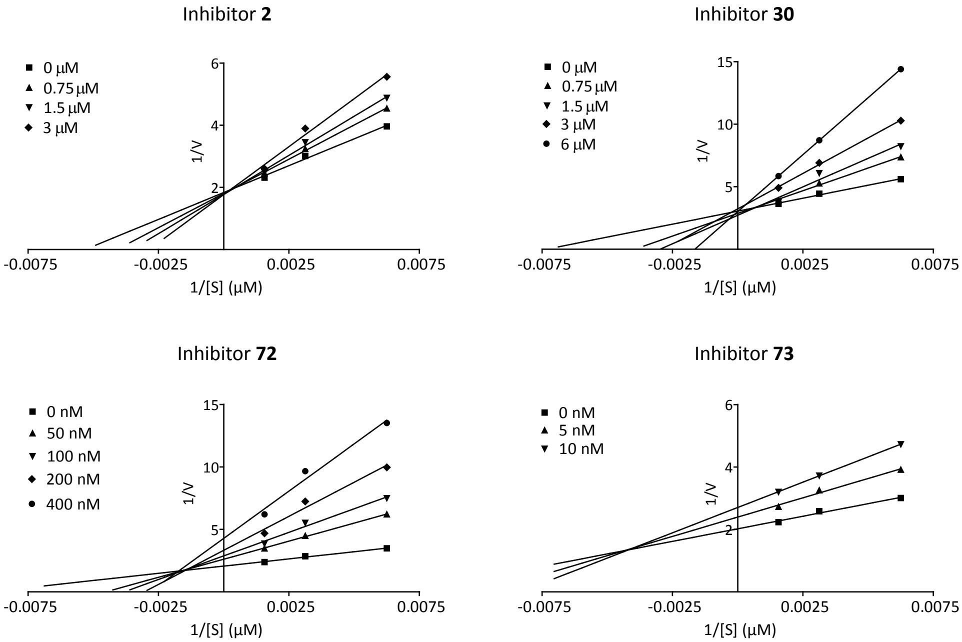

Supporting Figure S5. Lineweaver-Burk plots for the inhibitors of the optimization process. Kinetic analysis indicates competitive inhibition of ATX for **2** and **30**. Boronic acids **72** and **73** seem to inhibit in a mixed manner. Lineweaver-Burk plots were obtained from the choline release assay.

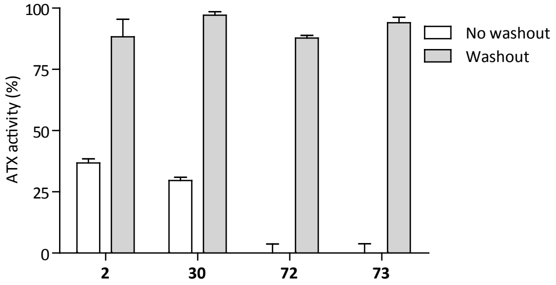

Supporting Figure S6. Washout experiment to study reversible binding the inhibitors with ATX. Incubating ATX with 5 µM of inhibitor **2**, **30**, **72** or **73** and washing out these solutions with ethyl acetate results in a recovery in ATX activity up to 97% in the choline release assay.

Supporting Table S1. Derivatives of screening hit **2** with a structural variation in the benzylidene moiety (R). Percentage inhibition (PI, %) at 5 µM has been determined in the choline release assay (**compound** / PI).

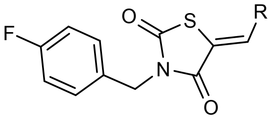

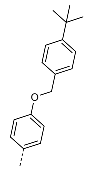 **78** / 5%	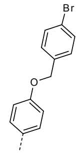 **79** / 3%	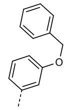 **80** / 0%	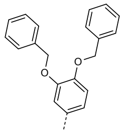 **81** / 0%	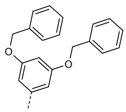 **82** / 0%	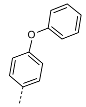 **83** / 0%
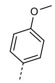 **84** / 0%	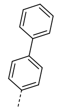 **85** / 0%	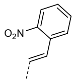 **86** / 4%	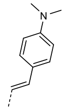 **87** / 0%	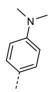 **88** / 0%	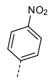 **89** / 0%
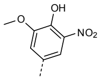 **90** / 0%	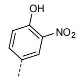 **91** / 0%	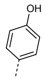 **92** / 0%	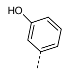 **93** / 0%	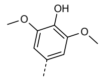 **94** / 12%	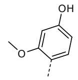 **95** / 3%
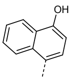 **96** / 4%	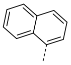 **97** / 2%	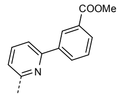 **98** / 0%	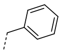 **99** / 0%	 **100** / 0%	

CHAPTER 4

Structure-based design of novel boronic acid-based inhibitors of autotaxin

Harald M.H.G. Albers, Loes J.D. Hendrickx, Rob J.P. van Tol, Jens Hausmann, Anastassis Perrakis and Huib Ovaa, *Journal of Medicinal Chemistry* **2011**, *54*, 4619-4626.

Abstract. Autotaxin (ATX) is a secreted phosphodiesterase that hydrolyzes the abundant phospholipid lysophosphatidylcholine (LPC) to produce lysophosphatidic acid (LPA). The ATX-LPA signaling axis has been implicated in inflammation, fibrosis and tumor progression, rendering ATX to an attractive drug target. Chapter 3 describes the development of a boronic acid-based inhibitor of ATX, named HA155 (**1**). This chapter reports the design of new inhibitors based on the crystal structure of ATX in complex with inhibitor **1**. Furthermore, the syntheses and activities of these new inhibitors are described and the potency of these inhibitors can be explained by structural data. To understand the difference in activity between two different isomers with nanomolar potencies, molecular docking experiments were performed using the crystal structure of ATX binding to inhibitor **1**. Intriguingly, molecular docking suggested a remarkable binding pose for one of the isomers, which differs from the original binding pose of inhibitor **1** for ATX, opening further options for inhibitor design.

4.1 Introduction

The secreted glycoprotein autotaxin (ATX) is a phosphodiesterase responsible for the hydrolysis of lysophosphatidylcholine (LPC) into lysophosphatidic acid (LPA) and choline, as depicted in Scheme 1.[1,2] The bioactive lipid LPA stimulates migration, proliferation and survival of cells by activating specific G protein-coupled receptors.[3] The ATX-LPA signaling axis is involved in cancer, inflammation and fibrotic disease.[4-6] Potent and selective ATX inhibitors are needed to elucidate the contribution of ATX action to signaling cascades that may result in disease in case of malfunction.

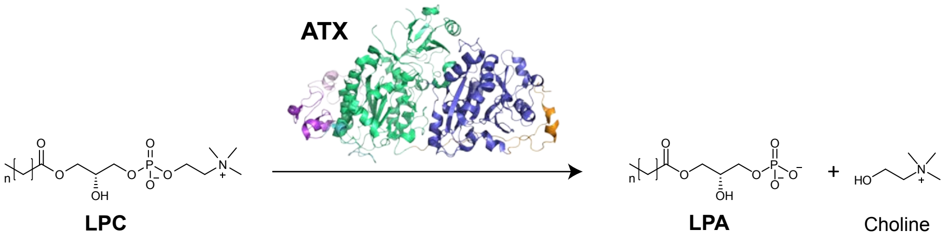

Scheme 1: Autotaxin (ATX) is responsible for hydrolyzing the lipid lysophosphatidylcholine (LPC) into lysophosphatidic acid (LPA) and choline.

ATX, also known as ENPP2, is a unique member of the ecto-nucleotide pyrophosphatase/ phosphodiesterase (ENPP) family of proteins. It is the only family member capable of producing LPA by hydrolysis of LPC.[7] Recently reported crystal structures of mouse[8] and rat[9] ATX confirmed that a threonine residue and two zinc ions are necessary for activity of ATX.[10] Furthermore, these structures showed that ATX specifically binds its lipid substrates in a hydrophobic pocket extending from the active site of ATX. This pocket accommodates the alkyl chain of the lipids in different poses as was also shown in various crystal structures.[8]

In Chapter 2 we described the discovery of a boronic acid-based ATX inhibitors that helped to reveal the short half life (~5 min) of LPA *in vivo*.[11,12] We introduced a boronic acid moiety in the inhibitor structure to rationally target the threonine oxygen nucleophile of ATX with a hard matching Lewis acid. The crystal structure of ATX in complex with HA155 (**1**),[9] confirmed our hypothesis described in Chapter 3 that this inhibitor targets the threonine oxygen nucleophile in the ATX active site *via* the boronic acid moiety, while the hydrophobic 4-fluorobenzyl moiety of inhibitor **1** targets the hydrophobic pocket responsible for lipid binding (Figure 1).

Here, we report a number of synthetic routes, systematically substituting the ether linker and the thiazolidine-2,4-dione core in **1**, while keeping the boronic acid moiety untouched. The observed structure-activity relations could well be explained from the ATX structure in complex with inhibitor **1**. A remarkable binding pose of a novel inhibitor, as predicted from molecular docking experiments, suggests additional avenues for further inhibitor design.

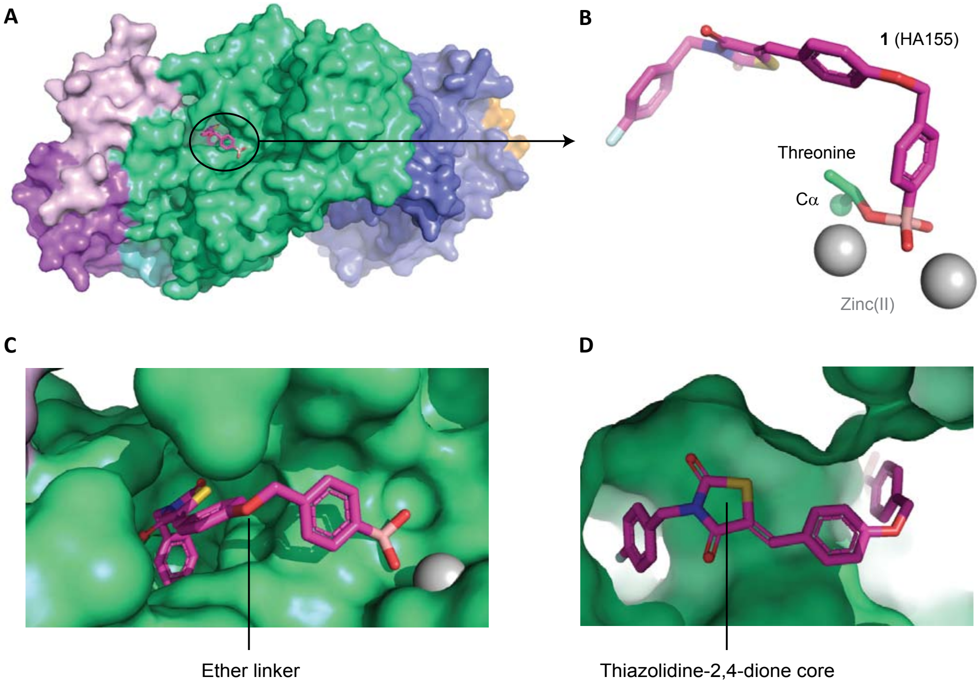

Figure 1: ATX crystal structure liganded with inhibitor **1** (PDB ID: 2XRG). (A) Surface representation of ATX with inhibitor **1** (magenta). (B) Binding of inhibitor **1** to the threonine oxygen nucleophile and two zinc ions. (C) Visualizing the ether linker of inhibitor **1** bound to ATX. (D) Visualizing the degree of freedom for the thiazolidine-2,4-dione core of inhibitor **1** in the ATX binding site. Images were made using the program PyMol.

4.2 Results and discussion

4.2.1 Design of inhibitors

The crystal structure of inhibitor **1** bound to the ATX active site (Figure 1) showed that its 4-fluorobenzyl moiety binds into the hydrophobic lipid binding pocket of ATX (Figure 1C, 1D).[9] This pocket also accommodates the lipid tail of LPA, the hydrolysis product of LPC.[8] The thiazolidine-2,4-dione core of **1** and the conjugated aromatic ring are located between the hydrophobic pocket and the catalytic site (Figure 1D). The ether linker, bridging the two aromatic rings in **1**, and especially a methylene and arylboronic acid moiety are well accessible to solvent (Figure 1C). Binding of inhibitor **1** to the ATX active site is predominately driven by hydrophobic interactions (the interaction interface is approximately 500 Å^2) and by the boronic acid binding to the threonine oxygen nucleophile of ATX.[9] The boron-oxygen distance observed is ~1.6 Å, which is consistent with a covalent bond. As expected, this binding is reversible evidenced by the fact that ATX activity can be fully restored upon washing out the inhibitor (see Chapter 3).[13] In addition, one of the boronic acid hydroxyl moieties is tethered by the two zinc ions in the ATX active site. Thus, the boronic acid moiety targets not only the threonine oxygen nucleophile, but also the two zinc ions that are essential for catalytic activity of ATX (Figure 1B). Remarkably, there are no hydrogen bonds or salt bridges that participate in binding of inhibitor **1** to ATX. Inhibitor **1** is locked in a pose with reduced molecular flexibility, forming an ideal starting point for a structure based approach to further modifications.

Previously, we determined that the 4-fluorobenzyl moiety is preferred from over 40 benzylic substituents tested (Chapter 3).[13] For this reason, we left the 4-fluorobenzyl moiety untouched in this study. We investigated new design options, starting by modifying the ether linker in inhibitor **1**. We decided to replace the ether linkage (OCH_2) with various amides, an amine and an *E*-configured double bond (CONH (**17**), $CONCH_2$ (**18**), NHCO (**19**), $NHCH_2$ (**36**) and (*E*)-CH=CH (**20**); see Table 1). The thiazolidine-2,4-dione core was investigated also. The sulfur atom in this core was replaced with (substituted) amino and methylene moieties (NH (**26**), NCH_3 (**28**), or CH_2 (**32**); see Table 2). The carbon double bond conjugated to the thiazolidine-2,4-dione carbonyl moiety forms a possible Michael acceptor. Although this Michael acceptor is resistant to nucleophilic additions *in vitro* (Supporting Figure S1) it may be a biologically active Michael acceptor *in vivo* and therefore, we investigated its removal.

4.2.2 Chemical synthesis of modified inhibitors

We first explored synthetic routes to replace the ether linkage in **1**. The synthesis of target molecules **17**-**20** (Scheme 2) starts with palladium catalyzed borylation of appropriate aldehydes *via* a Suzuki-Miyaura reaction[13] as depicted in Scheme 2 (for syntheses of aldehydes **2**-**6** see Supporting Information). This reaction provided intermediates **7**-**11**. Next, the pinacol protecting group was hydrolyzed under acidic conditions and oxidatively destroyed by $NaIO_4$ giving boronic acid aldehydes **12**-**16**. In the final step, 3-(4-fluorobenzyl)thiazolidine-2,4-dione is reacted with the boronic acid aldehyde by Knoevenagel condensation to selectively give the *Z*-isomer of the final products (**1** and **17**-**20**).

In order to remove the potential Michael acceptor present, we reduced the double bond in inhibitor **1** using hydrogen and palladium on carbon (Scheme 3A), to give compound **21**. To reduce the carbonyl moiety also in the thiazolidine-2,4-dione core of **1**, we used $NaBH_4$ resulting in hemiaminal **22**. After addition of sulfuric acid to the reaction mixture to eliminate the hydroxyl moiety in **22**, unsaturated inhibitor **23** was obtained.

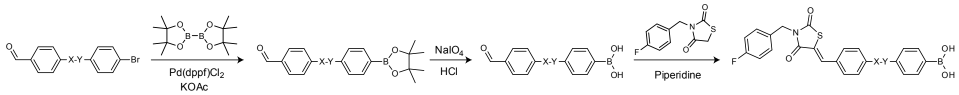

X	Y				
O	CH_2	**2**	**7**	**12**	**1** (HA155)
C=O	NH	**3**	**8**	**13**	**17**
C=O	$NHCH_2$	**4**	**9**	**14**	**18**
NH	C=O	**5**	**10**	**15**	**19**
(*E*)-HC=CH	-	**6**	**11**	**16**	**20**

Scheme 2: Synthetic route toward linker modified inhibitors.

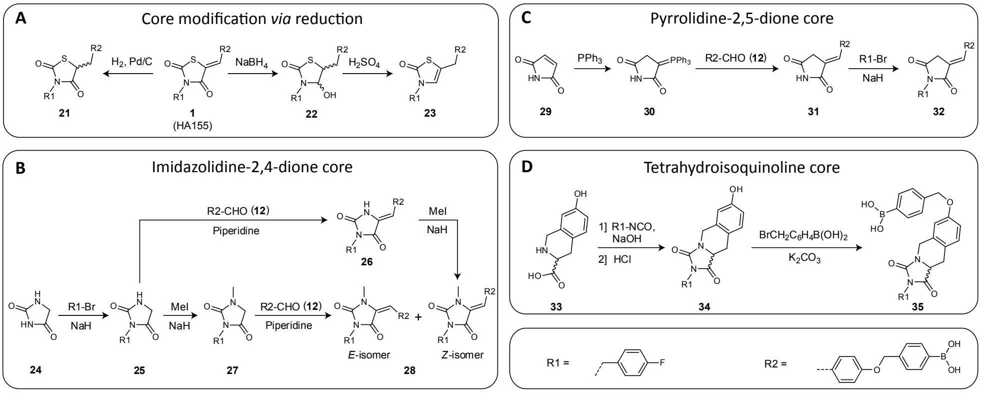
A
Core modification *via* reduction
H2, Pd/C
NaBH4
H2SO4
21
1
(HA155)
22
23
B
Imidazolidine-2,4-dione core
R2-CHO (12)
Piperidine
MeI
NaH
R1-Br
NaH
MeI
NaH
R2-CHO (12)
Piperidine
24
25
26
27
E-isomer
28
Z-isomer
C
Pyrrolidine-2,5-dione core
PPh3
R2-CHO (12)
R1-Br
NaH
29
30
31
32
D
Tetrahydroisoquinoline core
1] R1-NCO, NaOH
2] HCl
BrCH2C6H4B(OH)2
K2CO3
33
34
35
R1 =
R2 =

Scheme 3: Synthetic routes toward core modified inhibitors.

For the syntheses of imidazolidine-2,4-dione-based inhibitors **26** and **28**, imidazolidine-2,4-dione (**24**) was mono *N*-alkylated with 4-fluorobenzyl bromide to give intermediate **25** (Scheme 3B). Reaction of **25** by a Knoevenagel condensation with aldehyde **12** selectively resulted in the formation of the *Z*-isomer of **26**. In parallel, intermediate **25** was methylated to give compound **27**. Finally, **27** was condensed with aldehyde **12** resulting in target molecule **28**. Both the *Z*- and *E*-isomers were formed in a 1:4 (*Z*:*E*) ratio. To obtain and isolate solely the *Z*-isomer **28**, we *N*-methylated compound **26**.

Core-hopping from thiazolidine-2,4-dione to pyrrolidine-2,5-dione is depicted in Scheme 3C. The route starts with the formation of a Wittig reagent starting from 2,5-pyrroledione (**29**), which is reacted with triphenylphosphine to form ylide **30**.[14] The Wittig reaction of the carbonyl stabilized ylide **30** with aldehyde **12** selectively leads to the *E*-isomer of intermediate **31** as expected. Finally, compound **31** is *N*-alkylated with 4-fluorobenzyl bromide resulting in the pyrrolidine-2,5-dione product **32**.

For the synthesis of a final tetrahydroisoquinoline-based core with a more rigid structure, the secondary amine in *R*- or *S*-tetrahydroisoquinoline **33** is reacted with 4-fluorobenzyl isocyanate in the presence of sodium hydroxide to form a urea intermediate (Scheme 3D). The imidazolidine ring is then formed upon acidification with hydrochloric acid, resulting in compound *R*- or *S*-**34**. In the final step, intermediate **34** is *O*-alkylated with 4-(bromomethyl)phenylboronic acid resulting in *R*- or *S*-**35**.

4.2.3 Structure-activity relations of inhibitors and autotaxin

Activity of the new molecules resulting from the linker and core modifications were determined in an LPC hydrolysis assay described previously,[11,15] in which ATX-mediated release of choline from LPC is detected by a two-step enzymatic colorimetric reaction. The IC_{50} values observed for inhibitors with modified linkers and cores are listed in Tables 1 and 2.

Table 1. IC_{50} values of the inhibitors resulting from the linker modification.

Entry	Structure	IC_{50} (nM) [a]
1	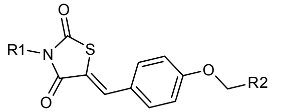	5.7 ± 0.4
17	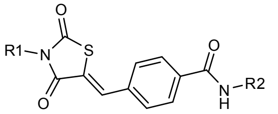	147 ± 47 [b]
18	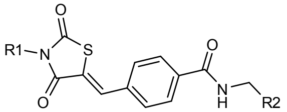	71 ± 17
19	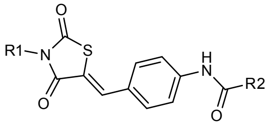	10 ± 1
36	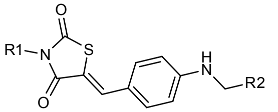	8.3 ± 0.9
20	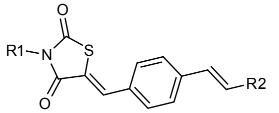	> 5,000

R1 = 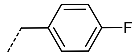 R2 = 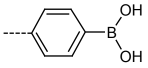

[a] IC_{50} values have been determined in the choline release assay using 40 µM LPC and 10 nM ATX. [b] The dose-response curve of inhibitor **17** shows biphasic curve (see Supporting Figure S2).

When we replaced the ether moiety (OCH_2, inhibitor **1**, IC_{50} = 5.7 nM) for an amide linker (CONH, **17**), we observed a significant loss of activity (IC_{50} = 147 nM). The dose-response curve of inhibitor **17** shows a biphasic curve[16] that could suggest several binding sites of this inhibitor for ATX (Supporting Figure S2). Expanding the CONH linker (**17**) to a more flexible $CONHCH_2$ linker (**18**) improved the IC_{50} value (71 nM) by two-fold compared to inhibitor **17**. Reversing the amide linker in **17** to yield compound **19**, results in high potency (IC_{50} = 10 nM), similar to inhibitor **1**. However, inhibitor **19** is not able to achieve full inhibition and 10% residual ATX activity is observed (Supporting Figure S3). Apparently, a more rigid amide linker results in suboptimal binding of the inhibitor. Therefore, we synthesized the more flexible amine analogue **36** (for the synthesis of inhibitor **36** see Supporting Information). This resulted indeed in a potent inhibitor (IC_{50} = 8.3 nM), similar to **1**, and with no residual ATX activity (Supporting Figure S3). Introduction of an (*E*)-CH=CH linker resulted in compound **20**, which was inactive in the nanomolar range (IC_{50} > 5 µM). This observation can be explained by the fact that the two aromatic rings linked with a flexible OCH_2 linker in inhibitor **1** are positioned in an angle of roughly 90° in the ATX structure (see Figure 1B) which cannot be achieved by the (*E*)-CH=CH linker due to its rigid planar conformation.

Next, we explored the activity of compounds with a modified core (Table 2) in combination with the OCH_2 linker, which had the highest activity of the linker modified molecules in Table 1. Reducing the carbon double bond in **1** resulted in little loss of activity in **21** with an IC_{50} value of 25 nM. Thus, although rigidity is preferred, the Michael acceptor can easily be removed without significant loss in activity. Reducing both the carbon double bond and the neighboring carbonyl in inhibitor **1** to hemiaminal **22**, led to a significant loss in potency (IC_{50} = 1.6 µM). Inhibitor **23**, where the hydroxyl moiety in compound **22** is removed is not very potent either (IC_{50} = 683 nM), indicates that the carbonyl moiety is important for binding. It appears from the crystal structure of inhibitor **1** bound to ATX that π-stacking between the phenyl ring of phenylalanine residue 274 (F274) and the carbonyl moiety in **1** is very likely seen their distance (4.1 Å, Supporting Figure S4).[17] By removing the carbonyl moiety in **1** or by changing it into a hydroxyl moiety, π-stacking will be lost resulting in lower potencies as observed for inhibitor **22** and **23**.

Table 2. IC_{50} values of the inhibitors resulting from the core modification.

Entry	Structure	IC_{50} (nM) [a]
1	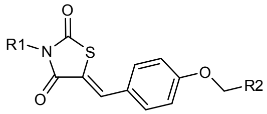	5.7 ± 0.4
21	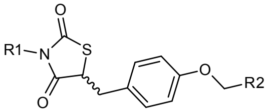	25 ± 2
22	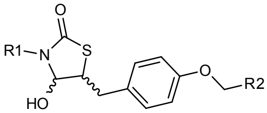	1594 ± 140
23	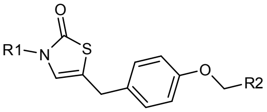	683 ± 88
26	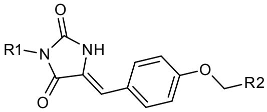	26 ± 4
E-**28**	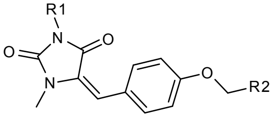	5.3 ± 0.5 [b]
Z-**28**	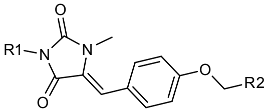	6.7 ± 0.4
32	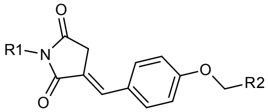	7.3 ± 0.5
S-**35**	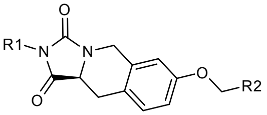	55 ± 9
R-**35**	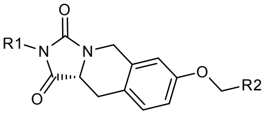	59 ± 7

R1 = 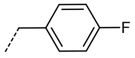 R2 = 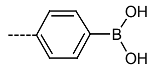

[a] IC_{50} values have been determined in the choline release assay using 40 µM LPC and 10 nM ATX. [b] *E*-**28** contains 20% of the *Z*-isomer.

The sulfur heteroatom in the thiazolidine-2,4-dione core was replaced with other atoms and moieties. We started by replacing the sulfur atom in **1** with a methylene moiety gives compound **32** with an IC_{50} value of 7.3 nM, comparable to inhibitor **1**. Replacement of the sulfur atom for an amino group (**26**, IC_{50} = 26 nM) resulted in little loss in activity compared to inhibitor **1**. When the amine in compound **26** is methylated, potency for the resulting inhibitor *Z*-**28** (IC_{50} = 6.7 nM) is slightly increased. Interestingly, the *E*-isomer of **28** (IC_{50} = 5.3 nM) is marginally more potent than *Z*-**28** or inhibitor **1**, a finding that we did not anticipate.

Intrigued by the characteristics of inhibitors *Z*-**28** and *E*-**28**, we decided to calculate likely binding poses using molecular docking. In molecular docking the binding of the inhibitor to the protein is predicted by optimizing the inhibitor's conformation such that the free energy of the overall system is minimized.

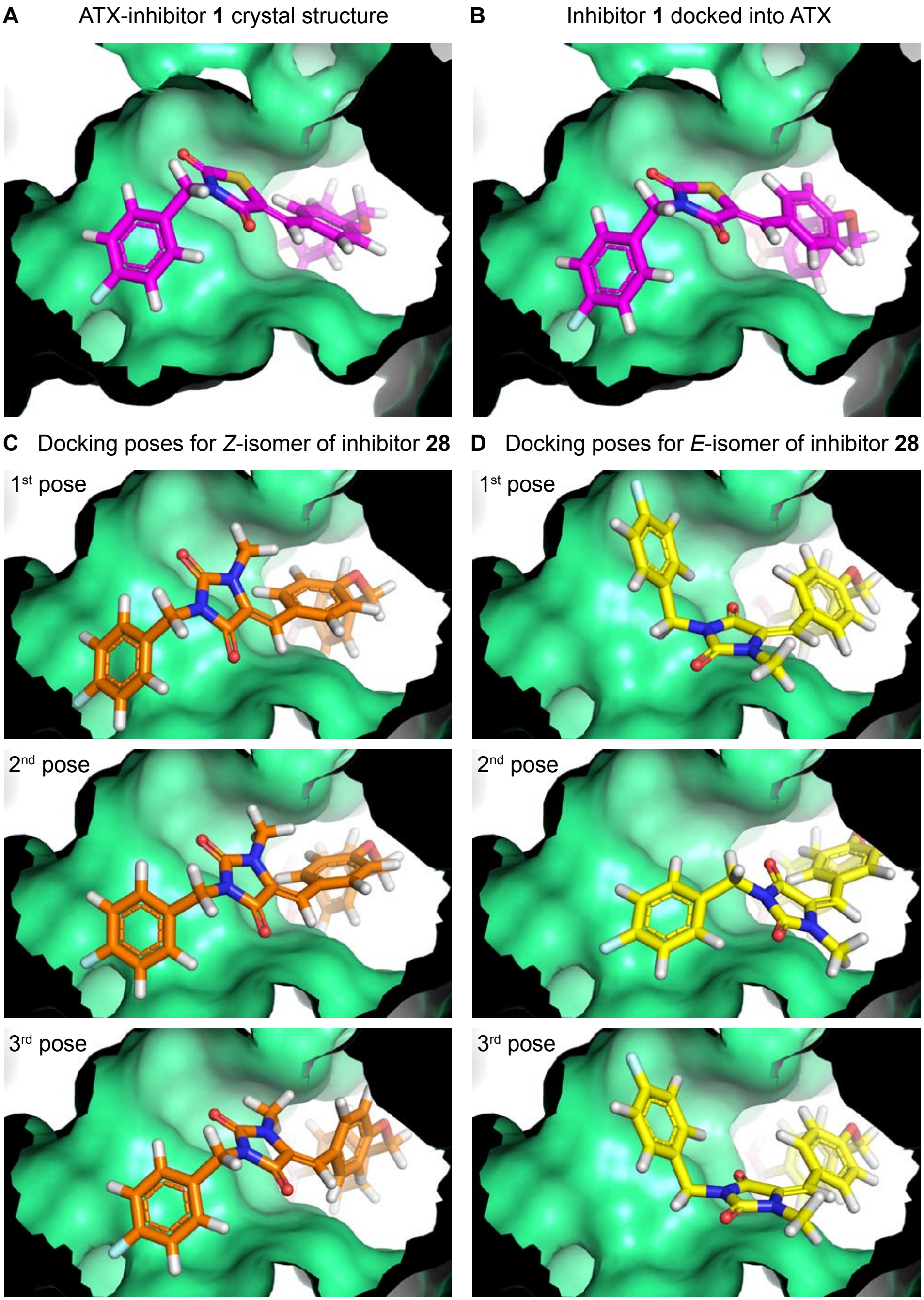
A
ATX-inhibitor 1 crystal structure
B
Inhibitor 1 docked into ATX
C
Docking poses for Z-isomer of inhibitor 28
D
Docking poses for E-isomer of inhibitor 28
1st pose
2nd pose
3rd pose
1st pose
2nd pose
3rd pose

Figure 2: (A) Focus from inside the protein on the thiazolidine-2,4-dione core of inhibitor **1** bound to ATX. (B) Inhibitor **1** docked into the active site of ATX to validate our docking approach. (C) The three best docking poses for the *Z*-isomer of **28**. (D) The three best docking poses for the *E*-isomer of **28**. Docking poses were generated using the docking program Glide.

For this purpose, we used the Glide docking software because it can dock boron-containing inhibitors.[18-20] Many docking programs, like AutoDock, can not dock boron-containing inhibitors because the boron atom is not defined in the software. To validate our docking approach where we constrain the boronic acid moiety, we first docked inhibitor **1** back into the ATX active site, resulting in a pose (Figure 2B) very similar to the original crystal structure (Figure 2A) with a root-mean-square deviation (RMSD) of 1.1 Å (for superimposed image see Supporting Figure S5). Next, we docked the *Z*- and *E*-isomers of inhibitor **28** (the three best docking poses are depicted in Figure 2C and D). The docking poses of *Z*-**28** are similar to the original pose of inhibitor **1** in the ATX structure. However, two of the best three docking poses for *E*-**28** suggest that the 4-fluorobenzyl moiety likely binds to a different area in the hydrophobic pocket (Figure 2D). The imidazolidine-2,4-dione core of *E*-**28** is flipped around the double bond axis in the ATX binding site compared to its *Z*-isomer (compare Figure 2C with D). This observation is in agreement with the conformations of both isomers. In addition, the binding poses of *Z*-**28** and *E*-**28** resulting from our docking study suggest that the current 4-fluorobenzyl moiety could be expanded from the methylene moiety in the 4-fluorobenzyl moiety with other substituents in future ATX inhibitors.

Finally, we evaluated inhibitors in which we introduced a rigidified three-ring system (Table 2) incorporating a tetrahydroisoquinoline motif that we deemed likely to bind. This modification avoids the presence of a Michael acceptor, while introducing rigidity and a new core structure. This modification resulted in the chiral inhibitor **35**, which is still very potent although some activity is lost compared to **1**. No significant difference is observed in potency between the *S*- and *R*-enantiomers of inhibitor **35**, with IC_{50} values of 55 and 59 nM, respectively.

In summary, we explored structure-activity relations building on boronic acid-based ATX inhibitor **1**, which resulted in a number of potent inhibitors. We used the crystal structure of ATX liganded with inhibitor **1** to explain the structure-activity relationships observed for a rational inhibitor modification approach. Our results suggest that this approach allows rapid structure guided modification. Finally, molecular docking efforts proved useful to explain unexpected high potency of *E*-isomer **28** and suggested that the lipophilic pocket near the ATX active site may be better exploited in the future for the design of new inhibitors.

4.3 Experimental section

General. The *S*- and *R*-enantiomers of building block **33** were purchased from CSPS Pharmaceuticals, San Diego, USA. All other chemicals were obtained from Sigma-Aldrich and used without further purification unless otherwise noted. Analytical thin layer chromatography was performed on aluminum sheets precoated with silica gel 60 F_{254}. Column chromatography was carried out on silica gel (0.035-0.070, 90 Å, Acros).

For isolation by centrifugation a Heraeus Multifuge 3 $_{S-R}$ centrifuge was used. Products were spun at 4400*g* at 298 K for 5 min. Nuclear magnetic resonance spectra (^{1}H and ^{13}C NMR) were determined in deuterated dimethyl sulfoxide (d_6-DMSO) using a Bruker Avance 300 (^{1}H: 300 MHz; ^{13}C: 75 MHz) at 298 K, unless indicated otherwise. Peak shapes are indicated with the symbols 'd' (doublet), 'dd' (double doublet), 's' (singlet), 'bs' (broad singlet) and 'm' (multiplet). Chemical shifts (δ) are given in ppm and coupling constants *J* in Hz. Dimethyl sulfoxide (δ_H = 2.50 ppm; δ_C = 39.51 ppm) was used as internal reference.

The purity of all tested compounds was determined by high-performance liquid chromatography coupled to mass spectrometry (HPLC-MS) and was greater than 95%. HPLC-MS measurements were performed on a system equipped with a Waters 2795 Seperation Module (Alliance HT), Waters 2996 Photodiode Array Detector (190-750 nm), Atlantis® T3 C18 column (2.1 mm x 100 mm, 3 µm) and an LCT™ Orthogonal Acceleration Time of Flight Mass Spectrometer. Samples were run at a flowrate of 0.40 mL min^{-1} at 313 K, using gradient elution (water/acetonitrile/formic acid) from 950/50/1 (*v*/*v*/*v*) to 50/950/1 (*v*/*v*/*v*).

The preparative HPLC system was equipped with a Waters 1525 Binary HPLC Pump, a Waters 2487 Dual *λ* Absorbance Detector and an Atlantis® C18 column (19 mm × 250 mm, 10 µm). Samples were run at a flowrate of 18 mL min^{-1} using gradient elution (water/acetonitrile) from 6/4 (*v*/*v*) to 1/9 (*v*/*v*).

General procedure for borylation of aldehydes and pinacol deprotection (12-16).
In a dry flask, bis(pinacolato)diboron (1.34 g, 5.28 mmol), the appropriate aldehyde (1.80 mmol) and potassium acetate (0.542 g, 5.52 mmol) were added to a solution of Pd(dppf)Cl_2 (46.6 mg, 0.0637 mmol) in dimethylformamide (15 mL). The reaction mixture was stirred under an atmosphere of argon for 18 h at 353 K. The reaction mixture was filtered over Hyflo Super Cel® medium and diluted with ethyl acetate (100 mL). The solution was washed with brine (50 mL and 25 mL), dried over magnesium sulfate and was concentrated.

The crude product was dissolved in tetrahydrofuran (11 mL) and sodium periodate (2.22 g, 10.4 mmol) and water (2.8 mL) were added. After stirring for 30 min, 1 M hydrochloric acid (1.1 mL) was added, and after 2 h, additional sodium periodate (1.17 g, 5.47 mmol) was added and the solution was stirred for another 2 h. The reaction mixture was diluted with ethyl acetate (20 mL) and washed with water (10 mL). The water layer was extracted with ethyl acetate (15 mL). The combined organic layers were washed with brine (15 mL), dried over magnesium sulfate and the solution was concentrated under vacuum resulting in a light yellow solid. The resulting product was used without further purification.

(4-((4-formylphenoxy)methyl)phenyl)boronic acid (12). Yield: 70%. **^{1}H NMR:** δ = 9.86 (s, 1H), 8.09 (s, 1H), 7.87 (d, *J* = 8.8, 1H), 7.82 (d, *J* = 8.1, 1H), 7.42 (d, *J* = 8.1, 1H), 7.20 (d, *J* = 8.7, 1H), 5.24 (s, 1H). **^{13}C NMR:** δ = 191.75, 163.73, 138.49, 134.74, 132.26, 130.22, 127.15, 115.76, 70.09, 39.95 (C-B$(OH)_2$ not visible). **MS:** m/z $[M+H]^+$ calc. 257.10, obs. 257.10.

(4-(4-formylbenzamido)phenyl)boronic acid (13). Yield: 81%. **^{1}H NMR:** δ = 10.47 (s, 1H), 10.12 (s, 1H), 8.13 (d, *J* = 8.3, 2H), 8.06 (d, *J* = 8.5, 2H), 7.95 (s, 2H), 7.80 (d, *J* = 8.7, 2H), 7.75 (d, *J* = 8.7, 2H).

^{13}C NMR: δ = 192.86, 164.74, 140.64, 139.93, 137.94, 134.70, 129.37, 128.38, 119.08 (C-B(OH)$_2$ not visible). **MS:** m/z [M+H]$^+$ calc. 270.09, obs. 270.11.

(4-((4-formylbenzamido)methyl)phenyl)boronic acid (14). Yield: 72%. **^{1}H NMR:** δ = 10.09 (s, 1H), 9.25 (t, *J* = 5.9, 1H), 8.08 (d, *J* = 8.3, 2H), 8.01 (d, *J* = 8.5, 2H), 7.75 (d, *J* = 8.1, 2H), 7.29 (d, *J* = 8.1, 2H), 4.51 (d, *J* = 5.9, 2H). **^{13}C NMR:** δ = 192.85, 165.39, 141.10, 139.33, 137.74, 134.14, 129.39, 127.96, 126.21, 42.78 (C-B(OH)$_2$ not visible). **MS:** m/z [M+H]$^+$ calc. 284.11, obs. 284.11.

(4-((4-formylphenyl)carbamoyl)phenyl)boronic acid (15). Yield: 72%. **^{1}H NMR:** δ = 10.62 (s, 1H), 9.92 (s, 1H), 8.26 (bs, 2H), 8.05-7.90 (m, 8H). **^{13}C NMR:** δ = 191.61, 166.22, 144.79, 135.65, 134.00, 131.57, 130.59, 126.66, 119.82 (C-B(OH)$_2$ not visible). **MS:** m/z [M+H]$^+$ calc. 270.09, obs. 270.11.

(*E*)-(4-(4-formylstyryl)phenyl)boronic acid (16). Yield: 75%. **^{1}H NMR:** δ = 9.99 (s, 1H), 8.06 (s, *2*H), 7.97 – 7.57 (m, 8H), 7.45 (dd, *J* = 16, 1H). **^{13}C NMR:** δ = 192.34, 143.05, 137.94, 135.08, 134.53, 131.97, 129.98, 127.72, 127.02, 125.91 (C-B(OH)$_2$ not visible). **MS:** m/z [M+H]$^+$ calc. 253.10, obs. 253.13.

General method for Knoevenagel condensation (1, 17-20, 26 and *E*-28).
To a solution of 3-(4-fluorobenzyl)thiazolidine-2,4-dione (0.293 mmol) in ethanol (2.5 mL), piperidine (20 μL, 0.207 mmol) and the appropriate aldehyde (0.352 mmol) were added and the solution was refluxed for 22 h.

(*Z*)-4-[(4-{[3-(4-fluorobenzyl)-2,4-dioxo-1,3-thiazolan-5-yliden]methyl}phenoxy) methyl]benzene boronic acid (1). Upon cooling the reaction mixture to room temperature the product precipitated out of solution. Dissolving the product in dimethyl sulfoxide and precipitating it with 0.5 M hydrochloric acid resulted in pure compound. **Yield:** 81%. **^{1}H NMR**: δ = 8.03 (s, 2H), 7.92 (s, 1H), 7.80 (d, *J* = 8.1, 2H), 7.60 (d, *J* = 8.9, 2H), 7.41 (d, *J* = 8.0, 2H), 7.39 – 7.31 (m, *J* = 5.5, 8.8, 2H), 7.26 – 7.09 (m, *J* = 4.5, 8.9, 4H), 5.21 (s, 2H), 4.82 (s, 2H). **^{13}C NMR:** δ = 167.38, 165.59, 161.66 (d, $^1J_{CF}$ = 244), 160.33, 138.19, 134.28, 133.48, 132.33, 131.81 (d, $^4J_{CF}$ = 3), 129.95 (d, $^3J_{CF}$ = 8), 126.67, 125.55, 117.89, 115.81, 115.47 (d, $^2J_{CF}$ = 21), 69.52, 43.90 (C-B(OH)$_2$ not visible). **MS**: m/z [M+H]$^+$ calc. 464.11, obs. 464.19.

(*Z*)-(4-(4-((3-(4-fluorobenzyl)-2,4-dioxothiazolidin-5-ylidene)methyl)benzamido) phenyl)boronic acid (17). Upon cooling the reaction mixture to room temperature the product precipitated out of solution. Crude compound was recrystallized from a dichloromethane/methanol mixture (4:1). **Yield:** 60%. **^{1}H NMR:** δ = 10.39 (s, 1H), 8.10-8.04 (m, 3H), 7.94 (s, 2H), 7.80-7.76 (m, 6H), 7.40-7.37 (m, 2H), 7.22-7.16 (m, 2H), 4.84 (s, 2H). **^{13}C NMR:** δ = 167.12, 165.34, 164.66, 161.66 (d, $^1J_{CF}$ = 244), 140.57, 136.23, 135.68, 134.69, 132.23, 131.60 (d, $^4J_{CF}$ = 3), 129.95 (d, $^3J_{CF}$ = 8), 129.94, 128.53, 123.04, 119.01, 115.42 (d, $^2J_{CF}$ = 21), 44.04 (C-B(OH)$_2$ not visible). **MS:** m/z [M+H]$^+$ calc. 477.11, obs. 477.08.

(*Z*)-(4-((4-((3-(4-fluorobenzyl)-2,4-dioxothiazolidin-5-ylidene)methyl)benzamido) methyl)phenyl) boronic acid (18). Title compound was purified using preparative HPLC. **Yield:** 5%. **^{1}H NMR:** δ = 9.17 (t, *J* 6.0, 1H), 8.04-8.00 (m, 3H), 7.97 (s, 2H), 7.74-7.70 (m, 4H), 7.41-7.16 (m, 6H), 4.83 (s, 2H), 4.50 (d, *J* 5.8, 2H). **^{13}C NMR:** δ = 167.15, 165.35, 165.32, 161.66 (d, $^1J_{CF}$ = 244), 141.21, 135.64, 135.41, 134.13, 132.30, 131.58 (d, $^4J_{CF}$ = 3), 129.94 (d, $^3J_{CF}$ = 8), 129.89, 128.11, 126.17, 122.82, 115.42 (d, $^2J_{CF}$ = 21), 44.02, 42.72 (C-B(OH)$_2$ not visible). **MS:** m/z [M+H]$^+$ calc. 491.12, obs. 491.17.

(*Z*)-(4-((4-((3-(4-fluorobenzyl)-2,4-dioxothiazolidin-5-ylidene)methyl)phenyl)carbamoyl)phenyl) boronic acid (19). Title compound was purified using preparative HPLC. **Yield:** 21%. **^{1}H NMR:** δ =10.56 (s, 1H), 8.25 (s, 2H), 8.00 (d, *J* 8.8, 2H), 7.93 (m, 5H), 7.66 (d, *J* = 8.8, 2H), 7.40-7.35 (m, 2H), 7.22-7.16

(m, 2H), 4.83 (s, 2H). **^{13}C NMR:** δ = 167.38, 166.05, 165.58, 161.64 (d, $^{1}J_{CF}$ = 244), 141.53, 135.73, 134.00, 132.20, 131.76 (d, $^{4}J_{CF}$ = 3), 131.20, 129.92 (d, $^{3}J_{CF}$ = 8), 127.84, 126.61, 120.39, 118.97), 115.44 (d, $^{2}J_{CF}$ = 21), 43.89 (C-$B(OH)_2$ not visible). **MS:** m/z $[M+H]^+$ calc. 477.11, obs. 477.18.

(4-((*E*)-4-((*Z*)-(3-(4-fluorobenzyl)-2,4-dioxothiazolidin-5-ylidene)methyl)styryl)phenyl)boronic acid (20). Upon cooling the reaction mixture to room temperature the product precipitated out of solution. Dissolving the product in dimethyl sulfoxide and precipitating it with 0.5 M hydrochloric acid resulted in pure compound. **Yield:** 47%. **^{1}H NMR:** δ = δ 8.04 (s, 2H), 7.96 (s, 1H), 7.88 – 7.52 (m, 8H), 7.49 – 7.12 (m, 6H), 4.83 (s, 2H). **^{13}C NMR:** δ = 167.20, 165.48, 161.64 (d, $^{1}J_{CF}$ = 244), 139.43, 138.09, 134.52, 133.01, 131.94, 131.69 (d, $^{4}J_{CF}$ = 3), 130.93, 130.71, 129.91 (d, $^{3}J_{CF}$ = 8), 127.78, 127.29, 125.77, 120.38, 115.42 (d, $^{2}J_{CF}$ = 21), 43.94 (C-$B(OH)_2$ not visible). **MS:** m/z $[M+H]^+$ calc. 460.10, obs. 460.06.

(*Z*)-(4-((4-((1-(4-fluorobenzyl)-2,5-dioxoimidazolidin-4-ylidene)methyl)phenoxy)methyl)phenyl) boronic acid (26). Final product was isolated by using preparative HPLC. *Z*-configuration confirmed by the chemical shift of the vinyl and amine proton reported in literature.[21] **Yield:** 15%. **^{1}H NMR:** δ = 10.68 (s, 1H), 8.06 (s, 2H), 7.80 (d, *J* = 8.1, 2H), 7.62 (d, *J* = 8.9, 2H), 7.41 (d, *J* = 8.1, 2H), 7.39 – 7.28 (m, 2H), 7.24 – 7.10 (m, 2H), 7.04 (d, *J* = 8.9, 2H), 6.54 (s, 1H), 5.17 (s, 2H), 4.65 (s, 2H). **^{13}C NMR:** δ = 164.02, 161.49 (d, $^{1}J_{CF}$ = 244), 158.72, 154.89, 138.54, 134.22, 132.83 (d, $^{4}J_{CF}$ = 3), 131.30, 129.63 (d, $^{3}J_{CF}$ = 8), 126.55, 125.43, 115.35 (d, $^{2}J_{CF}$ = 21), 110.30, 69.28, 40.60 (C-$B(OH)_2$ not visible). **MS:** m/z $[M+H]^+$ calc. 447.15, obs. 447.25.

(*E*)-(4-((4-((1-(4-fluorobenzyl)-3-methyl-2,5-dioxoimidazolidin-4-ylidene)methyl)phenoxy)methyl) phenyl)boronic acid (*E*-28). Title compound was purified using preparative HPLC. *E*-**28** contains 20% of the *Z*-isomers which could not be separated. *E*-configuration confirmed by the chemical shift of the vinyl and methyl proton reported in literature.[22] **Yield:** 28%. **^{1}H NMR:** δ = 8.04 (s, 2H), 8.01 (d, *J* = 9.0, 2H), 7.80 (d, *J* = 8.0, 2H), 7.41 (d, *J* = 7.9, 2H), 7.38 – 7.32 (m, 2H), 7.23 – 6.98 (m, 4H), 6.52 (s, 1H), 5.16 (s, 2H), 4.65 (s, 2H), 3.15 (s, 3H), . **^{13}C NMR:** δ = 161.49 (d, $^{1}J_{CF}$ = 244), 161.18, 158.80, 152.62, 138.54, 134.20, 132.74 (d, $^{4}J_{CF}$ = 3), 132.08, 129.83 (d, $^{3}J_{CF}$ = 8), 127.23, 126.59, 125.57, 117.51, 115.31 (d, $^{2}J_{CF}$ = 21), 114.41, 69.23, 40.78, 26.36 (C-$B(OH)_2$ not visible). **MS:** m/z $[M+H]^+$ calc. 461.17, obs. 461.19.

(4-((4-((3-(4-fluorobenzyl)-2,4-dioxothiazolidin-5-yl)methyl)phenoxy)methyl) phenyl)boronic acid (21). A mixture of compound **1** (50.1 mg, 0.108 mmol) and 10 wt% Pd/C (24.0 mg) in degassed methanol (3 mL) was stirred under a hydrogen atmosphere for 2 h. Extra 10 wt% Pd/C was added (12.0 mg) and the reaction was allowed to continue for one night. The mixture was filtrated and concentrated to dryness. Preparative HPLC afforded the title compound. **Yield:** 18.3 mg, 77%. **^{1}H NMR:** δ = 8.03 (s, 2H), 7.80 (d, *J* = 8.1, 2H), 7.39 (d, *J* = 8.1, 2H), 7.28 – 6.99 (m, 6H), 6.88 (d, *J* = 8.7, 2H), 5.06 (s, 2H), 5.00 (dd, *J* = 4.4, 8.0, 1H), 4.60 (dd, *J* = 15.0, 21.5, 2H), 3.14 (dd, *J* = 8.0, 14.2, 1H). **^{13}C NMR:** δ = 173.71, 171.00, 161.50 (d, $^{1}J_{CF}$ = 244), 157.44, 138.74, 134.16, 131.58 (d, $^{4}J_{CF}$ = 3), 130.56, 129.66 (d, $^{3}J_{CF}$ = 8), 127.98, 126.52, 115.21 (d, $^{2}J_{CF}$ = 21), 114.57, 69.12, 50.94, 43.56, 35.79 (C-$B(OH)_2$ not visible). **MS:** m/z $[M+H]^+$ calc. 466.13, obs. 466.25, $[M-H_2O+H]^+$ calc. 448.12, obs. 448.23.

(4-((4-((3-(4-fluorobenzyl)-4-hydroxy-2-oxothiazolidin-5-yl)methyl)phenoxy) methyl)phenyl)boronic acid (22). To a solution of compound **1** (50.0 mg, 0.108 mmol) in dimethyl sulfoxide (0.5 mL), sodium borohydride (16.3 mg, 0.430 mmol) was slowly added. After 9 h of stirring the reaction mixture was diluted with ethyl acetate (4 mL) and was washed with water (2x2 mL). The organic layer was dried over calcium chloride and concentrated *in vacuo*, resulting in the title compound. **Yield:** 30.2 mg, 60%. **^{1}H NMR:** δ = 8.06 (s, 2H), 7.80 (d, *J* = 8.1, 2H), 7.39 (d, *J* = 8.0, 2H), 7.36 – 7.11 (m, 5H), 6.94 (d,

J = 8.7, 2H), 6.87 (d, *J* = 8.7, 2H), 6.71 (d, *J* = 6.2, 1H), 5.06 (s, 2H), 4.72 (dd, *J* = 7.7, 15.1, 1H), 4.10 (d, *J* = 15.1, 1H), 3.67 (t, *J* = 7.9, 1H), 3.35 (s, 1H), 2.81 (dd, *J* = 7.3, 13.9, 1H), 2.70 (dd, *J* = 8.4, 13.9, 1H). **^{13}C NMR:** δ = 169.70, 161.55 (d, $^1J_{CF}$ = 244), 157.13, 138.85, 134.15, 133.14 (d, $^4J_{CF}$ = 3.0), 130.01, 130.00 (d, $^3J_{CF}$ = 8), 129.73, 126.54, 115.38 (d, $^2J_{CF}$ = 21), 114.64, 84.02, 69.11, 51.42, 44.02, 39.65. (C-B(OH)$_2$ not visible). **MS:** m/z [M+H]$^+$ calc. 468.15, obs. 468.23.

(4-((4-((3-(4-fluorobenzyl)-2-oxo-2,3-dihydrothiazol-5-yl)methyl)phenoxy) methyl)phenyl)boronic acid (23). To a solution of compound **1** (45.7 mg, 0.0989 mmol) in dimethyl sulfoxide (0.75 mL), sodium borohydride (29.1 mg, 0.769 mmol) was slowly added. After 7 h of stirring the reaction mixture, concentrated sulfuric acid (2x50 µl) was added over a 15 min interval. The reaction mixture was stirred for an additional 5 h. Ethyl acetate (25 mL) was added and the mixture was washed with water (4x10 mL). The organic layer was dried over calcium chloride and concentrated *in vacuo*, affording pure compound **23**. **Yield:** 31.8 mg, 72%. **^{1}H NMR:** δ =8.05 (s, 2H), 7.79 (d, *J* = 8.1, 2H), 7.38 (d, *J* = 8.1, 2H), 7.36 – 7.16 (m, 4H), 7.13 (d, *J* = 8.7, 2H), 6.95 (d, *J* = 8.7, 2H), 6.87 (s, 1H), 5.07 (s, 2H), 4.80 (s, 2H), 3.73 (s, 2H). **^{13}C NMR:** δ = 170.43, 161.61 (d, $^1J_{CF}$ = 244), 157.13, 138.85, 134.17, 133.10 (d, $^4J_{CF}$ = 3), 130.63, 130.63, 129.76 (d, $^3J_{CF}$ = 8), 129.42, 126.48, 121.56, 117.78, 115.50 (d, $^2J_{CF}$ = 21), 114.86, 69.16, 46.78, 32.91 (C-B(OH)$_2$ not visible). **MS:** m/z [M+H]$^+$ calc. 450.13, obs. 450.22.

3-(4-fluorobenzyl)imidazolidine-2,4-dione (25). To a cooled solution (273 K) of hydantoin (8.01 g, 80.1 mmol) in dimethylformamide (140 mL) sodium hydride (60% in oil, 1.80 g, 45.0 mmol) was added. A solution of 1-(bromomethyl)-4-fluorobenzene (5.0 mL, 41 mmol) in dimethylformamide (5 mL) was added to the reaction mixture. The mixture was allowed to warm up to room temperature and was stirred for 6 h. Then the mixture was poured into water (200 mL) and hexane (200 mL) was added. After a night at 277 K the precipitate was filtered and dried to give a white solid. **Yield:** 4.7 g, 56%. **^{1}H NMR:** δ = 8.14 (s, 1H), 7.45 – 7.21 (m, 1H), 7.26 – 7.09 (m, 1H), 4.51 (s, 2H), 3.97 (s, 2H). **^{13}C NMR:** δ = 171.91, 161.45 (d, $^1J_{CF}$ = 244), 157.29, 133.04 (d, $^4J_{CF}$ = 3), 129.66 (d, $^3J_{CF}$ = 8), 115.21 (d, $^2J_{CF}$ = 21), 46.00, 40.29. **MS:** m/z [M+H]$^+$ calc. 209.07, obs. 208.93.

3-(4-fluorobenzyl)-1-methylimidazolidine-2,4-dione (27). To a cooled solution (273 K) of 3-(4-fluorobenzyl)imidazolidine-2,4-dione (98.1 mg, 0.471 mmol) in dimethylformamide (0.5 mL), sodium hydride (60% in oil, 21.1 mg, 0.530 mmol) was added. Subsequently, iodomethane (33 µl, 0.53 mmol) was added to the reaction mixture. The mixture was allowed to warm up to room temperature and was stirred for 3 h. Then the mixture was poured into ice water (2.5 mL) and hexane (2.5 mL) was added. After a night at 277 K the precipitate was filtered and dried to give a white solid. **Yield:** 75 mg, 72%. **^{1}H NMR:** δ = 7.34-7.12 (m, 4H), 4.52 (s, 2H), 4.01 (s, 2H), 2.86 (s, 3H). **^{13}C NMR:** δ = 170.20, 161.46 (d, $^1J_{CF}$ = 244), 156.24, 132.92 (d, $^4J_{CF}$ = 3), 129.68 (d, $^3J_{CF}$ = 8) , 115.21 (d, $^2J_{CF}$ = 21), 51.36, 40.74, 29.21. **MS:** m/z [M+H]$^+$ calc. 223.09, obs. 223.06.

(*Z*)-(4-((4-((1-(4-fluorobenzyl)-3-methyl-2,5-dioxoimidazolidin-4-ylidene)methyl) phenoxy)methyl)phenyl) boronic acid (*Z*-28). To a cooled solution (273 K) of hydantoin **26** (10.1 mg, 0.0224 mmol) and sodium hydride (60% in oil, 1.46 mg, 0.0365 mmol) in DMF (0.15 ml), iodomethane (2.25 µl, 0.0361 mmol) was added. The mixture was allowed to warm up to room temperature and was stirred for 4 h. Final product was isolated by using preparative HPLC. *Z*-configuration confirmed by the chemical shift of the vinyl and methyl proton reported in literature.[22] **Yield:** 6.97 mg, 68%. **^{1}H NMR:** δ = 8.11 (s, 1H), 7.80 (d, *J* = 8.1, 2H), 7.50 – 7.30 (m, 6H), 7.26 – 7.10 (m, 2H), 7.05 (d, *J* = 8.8, 2H), 6.76 (s, 1H), 5.14 (s, 2H), 4.67 (s, 2H), 2.92 (s, 3H). **^{13}C NMR:** δ = 163.01, 159.92, 156.78 (d, $^1J_{CF}$ = 249), 138.52, 134.19, 132.55 (d, $^4J_{CF}$ = 3), 131.28, 129.75 (d, $^3J_{CF}$ = 8), 128.50, 126.58, 124.66, 115.31 (d, $^2J_{CF}$ = 21), 114.55, 111.56, 69.30, 41.12, 30.35 (C-B(OH)$_2$ not visible). **MS:** m/z [M+H]$^+$ calc. 461.17, obs. 461.12.

(*E*)-(4-((4-((2,5-dioxopyrrolidin-3-ylidene)methyl)phenoxy)methyl)phenyl) boronic acid (31). To a heated (343 K) solution of compound **30** (159 mg, 0.442 mmol)[14] in methanol (5 mL) aldehyde 12 (106 mg, 0.414 mmol) was added. After 1 h of heating the reaction mixture was cooled using an ice bath resulting in precipitation of the title compound. The precipitate was filtered and washed with ice-cold methanol resulting in compound **31**. **Yield:** 88 mg, 63%. **^{1}H NMR:** δ = 11.34 (s, 1H), 8.04 (s, 2H), 7.80 (d, J = 8.0, 2H), 7.57 (d, J = 8.9, 2H), 7.41 (d, J = 8.0, 2H), 7.33 (t, ^{4}J = 2.1, 1H), 7.10 (d, J = 8.8, 2H), 5.19 (s, 2H), 3.60 (d, ^{4}J = 2.2, 2H). **^{13}C NMR:** δ = 175.80, 172.09, 159.47, 138.42, 134.22, 132.00, 131.31, 126.96, 126.54, 124.16, 115.31, 69.31, 34.71 (C-B(OH)$_2$ not visible). **MS:** m/z [M+H]$^+$ calc. 338.12, obs. 338.11.

(*E*)-(4-((4-((1-(4-fluorobenzyl)-2,5-dioxopyrrolidin-3-ylidene)methyl)phenoxy) methyl)phenyl) boronic acid (32). To a solution of compound **31** (30 mg, 0.0890 mmol) in dimethylformamide (0.3 mL) sodium hydride (60% in oil, 3.65 mg, 0.0913 mmol) was added. After addition of 4-fluorobenzyl bromide (24 µl, 0.19 mmol), the reaction mixture was stirred for 4 h. In addition, potassium carbonate (2.04 mg, 0.0148 mmol) was added and the reaction mixture was stirred overnight. Then the mixture was poured into ice water (0.9 mL) and hexane (0.3 mL) was added. After a night at 277 K the precipitate was filtered, dried and purified using preparative HPLC to give a white solid. *E*-configuration confirmed by the chemical shift of the vinyl proton reported in literature.[14] **Yield:** 13 mg, 32%. **^{1}H NMR:** δ = 8.04 (s, 2H), 7.80 (d, J = 8.1, 2H), 7.61 (d, J = 8.9, 2H), 7.45 (t, ^{4}J = 2.1, 1H), 7.41 (d, J = 8.0, 2H), 7.38 – 7.29 (m, 2H), 7.23 – 7.04 (m, 4H), 5.19 (s, 2H), 4.66 (s, 2H), 3.74 (d, ^{4}J = 2.1, 2H). **^{13}C NMR:** δ = 174.19, 170.59, 161.44 (d, $^{1}J_{CF}$ = 244), 159.65, 138.39, 134.22, 132.59 (d, $^{4}J_{CF}$ = 3), 132.31, 132.17, 129.73 (d, $^{3}J_{CF}$ = 8), 126.85, 126.54, 122.27, 115.36, 115.22 (d, $^{2}J_{CF}$ = 21), 69.33, 40.71, 33.74 (C-B(OH)$_2$ not visible). **MS:** m/z [M+H]$^+$ calc. 446.16, obs. 446.12.

(*S*)-2-(4-fluorobenzyl)-7-hydroxy-10,10a-dihydroimidazo[1,5-b]isoquinoline-1,3(2H,5H)-dione (*S*-34). Compound *S*-**33** (100 mg, 0.518 mmol) was dissolved in a mixture of dioxane and water (3:1, 4 mL) and 30 wt% of sodium hydroxide solution was used to adjust the pH to 14. The reaction mixture was heated to 313 K and 4-fluorobenzyl isocyanate (100 µL, 0.785 mmol) was added. After 2 h of stirring, the mixture was cooled to room temperature and the resulting solid was removed using centrifugation. From the resulting solution was dioxane evaporated and concentrated hydrochloric acid was used to adjust the pH to 1. After refluxing the reaction mixture for 2 h 30 it was cooled to 278 K affording a white precipitate. Washing the precipitate with ice-cold water (3x1 mL) afforded pure compound *S*-**34**. **Yield:** 30 mg, 18%. **^{1}H NMR:** δ = 9.37 (s, 1H), 7.35 – 7.30 (m, 2H), 7.18 – 7.12 (m, 2H), 7.06 – 7.03 (m, 1H), 6.65 – 6.63 (m, 2H), 4.77 (d, J = 16.8, 1H), 4.58 (s, 2H), 4.32 – 4.27 (m, 2H), 3.05 (m, 1H), 2.82 – 2.64 (m, 1H). **^{13}C NMR:** δ = 172.76, 161.44 (d, $^{1}J_{CF}$ = 244), 156.07, 154.60, 132.82 (d, $^{4}J_{CF}$ = 3), 132.35, 130.13, 129.51 (d, $^{3}J_{CF}$ = 8), 121.45, 115.26 (d, $^{2}J_{CF}$ = 21), 114.30, 112.67, 54.54, 41.23, 40.56, 29.02. **MS:** m/z [M+H]$^+$ calc. 327.11, obs. 327.09.

(*R*)-2-(4-fluorobenzyl)-7-hydroxy-10,10a-dihydroimidazo[1,5-b]isoquinoline-1,3(2H,5H)-dione (*R*-34). For reaction details see compound *S*-**34**. **Yield:** 29%.

(*S*)-(4-(((2-(4-fluorobenzyl)-1,3-dioxo-1,2,3,5,10,10a-hexahydroimidazo[1,5-b]isoquinolin-7-yl)oxy) methyl)phenyl)boronic acid (*S*-35). To a heated solution (323 K) of compound ***S*-34** (15.3 mg, 0.0469 mmol) in acetone (0.3 mL), potassium carbonate (10.2 mg, 0.0738 mmol) and 4-(bromomethyl) phenylboronic acid (12.4 mg, 0.0577 mmol) were added. After 4 h of stirring and heating, additional potassium carbonate (10.1 mg, 0.0730 mmol) was added and the suspension was stirred overnight. Finally, the reaction mixture was diluted with ethyl acetate and the organic layer was washed with 1 M hydrochloric acid (2x0.5 mL) and brine (0.5 mL), dried over sodium sulfate and concentrated *in vacuo*. The resulting solid was further purified using preparative HPLC affording pure compound ***S*-35**. **Yield:** 11 mg, 52%. **^{1}H NMR:** δ = 8.06 (s, 2H), 7.78 (d, *J* = 8.1, 2H), 7.50 – 7.27 (m, 4H), 7.27 – 7.05 (m, 3H), 7.02 – 6.76 (m, 2H), 5.09 (s, 2H), 4.82 (d, *J* = 17.0, 1H), 4.58 (s, 2H), 4.42 – 4.20 (m, 2H), 3.19 – 3.02 (m, 1H), 2.80 – 2.71 (m, 1H). **^{13}C NMR:** δ = 172.72, 161.46 (d, $^1J_{CF}$ = 244), 157.09, 154.60, 138.74, 134.17, 132.81 (d, $^4J_{CF}$ = 3), 132.60, 130.23, 129.55 (d, $^3J_{CF}$ = 8), 126.49, 123.60, 115.28 (d, $^2J_{CF}$ = 21), 113.87, 112.47, 69.20, 54.40, 41.30, 40.60, 29.00 (C-B$(OH)_2$ not visible). **MS:** m/z $[M+H]^+$ calc. 461.17, obs. 461.14.

(*R*)-(4-(((2-(4-fluorobenzyl)-1,3-dioxo-1,2,3,5,10,10a-hexahydroimidazo[1,5-b]isoquinolin-7-yl)oxy) methyl)phenyl)boronic acid (*R*-35). For reaction details see compound *S*-**35**. **Yield:** 56%.

Spectral data on compounds. Spectral data (HPLC-MS, ^{1}H and ^{13}C NMR profiles) of all intermediates and target molecules is available free of charge *via* the Internet at http://pubs.acs.org.

Choline release assay.[11] See Experimental section Chapter 3.

Docking Experiments, Protein and Ligand Preparation. The X-ray structure of ATX in complex with inhibitor **1** (PDB ID: 2XRG) was used for the docking studies. The protein structure was prepared using the Schrödinger Suite 2010 Protein Preparation Wizard (with Epik 2.1,[23] Impact 5.6 and Prime 2.2). The initial 3D structures of the ligands were generated using LigPrep 2.4 and the ligand partial charges were ascribed using the OPLS2005 force-field as performed by Glide 5.6.[18-20] We defined the binding region by a 20 Å x 20 Å x 20 Å box centered on the central position of inhibitor **1** in the crystal ATX complex. We used positional constraints for the two oxygen atoms of the boronic acid and the arylic carbon direct next to the boron atom in inhibitor **1**. The Glide Emodel score was used to rank the docking poses. Images were made using PyMOL 1.3.

4.4 References

1. Tokumura, A. et al. Identification of human plasma lysophospholipase D, a lysophosphatidic acid-producing enzyme, as autotaxin, a multifunctional phosphodiesterase. *J. Biol. Chem.* **277**, 39436-39442 (2002).
2. Umezu-Goto, M. et al. Autotaxin has lysophospholipase D activity leading to tumor cell growth and motility by lysophosphatidic acid production. *J. Cell. Biol.* **158**, 227-233 (2002).
3. Moolenaar, W. H. van Meeteren, L. A. & Giepmans, B. N. The ins and outs of lysophosphatidic acid signaling. *BioEssays* **26**, 870-881 (2004).
4. Kanda, H. et al. Autotaxin, an ectoenzyme that produces lysophosphatidic acid, promotes the entry of lymphocytes into secondary lymphoid organs. *Nat. Immunol.* **9**, 415-423 (2008).
5. van Meeteren, L. & Moolenaar, W. Regulation and biological activities of the autotaxin-LPA axis. *Prog. Lipid Res.* **46**, 145-160 (2007).
6. Tager, A. et al. The lysophosphatidic acid receptor LPA1 links pulmonary fibrosis to lung injury by mediating fibroblast recruitment and vascular leak. *Nat. Med.* **14**, 45-54 (2008).
7. Stefan, C. Jansen, S. & Bollen, M. Modulation of purinergic signaling by NPP-type ectophosphodiesterases. *Purinergic. Signal* **2**, 361-370 (2006).
8. Nishimasu, H. et al. Crystal structure of autotaxin and insight into GPCR activation by lipid mediators. *Nat. Struct. Mol. Biol.* **18**, 205-212 (2011).

9. Hausmann, J. et al. Structural basis of substrate discrimination and integrin binding by autotaxin. *Nat. Struct. Mol. Biol.* **18**, 198-204 (2011).
10. Gijsbers, R. Aoki, J. Arai, H. & Bollen, M. The hydrolysis of lysophospholipids and nucleotides by autotaxin (NPP2) involves a single catalytic site. *FEBS Lett.* **538**, 60-64 (2003).
11. Albers, H. M. et al. Discovery and Optimization of Boronic Acid Based Inhibitors of Autotaxin. *J. Med. Chem.* **53**, 4958-4967 (2010).
12. Albers, H. M. et al. Boronic acid-based inhibitor of autotaxin reveals rapid turnover of LPA in the circulation. *Proc. Natl. Acad. Sci. USA* **107**, 7257-7262 (2010).
13. Miyaura, N. & Suzuki, A. Palladium-Catalyzed Cross-Coupling Reactions of Organoboron Compounds. *Chem. Rev.* **95**, 2457-2483 (1995).
14. Mizufune, H. Nakamura, M. & Mitsudera, H. Process research on arylnaphthalene lignan aza-analogues: a new palladium-catalyzed benzannulation of α,β-bisbenzylidenesuccinic acid derivatives. *Tetrahedron* **62**, 8539-8549 (2006).
15. Cui, P. et al. Synthesis and biological evaluation of phosphonate derivatives as autotaxin (ATX) inhibitors. *Bioorg. Med. Chem. Lett.* **17**, 1634-1640 (2007).
16. Fischer, G. et al. Ro 25-6981, a Highly Potent and Selective Blocker of N-Methyl-d-aspartate Receptors Containing the NR2B Subunit. Characterization in Vitro. *J. Pharmacol. Exp. Ther.* **283**, 1285-1292 (1997).
17. Jain, A. Purohit, C. Verma, S. & Sankararamakrishnan, R. Close Contacts between Carbonyl Oxygen Atoms and Aromatic Centers in Protein Structures: $\pi-\pi$ or Lone-Pair-π Interactions? *J. Phys. Chem. B* **111**, 8680-8683 (2007).
18. Friesner, R. et al. Glide: A New Approach for Rapid, Accurate Docking and Scoring. 1. Method and Assessment of Docking Accuracy. *J. Med. Chem.* **47**, 1739-1749 (2004).
19. Friesner, R. et al. Extra Precision Glide: Docking and Scoring Incorporating a Model of Hydrophobic Enclosure for Protein-Ligand Complexes. *J. Med. Chem.* **49**, 6177-6196 (2006).
20. Halgren, T. et al. Glide: A New Approach for Rapid, Accurate Docking and Scoring. 2. Enrichment Factors in Database Screening. *J. Med. Chem.* **47**, 1750-1759 (2004).
21. Silva, T. G. et al. Synthesis and structural elucidation of new benzylidene imidazolidines and acridinylidene thiazolidines. *Heterocycl. Commun.* **7**, 523-528 (2001).
22. Tan, S. Ang, K. & Fong, Y. (*Z*)- and (*E*)-5-Arylmethylenehydantoins: spectroscopic properties and configuration assignment. *J. Chem. Soc., Perkin Trans. 2* 1941-1944 (1986).
23. Shelley, J. et al. Epik: a software program for pKa prediction and protonation state generation for drug-like molecules. *J. Comput.-Aided Mol. Des.* **21**, 681-691 (2007).

4.5 Supporting information

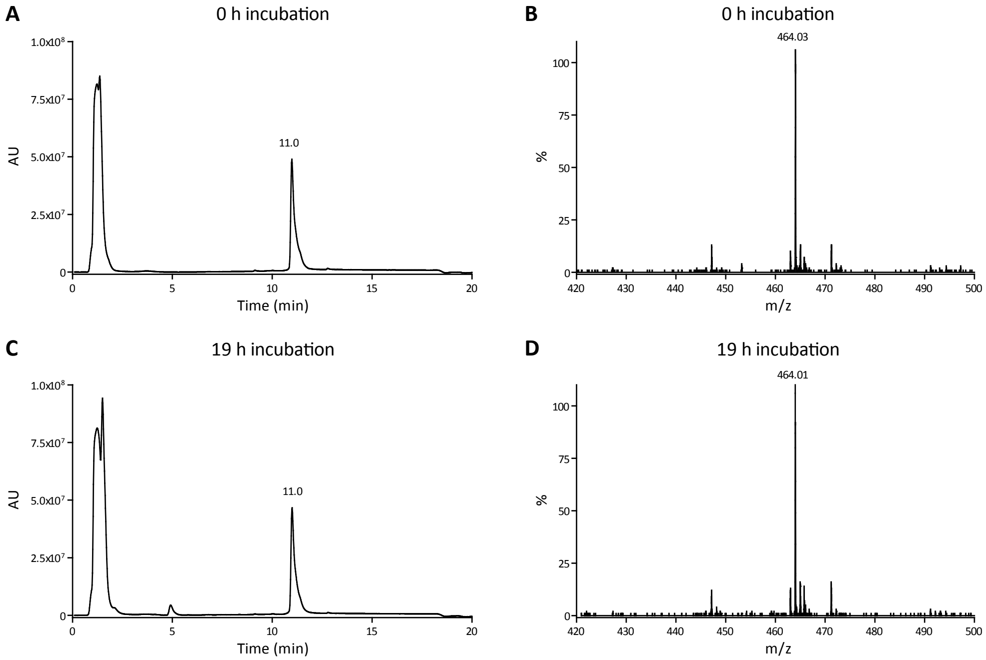

Supporting Figure S1. Michael acceptor study of inhibitor **1**. We incubated 100 µM of inhibitor **1** ((M+H$^+$) = 464.11) with 10 mM of *l*-glutathione (reduced) in a Tris-HCl buffer (50 mM, pH 7.4) at 310 K for 19 h. *L*-glutathione is a natural occurring reducing agent which is abundantly present in blood (1 mM) and can act as a Michael donor. After 19 h of incubation no Michael addition was observed (compare LC spectrum and MS profile in A] and B] with C] and D]).

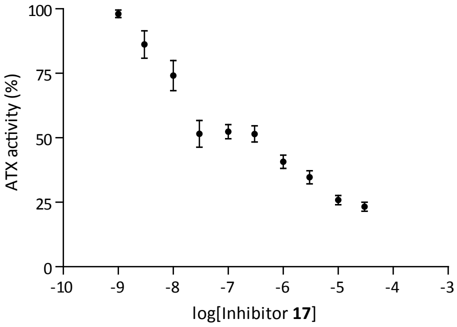

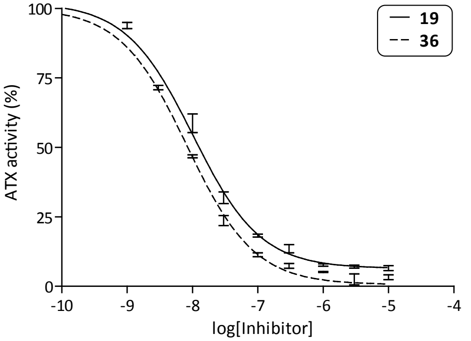

Supporting Figure S2. Dose-response graph for inhibitor **17** (n=5).

Supporting Figure S3. Dose-response curves for inhibitors **19** and **36**.

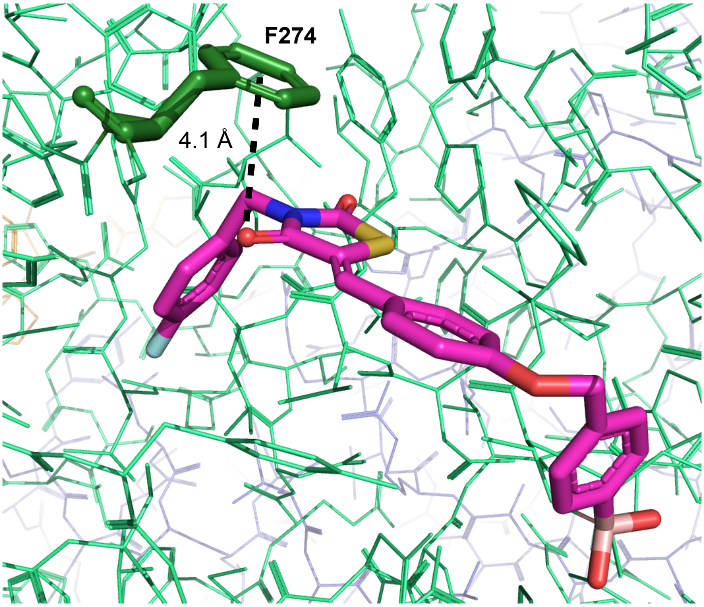

Supporting Figure S4. The distance between the oxygen of the carbonyl moiety in inhibitor **1** and the center of the aromatic ring of ATX residue F274 is 4.1 Å, suggesting π-stacking between these two moieties.

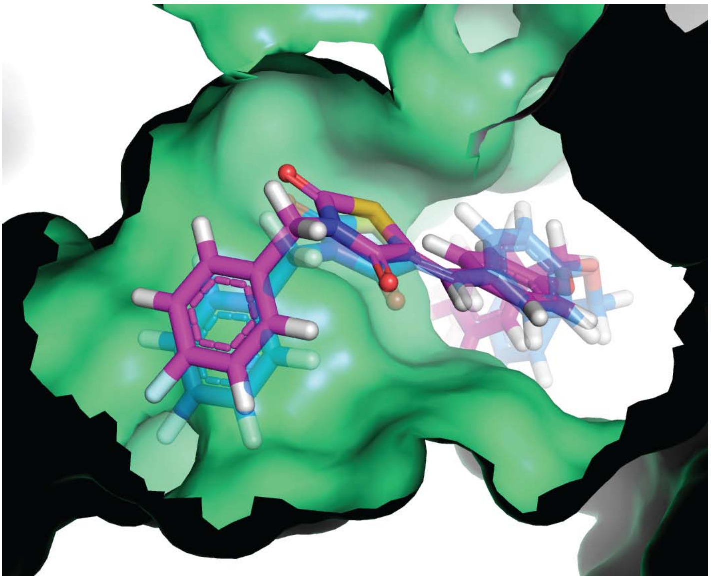

Supporting Figure S5. Docked (transparent blue) and X-ray (magenta) pose of inhibitor **1**.

Syntheses supporting information

Syntheses aldehydes 2-6

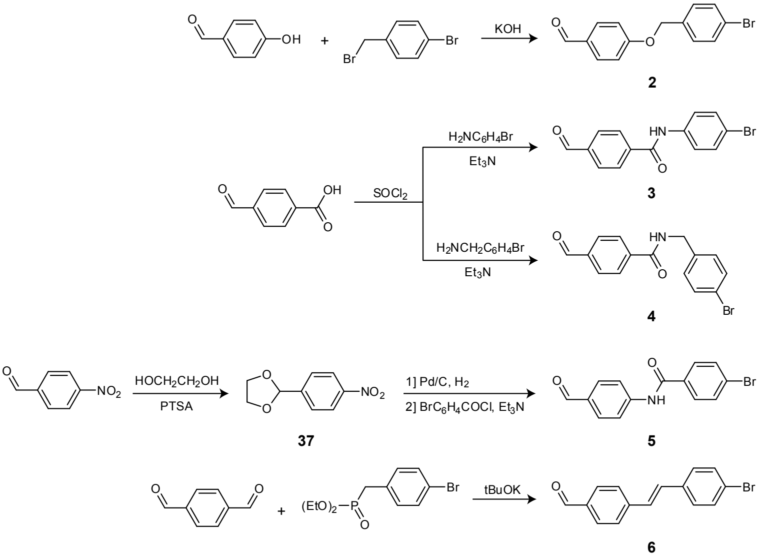

4-((4-bromobenzyl)oxy)benzaldehyde (2). To a solution of 4-hydroxybenzaldehyde (1.02 g, 8.33 mmol) and potassium hydroxide (0.533 g, 9.50 mmol) in dimethyl sulfoxide (13 mL), 4-(bromomethyl) phenyl bromide (1.38 g, 5.51 mmol) was added. The reaction mixture was stirred at room temperature and after 1 h the precipitate was isolated by centrifugation, washed with water (3x15 mL) and lyophilized resulting in the title compound. **Yield:** 1.5 g, 91% **^{1}H NMR:** δ = 9.87 (s, 1H), 7.87 (d, *J* = 8.8, 2H), 7.60 (d, *J* = 8.5, 2H), 7.43 (d, *J* = 8.5, 2H), 7.20 (d, *J* = 8.7, 2H), 5.22 (s, 2H). **^{13}C NMR:** δ = 191.23, 163.02, 135.77 ($\underline{C}_{Ar}$-Br+$\underline{C}_{Ar}$COH), 131.74, 131.40, 129.89, 121.16, 115.27, 68.79. **MS:** m/z [M+H]$^+$ calc. 291.00, 293.00, obs. 291.01, 293.02.

***N*-(4-bromophenyl)-4-formylbenzamide (3).** Thionyl chloride (0.75 mL, 10.3 mmol) was added to a suspension of 4-carboxy benzaldehyde (0.517 g, 3.44 mmol) in dry toluene (15 mL). The reaction mixture became clear after 4 h of refluxing. Concentrating the solution resulted in a light brown solid. The crude product was dissolved in dichloromethane (12.5 mL) and 4-bromo aniline (0.607 g, 3.53 mmol) and triethylamine (1.3 mL, 9.3 mmol) were added. After 1 h 30 of refluxing under an atmosphere of argon the reaction mixture was diluted with ethyl acetate (40 mL) and washed with 1 M hydrochloric acid (40 mL) and saturated bicarbonate solution (40 mL). The organic layer was dried over magnesium sulfate and was concentrated resulting in a yellow solid. **Yield:** 707.1 mg, 68%. **^{1}H NMR:** δ = 10.58 (s, 1H), 10.12 (s, 1H), 8.13 (d, *J* = 8.5, 2H), 8.06 (d, *J* = 8.5, 2H), 7.77 (d, *J* = 8.9, 2H), 7.56 (d, *J* = 8.9, 2H). **^{13}C NMR:** δ = 192.89, 164.81, 139.64, 138.26, 138.04, 131.49, 129.42, 128.43, 122.28, 115.69. **MS:** m/z [M+H]$^+$ calc. 304.00, 306.00, obs. 303.96, 305.96.

***N*-(4-bromobenzyl)-4-formylbenzamide (4).** In a dry flask, thionyl chloride (3.3 mL, 45.2 mmol) was added to a suspension of 4-carboxy benzaldehyde (1.07 g, 7.13 mmol) in dry toluene (30 mL). The reaction mixture was refluxed for 5 h and concentrated *in vacuo*. The crude product was dissolved in dichloromethane (25 mL) and 4-bromobenzyl amine (1.0 mL, 7.92 mmol) and triethylamine (1.3 mL, 7.17 mmol) were added. The reaction mixture was refluxed for 2 h. Finally, the mixture was diluted with ethyl acetate (60 mL) and washed with 1 M hydrochloric acid (40 mL) and bicarbonate solution (40 mL). The organic layer was dried over magnesium sulfate and concentrated *in vacuo*. **Yield:** 1.65 g, 73%. **^{1}H NMR:** δ = 10.08 (s, 1H), 9.30 (t, *J* = 5.9, 1H), 8.08 (d, *J* = 8.3, 2H), 8.00 (d, *J* = 8.5, 2H), 7.52 (d, *J* = 8.5, 2H), 7.30 (d, *J* = 8.5, 2H), 4.47 (d, *J* = 5.9, 2H). **^{13}C NMR:** δ = 192.85, 165.45, 139.15, 138.79, 137.84, 131.15, 129.53, 128.81, 127.98, 119.82, 42.19. **MS:** m/z $[M+H]^+$ calc. 318.01, 320.01, obs. 317.95, 319.96.

2-(4-nitrophenyl)-1,3-dioxolane (37). To a solution of 4-nitrobenzaldehyde (3.95 g, 26.1 mmol) in dry toluene (10 mL), molecular sieves (4 Å, 2 g), dry ethylene glycol (10.0 mL, 179 mmol) and *p*-toluenesulfonic acid monohydrate (2.04 g, 10.7 mmol) were added was refluxed for 25 h using a Dean-Stark apparatus. Toluene (50 mL) and water (50 mL) were added and the water layer was extracted with toluene (2x50 mL). The organic layers were combined and washed with brine (3x100 mL), dried over magnesium sulfate and finally concentrating *in vacuo*. **Yield:** 3.87 g, 76%. **^{1}H NMR:** δ = 8.25 (d, *J* = 8.8, 2H), 7.71 (d, *J* = 8.5, 2H), 5.89 (s, 1H), 4.05-3.97 (m, 4H). **^{13}C NMR:** δ = 147.91, 145.20, 127.79, 123.45, 101.38, 65.02. MS: m/z $[M+H]^+$ calc. 196.06, obs. 196.06.

4-bromo-*N*-(4-formylphenyl)benzamide (5). Compound **37** (3.87 g, 19.8 mmol) was dissolved in degassed tetrahydrofuran (250 mL) and 10 wt% Pd/C (480 mg) was added. After stirring the reaction mixture for 16 h under a hydrogen atmosphere it was filtered over Hyflo Super Cel® medium and was concentrated. The crude product was used without any further purification and was dissolved in dry dichloromethane (75 mL) and 4-bromobenzoyl chloride (3.57 g, 16.3 mmol) was added. The solution was stirred for 2 h and triethylamine (0.4 mL, 2.87 mmol) was added. Additional triethyl amine (2.8 ml, 20 mmol) was added over 2 h with time intervals of 30 min. After stirring for another 1 h 30 the solution was diluted with ethyl acetate (200 mL) and washed with 1 M hydrochloric acid (100 mL) and brine (100 mL). The solution was dried over magnesium sulfate and concentrated *in vacuo*. Crude product (922 mg) was deprotected in dichloromethane (100 mL) using perchloric acid (50 mL). After stirring the mixture for 2 h it was diluted with ethyl acetate (100 mL) and neutralized with 30 wt% sodium hydroxide solution which initiated separation. The oranic layer was dried over magnesium sulfate and the solvent was concentrated *in vacuo* which resulted in an orange solid. **Yield:** 464.1 mg, 66%. **^{1}H NMR:** δ = 10.69 (s, 1H), 9.92 (s, 1H), 8.02 (d, *J* = 8.3, 2H), 7.93 (d, *J* = 8.5, 2H), 7.90 (d, *J* = 8.5, 2H), 7.77 (d, *J* = 8.5, 2H). **^{13}C NMR:** δ = 191.62, 165.13, 144.61, 133.55, 131.68, 131.46, 130.59, 129.94, 125.74, 119.92. **MS:** m/z $[M+H]^+$ calc. 304.00, 306.00, obs. 304.03, 306.04.

(*E*)-4-(4-bromostyryl)benzaldehyde (6). To a solution of terephthalaldehyde (8.06 g, 60.1 mmol) in tetrahydrofuran (420 mL) were added diethyl(4-bromobenzyl)phosphonate (5.10 g, 16.6 mmol) and potassium tert-butoxide (2.92 g, 26.0 mmol). After 40 min stirring under an argon atmosphere additional potassium tert-butoxide (2.92 g, 26.0 mmol) was added and stirred for another 30 min. The reaction mixture was filtered and concentrated *in vacuo* and the resulting solid was purified using column chromatography (hexane-dichloromethane, 1:1) to provide the title compound. **Yield:** 2.1 g, 43%. **^{1}H NMR** ($CDCl_3$): δ = 9.98 (s, 1H), 7.86 (d, *J* = 8.4, 2H), 7.63 (d, *J* = 8.3, 2H), 7.50 (d, *J* = 8.6, 2H), 7.39 (d, *J* = 8.5, 2H), 7.14 (dd, *J* = 16.4, 23.2, 2H). **^{13}C NMR** ($CDCl_3$): δ = 191.75, 143.23, 135.78, 135.74, 132.22, 131.10, 130.49, 128.55, 128.28, 127.20, 122.60. **MS:** m/z $[M+H]^+$ calc. 287.01, 289.01, obs. 286.97, 288.97.

Synthesis amine linker-based inhibitor 36

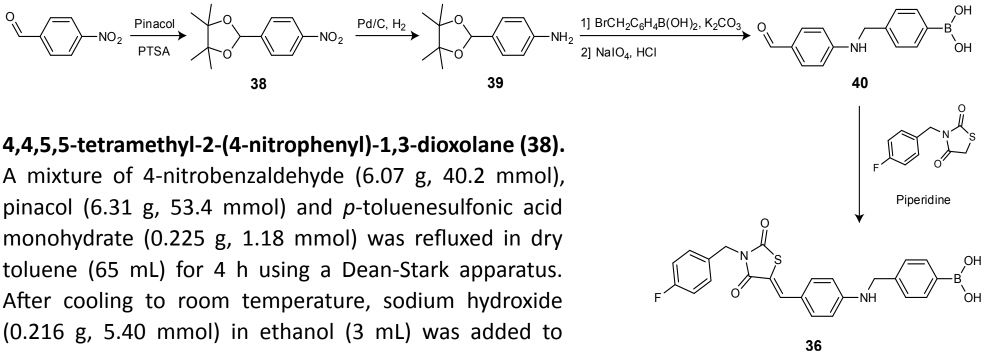

4,4,5,5-tetramethyl-2-(4-nitrophenyl)-1,3-dioxolane (38). A mixture of 4-nitrobenzaldehyde (6.07 g, 40.2 mmol), pinacol (6.31 g, 53.4 mmol) and *p*-toluenesulfonic acid monohydrate (0.225 g, 1.18 mmol) was refluxed in dry toluene (65 mL) for 4 h using a Dean-Stark apparatus. After cooling to room temperature, sodium hydroxide (0.216 g, 5.40 mmol) in ethanol (3 mL) was added to the mixture and stirred for 30 min. The suspension was filtered and the residue was washed with toluene (125 mL). The filtrate was washed with brine (3x100 mL), dried over sodium sulfate and finally concentrated *in vacuo* to provide the title compound. **Yield:** 9.3 g, 92%. **^{1}H NMR:** δ = 8.23 (d, *J* = 8.8, 2H), 7.70 (d, *J* = 8.4, 2H), 6.00 (s, 0H), 1.27 (s, 6H), 1.17 (s, 6H). **^{13}C NMR:** δ = 147.54, 147.04, 127.37, 123.40, 97.76, 82.75, 23.84, 21.89. **MS:** m/z $[M+H]^+$ calc. 252.12, obs. 252.11.

4-(4,4,5,5-tetramethyl-1,3-dioxolan-2-yl)aniline (39). A mixture of compound 38 (0.498 g, 1.98 mmol) and 10 wt% Pd/C (50 mg) in degassed tetrahydrofuran (15 mL) under a hydrogen atmosphere was stirred for 7 h. The mixture was filtrated over Hyflo Super Cel® medium and the filtrate was concentrated *in vacuo*. **Yield:** 438 mg, 100%. **^{1}H NMR:** δ = 7.06 (d, *J* = 8.4, 2H), 6.51 (d, *J* = 8.5, 2H), 5.71 (s, 1H), 5.10 (s, 2H), 1.21 (s, 6H), 1.19 (s, 6H). **^{13}C NMR:** δ =149.04, 127.44, 126.39, 113.12, 99.75, 81.47, 24.34, 22.00. **MS:** m/z $[M+H]^+$ calc. 222.15, obs. 222.14.

(4-(((4-formylphenyl)amino)methyl)phenyl)boronic acid (40). To a solution of amine 39 (1.06 g, 4.79 mmol) in dry dimethylformamide (10 mL), potassium carbonate (0.612 g, 4.43 mmol) and 4-bromomethylphenylboronic acid (0.880 g, 4.10 mmol) were added. After stirring overnight under an argon atmosphere the reaction mixture was diluted with ethyl acetate (100 mL). The mixture was washed with 0.1 M hydrochloric acid (3x50 mL), dried over magnesium sulfate and concentrated *in vacuo*. The resulting mixture of mono- and dialkylated products was purified using column chromatography (dichloromethane-methanol, 95:5) to isolate the monoalkylated intermediate (0.661 g, 45%).

The pinacol protecting group was removed as follows: To a solution of monoalkylated intermediate (0.140 g, 0.394 mmol) in tetrahydrofuran (3 mL), sodium periodate (0.107 g, 0.500 mmol) and water (0.424 mL) were added. After 30 min of stirring under an atmosphere of argon, 1 M hydrochloric acid (0.284 mL) was added and stirred for one night. The reaction mixture was diluted with ethyl acetate (13 mL) and washed with brine (11 mL). The water layer was extracted with ethyl acetate and the combined organic layers were washed with brine (8 mL), dried over magnesium sulfate and concentrated *in vacuo* to afford the title compound in quantitative yield. **Overall yield:** 100 mg, 45% (two steps). **^{1}H NMR:** δ = 9.58 (s, 1H), 7.97 (s, 2H), 7.74 (d, *J* = 8.1, 2H), 7.58 (d, *J* = 8.8, 2H), 7.42 (t, *J* = 6.0, 1H), 7.30 (d, *J* = 8.0, 2H), 6.67 (d, *J* = 8.7, 2H), 4.39 (d, *J* = 6.0, 2H), . **^{13}C NMR:** δ = 189.55, 153.95, 140.88, 134.23, 131.77, 126.15, 125.05, 111.59, 45.79 (C-B$(OH)_2$ not visible). **MS:** m/z $[M+H]^+$ calc. 256.11, obs. 256.17.

(*Z*)-(4-(((4-((3-(4-fluorobenzyl)-2,4-dioxothiazolidin-5-ylidene)methyl)phenyl)amino)methyl)phenyl) boronic acid (36). To a solution of 3-(4-fluorobenzyl)thiazolidine-2,4-dione (18.8 mg, 0.0835 mmol) in ethanol (0.2 mL), piperidine (8.2 μL, 0.0835 mmol) and aldehyde 40 (19.7 mg, 0.0772 mmol) were added and the solution was refluxed for 4 h. Upon cooling to room temperature the product precipitated out of solution. Pure compound was obtained after preparative HPLC purification. **Yield:** 10 mg, 29%. **^{1}H NMR:** δ = 7.99 (s, 2H), 7.76 (s, 1H), 7.74 (d, *J* = 8.1, 2H), 7.47 – 7.23 (m, 7H), 7.20 – 7.14 (m, 2H), 6.70 (d, *J* = 8.8, 2H), 4.79 (s, 2H), 4.37 (d, *J* = 5.8, 2H). **^{13}C NMR:** δ = 167.54, 165.66, 161.59 (d, $^1J_{CF}$ = 244), 151.27, 141.03, 134.76, 134.24, 132.67, 132.01 (d, $^4J_{CF}$ = 3), 129.84 (d, $^3J_{CF}$ = 8), 126.17, 119.94, 115.40 (d, $^2J_{CF}$ = 21), 112.57, 112.37, 45.84, 43.66 (C-B$(OH)_2$ not visible). **MS:** m/z $[M+H]^+$ calc. 463.13, obs. 463.20.

CHAPTER 5

From the phosphodiesterase autotaxin to dual specificity phosphatases:

A short introduction on dual specificity phosphatases

5.1 Introduction

The previous chapters describe the discovery, optimization and biological validation of autotaxin (ATX) inhibitors. Next to the phosphodiesterase ATX, protein phosphatases are another interesting class of enzymes in drug discovery.[1] Like ATX, protein phosphatases have the ability to hydrolyze phosphate esters, however, their substrates are intracellular phosphorylated proteins rather than lipids. Therefore, ATX and protein phosphatases have different functions in biology. Here a short introduction on protein phosphatases is provided with the main focus on dual specificity phosphatases as an introduction to the next chapter.

After protein synthesis, approximately one-third of mammalian proteins are phosphorylated by protein kinases (Figure 1).[2] Dynamic protein phosphorylation is one of the major mechanisms by which cells regulate transcription, signal transduction, proliferation, differentiation, motility and metabolism.[3-8] The phosphorylation state of cellular proteins is tightly controlled by the concerted and reversible action of protein kinases and protein phosphatases. The importance of controlling the activity of protein kinases in biology has long been recognized and this has resulted in the development of several clinically approved protein kinase inhibitors (e.g. Imatinib). A growing body of evidence now demonstrates that the regulation of protein dephosphorylation by protein phosphatases is equally important, which stimulates the development of protein phosphatase inhibitors.[4]

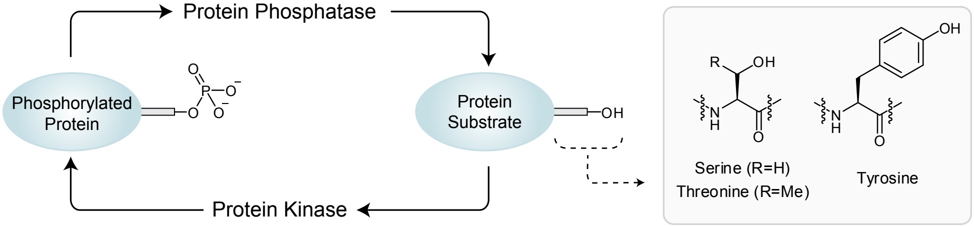

Figure 1: The phosphorylation status of proteins is regulated by both protein phosphatases and protein kinases. Protein phosphorylation occurs predominately on the amino acids serine, threonine and tyrosine.

Protein phosphatases have historically have classified as serine/threonine (PSP),[9] tyrosine (PTP),[10] and dual specificity (DUSP)[11] phosphatases based on their preference for specific phosphorylated hydroxyl amino acids (Figure 1) over others. The unique feature that distinguishes DUSPs from PSPs and PTPs is their ability to dephosphorylate both phosphorylated tyrosine and serine/threonine residues within a protein substrate. Both classical PTPs and DUSPs share a similar mechanism of catalysis for the hydrolysis of phosphorylated substrates that involves the formation of a phosphoryl-enzyme intermediate (Figure 2).[11-13] The highly conserved catalytic domain in DUSPs contains the consensus sequence HCXXGXXRS(T) (Table 1). The cysteine residue (C), which is essential for catalytic

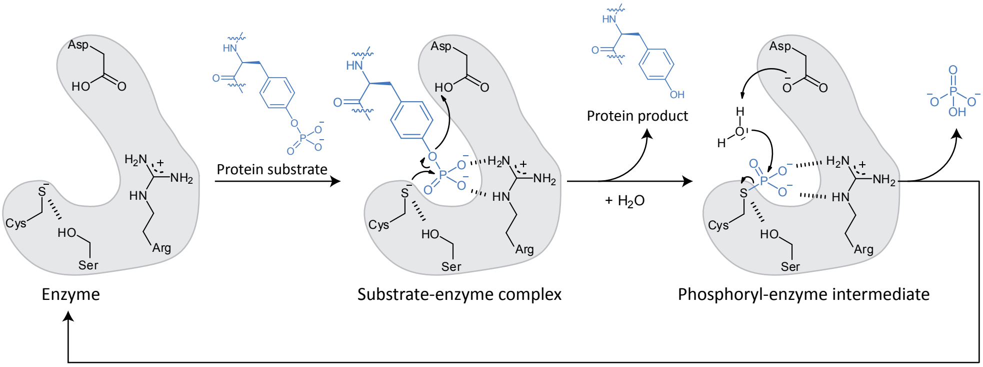

Figure 2: Proposed catalytic mechanism for DUSPs and classical PTPs.

activity, is positioned at the centre of the catalytic pocket.[11] The arginine (R) of the consensus sequence coordinates to the phosphate group of the protein substrate to assist with catalysis. There is also a conserved aspartic acid present upstream of this conserved motif that acts as a general acid/base catalyst. The serine (S) of the consensus sequence, threonine (T) in some other protein phosphatases (i.e. DUSP23), most likely plays a role in stabilizing the cysteinyl anion through hydrogen bonding.[14-16] The catalytic pocket of a DUSP is shallow, but broader than that of classical PTPs, which is thought to be the mechanism how DUSPs can simultaneously accommodate more than one phosphorylated residue.[13]

Table 1: Conserved Catalytic Domain for DUSPs and PTPs.

DUSP3	H	C	R	E	G	Y	S	R	S
DUSP13	H	C	A	M	G	V	S	R	S
DUSP2	H	C	Q	A	G	I	S	R	S
DUSP4	H	C	Q	A	G	I	S	R	S
DUSP5	H	C	E	A	G	I	S	R	S
DUSP26	H	C	A	V	G	V	S	R	S
DUSP1	H	C	Q	A	G	I	S	R	S
DUSP27	H	C	V	M	G	R	S	R	S
DUSP22	H	C	L	A	G	V	S	R	S
DUSP14	H	C	A	A	G	V	S	R	S
DUSP12	H	C	H	A	G	V	S	R	S
DUSP16	H	C	L	A	G	I	S	R	S
DUSP10	H	C	Q	A	G	V	S	R	S
DUSP5	H	C	Q	A	G	V	S	R	S
PTPMT1	H	C	K	A	G	R	S	R	S
SSH3	H	C	K	M	G	V	S	R	S
DUSP15	H	C	F	A	G	I	S	R	S
DUSP6	H	C	L	A	G	I	S	R	S
DUSP7	H	C	L	A	G	I	S	R	S
DUSP13	H	C	V	V	G	V	S	R	S

[a] Table displays the PTP signature sequence in DUSP3, a well studied DUSP, compared with the 20 closest human homologs. Conserved amino acids are depicted in blue. Serine (S) is partially conserved (purple).

Although a number of potent and selective inhibitors of PSPs isolated from natural sources are known, like tautomycin and fostriecin,[17] selective PTP or DUSP inhibitors are still rare.[18] Genetic approaches using small interfering RNA (siRNA) can provide some insight into the biological function of these protein phosphatases in cells. However, some PTPs and DUSPs interact with other proteins and regulate their function in a manner that is independent of their phosphatase activity.[19] In addition, wrong gene annotations in commercial siRNA libraries and the difficulty of reproducible transfections of siRNA ask for independent controls. Therefore, potent and selective small molecule inhibitors of protein phosphatases are valuable to study the function of protein phosphatases, allowing immediate and reversible inhibition. The discovery of small molecule inhibitors of protein phosphatases has been challenging, especially the search for selective inhibitors. Selective inhibitors are difficult to obtain due to the highly conserved nature of the PTPs and DUSPs active site (Table 1).

In the next chapter we study the involvement of protein phosphatases in *Salmonella typhimurium* infection of human cells and we describe the discovery and development of inhibitors that target protein phosphatases that are essential for this infection process.

5.2 References

1. Blaskovich, M. Drug Discovery and Protein Tyrosine Phosphatases. *Curr. Med. Chem.* **16**, 2095-2176 (2009).
2. Zolnierowicz, S. & Bollen, M. Protein phosphorylation and protein phosphatases De Panne, Belgium, September 19-24, 1999. *EMBO J.* **19**, 483-488 (2000).
3. Hunter, T. Protein kinases and phosphatases: The Yin and Yang of protein phosphorylation and signaling. *Cell* **80**, 225-236 (1995).
4. Tonks, N. & Neel, B. Combinatorial control of the specificity of protein tyrosine phosphatases. *Curr. Opin. Cell Biol.* **13**, 182-195 (2001).
5. Alonso, A. et al. Protein Tyrosine Phosphatases in the Human Genome. *Cell* **117**, 699-711 (2004).
6. Mustelin, T. Moorhead, G. (ed.), pp. 9-22 (Humana Press, 2007).
7. Pearson, G. et al. Mitogen-Activated Protein (MAP) Kinase Pathways: Regulation and Physiological Functions. *Endocr. Rev.* **22**, 153-183 (2001).
8. Stoker, A. Protein tyrosine phosphatases and signalling. *J. Endocrinol.* **185**, 19-33 (2005).
9. Mumby, M. C. & Walter, G. Protein serine/threonine phosphatases: structure, regulation, and functions in cell growth. *Physiol. Rev.* **73**, 673-699 (1993).
10. Zhang, Z. Protein Tyrosine Phosphatases: Structure and Function, Substrate Specificity, and Inhibitor Development. *Annu. Rev. Pharmacol. Toxicol.* **42**, 209-234 (2002).
11. Patterson, K. Brummer, T. O'Brien, P. & Daly, R. Dual-specificity phosphatases: critical regulators with diverse cellular targets. *Biochem. J.* **418**, 475-489 (2009).
12. Denu, J. & Dixon, J. Protein tyrosine phosphatases: mechanisms of catalysis and regulation. *Curr. Opin. Chem. Biol.* **2**, 633-641 (1998).
13. Denu, J. M. & Dixon, J. E. A catalytic mechanism for the dual-specific phosphatases. *Proc. Natl. Acad. Sci. USA* **92**, 5910-5914 (1995).
14. Agarwal, R. Burley, S. & Swaminathan, S. Structure of Human Dual Specificity Protein Phosphatase 23, VHZ, Enzyme-Substrate/Product Complex. *J. Biol. Chem.* **283**, 8946-8953 (2008).
15. Rossi, R. et al. Fast-reacting Thiols in Rat Hemoglobins Can Intercept Damaging Species in Erythrocytes More Efficiently Than Glutathione. *J. Biol. Chem.* **273**, 19198-19206 (1998).
16. Stuckey, J. et al. Crystal structure of Yersinia protein tyrosine phosphatase at 2.5 Å and the complex with tungstate. *Nature* **370**, 571-575 (1994).
17. Colby, D. & Chamberlin, A. R. Pharmacophore Identification: The Case of the Ser/Thr Protein Phosphatase Inhibitors. *Mini-Rev. Med. Chem.* **6**, 657-665 (2006).

18. Bialy, L. & Waldmann, H. Inhibitors of Protein Tyrosine Phosphatases: Next-Generation Drugs? *Angew. Chem., Int. Ed.* **44**, 3814-3839 (2005).
19. Zou, X. et al. The Cell Cycle-Regulatory CDC25A Phosphatase Inhibits Apoptosis Signal-Regulating Kinase 1. *Mol. Cell. Biol.* **21**, 4818-4828 (2001).

CHAPTER 6

Controlling bacterial infection by human dual specificity phosphatase inhibition

Harald M.H.G. Albers, Coenraad Kuijl, Tiziana Scanu, Loes J.D. Hendrickx, Sharida Wekker, Nadha Farhou, Nora Liu, Patrick Celie, Huib Ovaa and Jacques J. Neefjes, *Paper in preparation*.

Abstract. Multidrug resistance (MDR) of bacteria is a serious social threat and a neglected area in the pharmaceutical industry. New intervention strategies besides conventional treatments are required to overcome MDR bacteria. Current treatments use antibiotics that target the pathogen but not the involved host protein pathway required for pathogen survival. Recently, it has been demonstrated by Kuijl *et al.* that H-89 inhibits intracellular growth of *Salmonella (S.) typhimurium* by inhibiting the host's protein kinase PKB/Akt1. Here we describe an RNA interference screen of the human phosphatome that reveals several host dual specificity phosphatases (DUSP3, 11 and 27) that are essential for intracellular growth of *S. typhimurium*. In parallel, screening a tyrosine/dual specificity phosphatase targeted library of small molecules afforded inhibitors that reduced intracellular growth of *S. typhimurium*. One of these identified molecules inhibited the host proteins DUSP3, 11 and 27 confirming the target (DUSPs) lead (inhibitor) relationship for *S. typhimurium* infection. This inhibitor was further developed into a selective inhibitor for DUSP3 (IC_{50} = 0.33 µM) over DUSP27 (IC_{50} > 5 µM) and molecular docking reveals a binding pose of this inhibitor for DUSP3 explaining this selectivity. In conclusion, targeting the host proteins required for pathogen survival appears to be a valid way to control bacterial infection and holds promise as a new therapeutic approach to treat bacterial infections in the clinic.

6.1 Introduction

Bacterial infection is still a big social threat as proven by one of the world's most severe outbreaks of Enterohaemorrhagic *Escherichia coli* (EHEC) in Europe last year.[1] In addition, with multidrug resistance (MDR) of bacteria it becomes increasingly difficult to treat these bacterial infections.[2] New intervention strategies are required next to conventional treatments to overcome MDR in bacteria. Developing medicines that target host proteins essential for bacterial survival instead of killing bacteria directly with antibiotics could be an answer to this problem.

Many bacterial pathogens survive in intracellular compartments of host cells and use that location as a niche for growth while remaining undetected by the immune system.[3] These bacteria frequently remain in such compartments in a dormant state and are therefore difficult to reach by antibodies and antibiotics. For their survival, bacteria need to manipulate the host system to prevent transport from phagosomes to phagolysosomes where they can be degraded.[4,5]

Using a combination of chemistry, small interfering RNA (siRNA) screening, biochemistry and cell biology, we have recently shown that the intracellular bacteria *Salmonella* (*S.*) *typhimurium* activates a signaling network around the protein kinase PKB/Akt1 to prevent delivery to lysosomal compartments where bacteria would otherwise have been degraded (Figure 1A).[5] Bacteria activate the protein kinase PKB/Akt1 for their survival

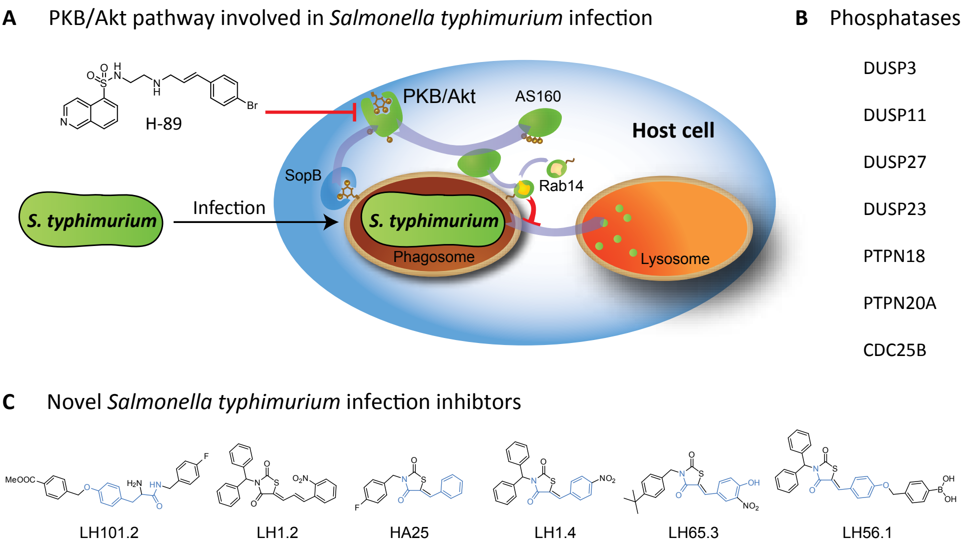
A
PKB/Akt pathway involved in *Salmonella typhimurium* infection
H-89
Br
N
S. typhimurium
Infection
SopB
PKB/Akt
AS160
Host cell
Rab14
S. typhimurium
Phagosome
Lysosome
B
Phosphatases
DUSP3
DUSP11
DUSP27
DUSP23
PTPN18
PTPN20A
CDC25B
C
Novel *Salmonella typhimurium* infection inhibtors
MeOOC
H₂N
HN
F
O₂N
NO₂
OH
LH101.2
LH1.2
HA25
LH1.4
LH65.3
LH56.1

Figure 1: (A) The PKB/Akt1 protein pathway involved in *Salmonella (S.) typhimurium* infection. By inhibiting PKB/Akt1 using small molecule inhibitor H-89, intracellular growth of *S. typhimurium* can be blocked. (B) Identified phosphatases by siRNA screening that reduce intracellular growth of *S. typhimurium* in human cells. (C) Novel identified *S. typhimurium* infection inhibitors by screening a tyrosine-based small molecule library (blue: tyrosine motif).

and we inhibited this protein kinase with a commercial inhibitor (H-89, Figure 1A) which induced the bacterial elimination in human cells.[5]

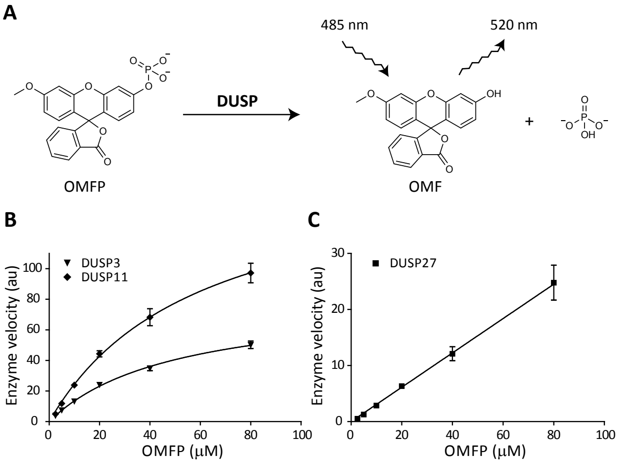

Figure 2: (A) DUSP activity assay using OMFP as substrate. (B) Saturation curves for DUSP3 and 11. (C) Linear relationship of the phosphate hydrolysis velocity of DUSP27 and substrate concentration.

We now report the identification of protein phosphatases that control intracellular growth of *S. typhimurium* in the human host cell. The function of only few protein phosphatases is known and this class of enzymes is studied relatively poorly compared to protein kinases. Protein phosphatases are divided in three main classes based on their phosphorylated protein substrates; serine/threonine phosphatases, tyrosine phosphatases and dual specificity phosphatases (DUSP).[6] The latter class is able to hydrolyze both phosphorylated serine, threonine and tyrosine residues and is member of the protein tyrosine phosphatase family. By silencing all protein phosphatases (Supporting Table S1) of the human host cell we have mainly identified protein tyrosine phosphatases, which control intracellular bacterial growth of *S. typhimurium* (Figure 1B). Among these identified protein tyrosine phosphatases several DUSPs were present (DUSP3, 11 and 27).

We tested a tyrosine-based small molecule library designed to target protein tyrosine phosphatases, including DUSPs. This library partly consisted of the previously described ATX inhibitors in Chapter 3. Compounds depicted in Figure 1C reduced the intracellular growth of *S. typhimurium* in host cells to a similar extent as obtained through phosphatase silencing. Important to note, these compounds were not toxic for *S. typhimurium* or the host cell alone (see Supporting Figures S1 and S2).

In this study we show that one of the identified inhibitors of intracellular growth of *S. typhimurium* act on the identified host DUSPs. Medicinal chemistry efforts then resulted in a selective DUSP3 inhibitor, which is a challenging task in the development of phosphatase inhibitors. The selectivity of this compound can be explained by molecular docking of this inhibitor into DUSP3 and 27 crystal structures.

6.2 Enzyme kinetics of DUSP3, 11 and 27

In order to test *S. typhimurium* inhibitors on DUSP activity we have developed an activity assay using 3-*O*-methylfluorescein phosphate (OMFP) as DUSP substrate (Figure 2A).[7] The quenched

OMFP substrate is hydrolyzed by the DUSPs into the fluorophore 3-*O*-methylfluorescein (OMF) and phosphate. First we studied the enzyme kinetics of DUSP3, 11 and 27 (Figure 2B and C) using this assay. DUSP3 and 11 show normal Michaelis–Menten kinetics giving saturation at high substrate concentration (Figure 2B) while DUSP27 shows a linear relationship between enzyme velocity and substrate concentration (Figure 2C). The Michaelis constants (K_m values) for DUSP3 and 11 are 50 µM and 59 µM, respectively. Due to the linear kinetics of DUSP27 its K_m is infinite under these conditions.

6.3 Effect of *S. typhimurium* inhibitors on DUSP activity

The compounds that reduced intracellular growth of *S. typhimurium* in human host cells have been tested on their effect on the the activity of the three DUSPs. DUSP activity was measured at an OMFP concentration of 20 µM using an inhibitor concentration of 5 µM (Figure 3). The most active compound that inhibited all the three DUSPs is LH65.3 with high percentage inhibitions (PI) between 85% and 97%. This inhibitor did not show any preference for a specific DUSP (Figure 4A).

6.4 Structure-activity relationships of DUSP inhibitors

In order to increase the potency and selectivity of LH65.3 for the three DUSPs we synthesized analogs of this inhibitor. For this purpose we changed the benzyl (R1) and benzylidene (R2) moieties as depicted in Table 1. Activities of the compounds for DUSP3, 11 and 27 were measured as percentage inhibition (PI) at an inhibitor concentration of 5 µM. First we replaced the 4-*tert*-butyl benzyl (R1) moiety in LH65.3 by 4-nitroacetophenone (**1**), 4-trifluoromethyl benzyl (**2**), diphenyl methane (**3**), 2-(methyl)naphthalene (**4**), 4-bromo benzyl (**5**) and 4-fluoro benzyl (**6**). None of the modifications improved the activity of the inhibitors (Table 1). Next, we changed the position of the nitro and hydroxyl moiety in LH65.3 (compounds **7** and **14**) which had a negative effect on DUSP inhibition. However, introduction of a methoxy group on the *meta* position (**21**) afforded full inhibition for all the three DUSPs. We then explored structure-activity relationships (SAR) of all the possible combinations of the previously described R1 and R2 groups (Table 1). In general, having a 4-hydroxy-3-methoxy-5-nitrophenyl moiety for R1 (**21**-**26**) has a positive effect on the potency of the inhibitors leading to almost full inhibition for the three DUSPs. The nature of the R1 group doesn't seem to have a

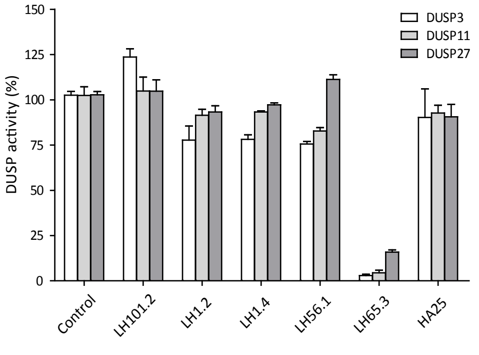

Figure 3: Effect of identified *S. typhimurium* infection inhibitors on the activity of DUSP3, 11 and 27. DUSP activity (%) has been measured at an inhibitor concentration of 5 µM.

Table 1: Structure-activity relationships of DUSP inhibitors. Percentage inhibition (PI, %) at 5 µM of compound are given for DUSP3, 11 and 27, respectively.

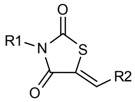

R2 **R1**	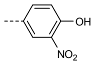	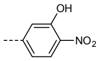	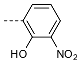	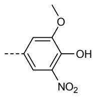
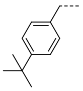	LH65.3 97 ± 1 🟩 **DUSP3** 96 ± 1 🟩 **DUSP11** 84 ± 1 ▨ **DUSP27**	**7** 49 ± 3 🟧 41 ± 4 🟧 22 ± 4 🟥	**14** 28 ± 7 🟥 26 ± 2 🟥 20 ± 4 🟥	**21** 98 ± 1 🟩 98 ± 1 🟩 94 ± 1 🟩
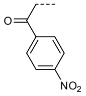	**1** 22 ± 1 🟥 14 ± 1 🟥 10 ± 3 🟥	**8** 98 ± 1 🟩 99 ± 1 🟩 40 ± 1 🟧	**15** 81 ± 6 ▨ 62 ± 7 ▨ 22 ± 2 🟥	**22** 99 ± 1 🟩 99 ± 1 🟩 92 ± 1 🟩
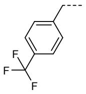	**2** 71 ± 12 ▨ 65 ± 6 ▨ 53 ± 3 🟧	**9** 89 ± 10 ▨ 80 ± 2 ▨ 34 ± 3 🟧	**16** 43 ± 2 🟧 35 ± 6 🟧 29 ± 3 🟥	**23** 99 ± 1 🟩 100 ± 1 🟩 99 ± 1 🟩
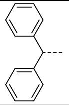	**3** 68 ± 4 ▨ 66 ± 6 ▨ 53 ± 2 🟧	**10** 70 ± 6 ▨ 53 ± 5 🟧 33 ± 6 🟧	**17** 70 ± 7 ▨ 69 ± 4 ▨ 56 ± 1 🟧	**24** 98 ± 1 🟩 99 ± 1 🟩 96 ± 1 🟩
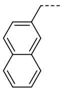	**4** 91 ± 1 🟩 85 ± 1 ▨ 68 ± 4 ▨	**11** 87 ± 3 ▨ 64 ± 5 ▨ 22 ± 3 🟥	**18** 66 ± 3 ▨ 57 ± 8 🟧 33 ± 3 🟧	**25** 96 ± 2 🟩 93 ± 2 🟩 84 ± 3 ▨
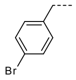	**5** 96 ± 1 🟩 86 ± 8 ▨ 47 ± 3 🟧	**12** 69 ± 3 ▨ 56 ± 2 🟧 25 ± 1 🟥	**19** 48 ± 4 🟧 49 ± 2 🟧 30 ± 2 🟧	**26** 96 ± 1 🟩 98 ± 1 🟩 95 ± 1 🟩
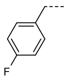	**6** 6 ± 2 🟥 6 ± 4 🟥 9 ± 1 🟥	**13** 42 ± 5 🟧 25 ± 1 🟥 13 ± 1 🟥	**20** 10 ± 1 🟥 8 ± 2 🟥 7 ± 4 🟥	**27** 10 ± 1 🟥 12 ± 10 🟥 15 ± 1 🟥

🟥 0-30% 🟧 30-60% ▨ 60-90% 🟩 90-100%

large negative effect on the activity of the compounds when R2 is 4-hydroxy-3-methoxy-5-nitrophenyl, with the only exception when R1 is 4-fluoro benzyl (**27**). Overall, poor activities were obtained for R1 as a 4-fluoro benzyl moiety (**6**, **13**, **20** and **27**), most of the activities (PI) for these compounds were below 15%.

6.5 Selectivity and mode of inhibition of inhibitor 8

For the most active compounds in Table 1 that evidenced full DUSP3 inhibition (dark green boxes) we have determined IC_{50} values for all the three DUSPs (Table 2) in order to find selective DUSP inhibitors. Obtained IC_{50} values for the inhibitors varied between 0.33 and 2.4 µM. We were able to improve the activity of our reference inhibitor,

Table 2: IC_{50} values (µM) for the ten most potent DUSP inhibitors sorted by decreasing potency for DUSP3.

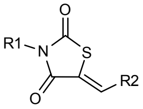

Entry	R1	R2	DUSP3	DUSP11	DUSP27
8	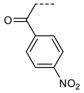	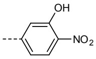	0.33 ± 0.06	0.73 ± 0.06	> 5.00
23	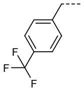	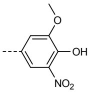	0.59 ± 0.08	0.66 ± 0.03	0.94 ± 0.06
25	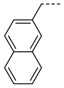	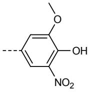	0.93 ± 0.09	1.01 ± 0.09	0.70 ± 0.01
24	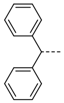	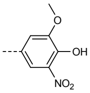	1.21 ± 0.20	1.23 ± 0.02	1.45 ± 0.06
4	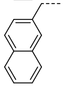	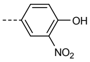	1.27 ± 0.25	1.67 ± 0.09	2.53 ± 0.23
21	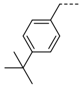	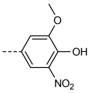	1.36 ± 0.05	1.35 ± 0.08	1.79 ± 0.03
26	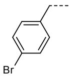	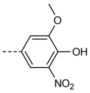	1.40 ± 0.02	1.35 ± 0.07	1.65 ± 0.02
LH65.3	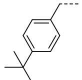	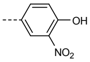	1.53 ± 0.05	1.57 ± 0.06	1.86 ± 0.05
5	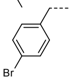	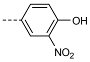	1.62 ± 0.08	2.11 ± 0.10	1.81 ± 0.04
22	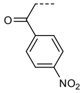	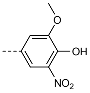	1.74 ± 0.27	2.11 ± 0.17	2.43 ± 0.03

LH65.3, by a 5 fold for DUSP3 resulting in inhibitor **8**. More importantly, inhibitor **8** is selective for DUSP3 (IC_{50} = 0.33 µM) compared to DUSP11 and 27 (IC_{50} = 0.73 µM and IC_{50} > 5 µM). In Figure 4A and 4B the dose-response curves for LH65.3 and **8** are depicted to visualize the gain in potency and selectivity of **8** for the three DUSPs compared to LH65.3.

Next, we studied the mode of inhibition of **8** using Lineweaver-Burk analysis. For DUSP3 and 11, inhibitor **8** showed non-competitive inhibition (Figure 4C). Increasing the inhibitor concentration of inhibitor **8** did not change the V_{max} or K_m of DUSP27 (Figure 4C).

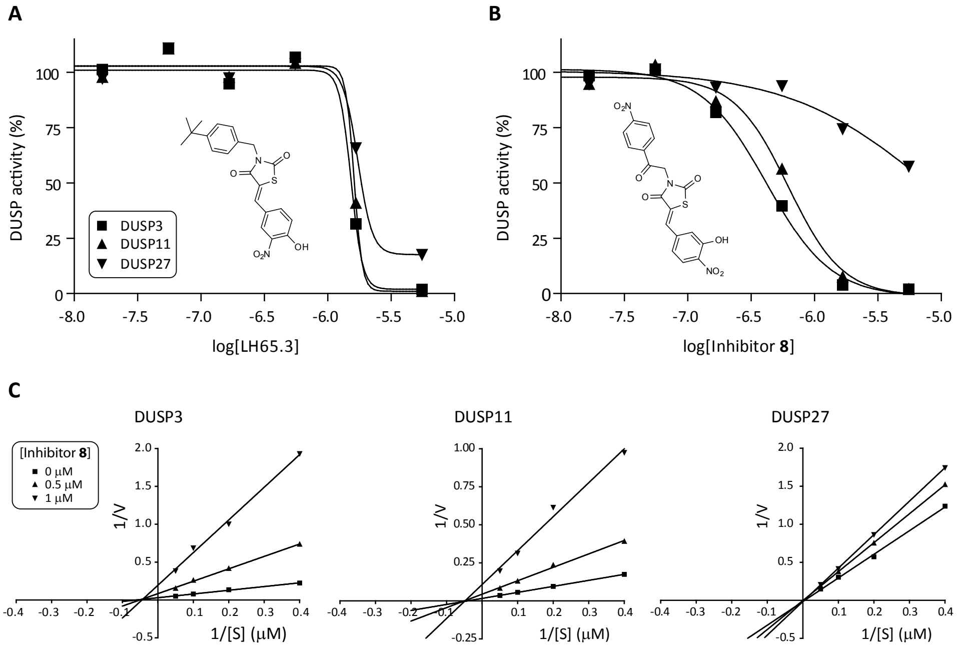

Figure 4: Selectivity and mode of inhibition. (A) Dose response curves for LH65.3. (B) Dose response curves for inhibitor **8**. (C) Lineweaver-Burk analysis of inhibitor **8** for DUSP3, 11 and 27.

6.6 Protein surface comparison between DUSP3 and 27

In order to explain the selectivity of inhibitor **8** for DUSP3 over DUSP27 we compared the protein surfaces of these two DUSPs. Several crystal structures of DUSP3 have been reported[8-10] but not for DUSP27 at the time of this study. Therefore we crystallized DUSP27 to make a structural comparison with DUSP3 (for details concerning the crystallization see Experimental section). In Figure 5 the electrostatic surfaces of DUSP3,[10] inactive DUSP3 (C124S mutant) bound to a phosphorylated p38 peptide,[8] and DUSP27 are displayed. In DUSP3 two pockets are clearly visible, the catalytic pocket (P1) and an arginine pocket (P2). The phosphorylated p38 peptide binds to these pockets with its phosphorylated tyrosine residue and phosphorylated serine residue to P1 and P2, respectively.[8] The P1 and P2 pocket in DUSP3 are separated by a cleft were the p38 peptide still can bind. In DUSP27 this catalytic pocket P1 is clearly visible but the P2 pocket is not as abundantly present as in DUSP3. A clear difference between DUSP3 and 27 can be observed in the electrostatic surface potential. DUSP3 and inactive DUSP3 have identical electrostatic surfaces while DUSP27 is displaying a reversed electrostatic surface compared to DUSP3. This reversed electrostatic surface between DUSP3 and 27 has been predicted using an DUSP27 homology model[11] and confirmed by a recently resolved DUSP27 structure[12] and our data.

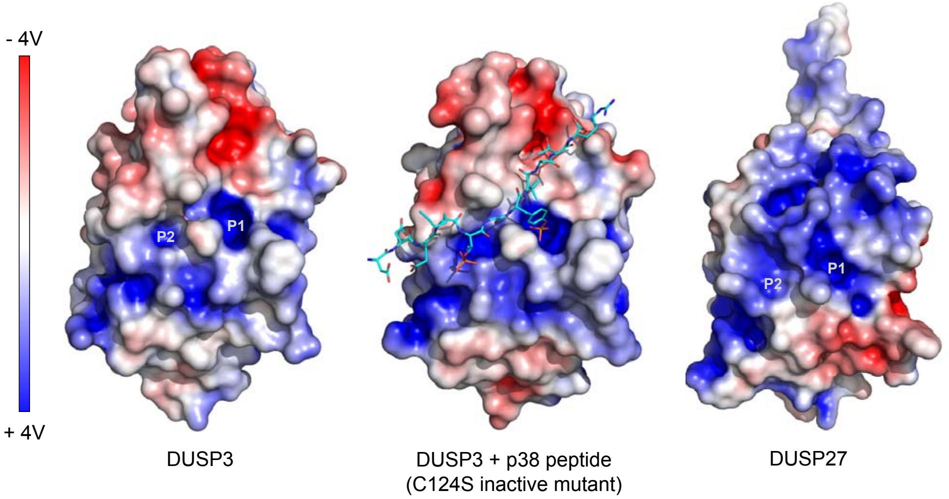

Figure 5: Surface representation displaying the electrostatic surface (blue is positive, red is negative) of the crystal structures of DUSP3 (PDB ID: 1VHR), inactive DUSP3 (C124S mutant) binding to a phosphorylated p38 peptide (PDB ID: 1J4X) and DUSP27. Catalytic site is indicated with P1 and an arginine pocket with P2.

6.7 Molecular docking of inhibitor 8 with DUSP3 and 27

Intrigued by the differences in the surfaces of DUSP3 and 27 we reasoned that molecular docking of inhibitor **8** with these two DUSPs could explain why this inhibitor is selective for DUSP3 over DUSP27. In our docking approach, using the program Autodock, we used a large docking site around catalytic pocket P1 and arginine pocket P2 (docking space, 30 Å x 30 Å x 30 Å) to see whether inhibitor **8** has a preference for a different binding site than P1 and P2. However, the best binding site of inhibitor **8** for DUSP3 and 27 was catalytic pocket P1 (Figure 6). The best docking pose of inhibitor **8** for DUSP3

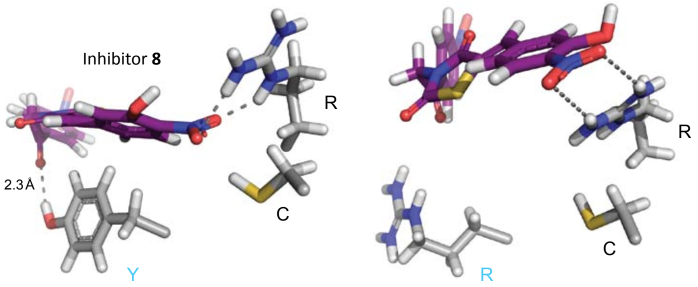

Protein:	DUSP3	DUSP27
Catalytic sequence:	HCREGYSR	HCVMGRSR
Docking energy:	- 8.0 kcal mol^{-1}	- 6.4 kcal mol^{-1}

Figure 6: Molecular docking suggests that inhibitor **8** (deep purple) binds in proximity of catalytic arginine residue (R) of DUSP3 and 27. A hydrogen bond is observed between a tyrosine residue (Y) in the DUSP3 active site with the indicated carbonyl of inhibitor **8**, this interaction is not possible in DUSP27.

revealed an interaction with the catalytic arginine residue R130 of DUSP3 with the nitro group in **8**. In addition, there is a hydrogen bond between the carbonyl of the 4-nitroacetophenone moiety in **8** with tyrosine residue Y128 (Figure 6). This hydrogen bond is not observed for the best docking pose of inhibitor **8** in DUSP27 because the tyrosine residue in not conserved in DUSP27 and is replaced by an arginine residue (Figure 6). This hydrogen bond of **8** with DUSP3 is a logical explanation why the affinity of **8** for DUSP3 (IC_{50} = 0.33 µM) is much higher than for DUSP27 (IC_{50} > 5 µM) and also for the higher predicted binding energy of inhibitor **8** for DUSP3 (-8.0 kcal mol^{-1} versus -6.4 kcal mol^{-1}).

6.8 Conclusions and Discussion

This study shows that the host proteins DUSP3, 11 and 27 of the host cell are essential for intracellular growth of the bacteria *S. typhimurium*. In our approach we used a small interfering RNA (siRNA) screen of the human phosphatome and a reversed chemical screen. In the latter methodology we screened tyrosine-based small molecules as a general tyrosine/dual specificity phosphatase inhibitor library. One of the molecules (LH65.3) that resulted from the small molecule screen inhibited the identified DUSPs 3, 11 and 27 confirming the phosphatase target-inhibitor relationship.

Further development of LH65.3 resulted in a selective DUSP3 inhibitor (**8**) which has poor affinity for DUSP27. Molecular docking suggests that a hydrogen bond exists between inhibitor **8** and tyrosine residue Y130 in DUSP3 which is not present in DUSP27. This hydrogen bond probably explains the higher affinity of this inhibitor for DUSP3 over DUSP27.

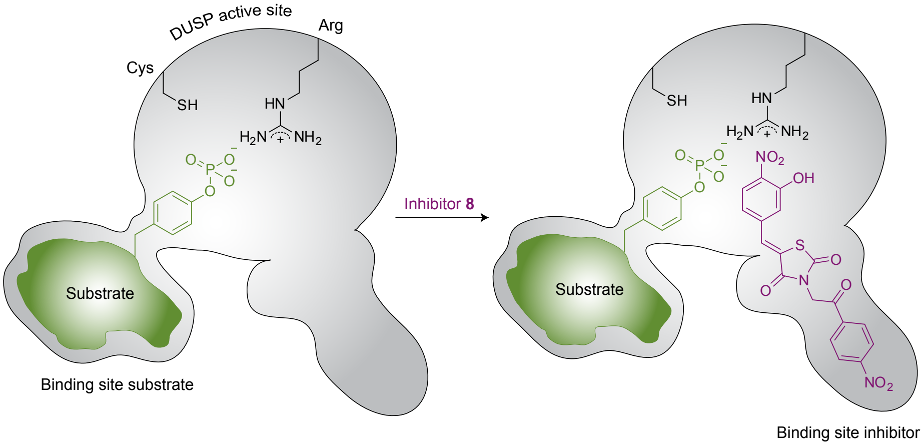

Figure 7: Model proposing the binding of inhibitors and tyrosine phosphorylated substrate with DUSP family phosphatases. Here DUSP inhibitor **8** (purple) is depicted as example. Tyrosine moieties of a substrate (green) and inhibitor **8** are located in the active site while the remaining part of these molecules binds to a different site in DUSP. Only the catalytic residues cysteine and arginine are depicted for clarity.

Development of selective phosphatase inhibitors is a challenging task because of their close homology.

Somewhat controversial is the fact that the mode of inhibition for this selective inhibitor **8** is non-competitive. The tyrosine moiety in this inhibitor is introduced to target the phosphatase active site. In addition, unbiased molecular docking of inhibitor **8** shows a preference for the catalytic site of DUSP3 and 27. Our hypothesis explaining our results is depicted in Figure 7. In this model the binding site of tyrosine moieties of a tyrosine phosphorylated DUSP substrate and selective inhibitor **8** are in proximity of each other in the large DUSP active site while the remaining parts of the molecules bind to different sites outside the DUSP active site. A crystal structure of inhibitor **8** in complex with DUSP3 or 27 should reveal its true binding.

In conclusion, targeting host DUSP proteins essential for bacterial growth seems to be a valid way to fight bacterial infection and holds promise as a new therapeutic strategy to treat these infections. This new approach could be a useful addition to the current bacterial infection treatments that target solely the bacteria itself.

6.9 Experimental section

General. See Experimental section Chapter 4.

Synthesis inhibitor library. Inhibitors were synthesized as previously described with minor adjustments to the protocol.[13-15] In short, to a cooled solution (277 K) of thiazolidine-2,4-dione (5.87 g, 50 mmol) in DMF (100 ml) sodium hydride (60% in oil, 1.8 g, 45 mmol) was added. A solution of the appropriate benzyl bromide (36.8 mmol) in DMF (25 ml) was added to the reaction mixture. The mixture was allowed to warm up to room temperature and was stirred for 4 h. Then the mixture was poured into of ice water (250 ml) and hexane (100 ml) was added. After a night at 277 K the precipitated crystals were filtrated and dried to give *N*-alkylated thiazolidine-2,4-dione.

The resulting *N*-alkylated thiazolidine-2,4-dione (0.317 mmol) was dissolved in ethanol (2.5 mL) containing piperidine (70 µL, 0.709 mmol) and the appropriate aldehyde (0.348 mmol) was added and the solution was refluxed overnight. Upon cooling to room temperature the product precipitated out of solution. Centrifugation and washing with ethanol gave homogeneous compound.

(*Z*)-3-(4-(tert-butyl)benzyl)-5-(4-hydroxy-3-nitrobenzylidene)thiazolidine-2,4-dione (LH65.3). Yield: 20%. **^{1}H NMR:** δ = 8.20 (d, *J* = 2.3, 1H), 7.95 (s, 1H), 7.77 (dd, *J* = 2.3, 8.8, 1H), 7.37 (d, *J* = 8.5, 2H), 7.25 (dd, *J* = 8.6, 11.0, 3H), 4.79 (s, 2H), 1.25 (s, 9H). **^{13}C NMR:** δ = 166.93, 165.37, 153.69, 150.28, 137.43, 135.51, 132.46, 131.63, 127.80, 127.49, 125.40, 123.93, 120.15, 119.96, 44.38, 34.21, 31.02. **MS:** m/z $[M+H]^+$ calc. 413.12, obs. 412.92.

(*Z*)-5-(3-hydroxy-4-nitrobenzylidene)-3-(2-(4-nitrophenyl)-2-oxoethyl)thiazolidine-2,4-dione (8). Yield: 26%. **^{1}H NMR:** δ = 8.41 (d, *J* = 9.0, 2H), 8.33 (d, *J* = 9.1, 2H), 8.02 (d, *J* = 8.5, 1H), 7.99 (s, 1H), 7.39 (d, *J* = 1.7, 1H), 7.27 (dd, *J* = 1.6, 8.6, 1H), 5.45 (s, 2H). **^{13}C NMR:** δ = 190.94, 166.52, 164.77, 152.44, 150.61, 138.63, 138.23, 137.53, 131.84, 129.89, 126.13, 124.36, 124.00, 120.47, 119.81, 48.28. **MS:** m/z $[M+H]^+$ calc. 430.03, obs. 429.87.

Phosphatase siRNA screen. Gene silencing was performed in 96 well plates with a human breast cancer (MCF-7) and glioblastoma (A-172) cell line. Cells were seeded at a density of 5000 cells per well and reverse transfected with DharmaFECT transfection reagent #4 and 50 nM siRNA (Human siGenome SMARTpool phosphatase library, Dharmacon). Two days after transfection, cells were infected with *S. Typhimurium* expressing DsRed[16] was performed based on the infection protocol described by Steele-Mortimer *et al*. with minor changes.[17] In short, two days before infection a bacterial culture was streaked from the frozen stock on LB agar plate. The next day, an overnight bacterial culture was prepared by inoculating 5 mL LB medium with one colony from the agar plate. The overnight culture was incubated at 310 K and 200 rpm for 16-20 h and then diluted 1:33 in fresh, pre-warmed (310 K) ampicillin (100 µg mL^{-1}) containing LB medium for a further incubation of 3.5 h. The bacterial culture (4 mL) was transferred to a 15 ml Falcon tube and pelleted in 4000 rpm for 10 min at room temperature. The pellet was washed once with DMEM/FCS and resuspended in DMEM/FCS full medium (310 K). The cells were infected with an MOI of 50 for 20 min. After infection the cells were washed 4 times with DMEM/FCS containing 100 µg mL^{-1} gentamycin and remaining extracellular bacteria were killed by addition of DMEM/FCS medium with 100 µg mL^{-1} gentamicin for 60 min. For the remaining infection period, the antibiotic concentration was lowered to 10 µg mL^{-1}. After overnight infection cells were washed once with PBS and 30 µL of trypsin/EDTA was added for 5 min followed by addition of 30 µL PBS/BSA 1%. The sample was fixed by addition of 60 µL PBS formalin 7%.

Samples were analyzed by flow cytometry (BD FACSArray) for DsRed fluorescence as marker for Salmonella infection and proliferation. The data were normalized (cellHTS2, Bioconductor) and transformed into Z-scores.[18]

Small molecule screen. The infection of mammalian cells (MCF-7 or A172) with *S. typhimurium* expressing DsRed[16] was performed based on the infection protocol described by Steele-Mortimer *et al*. with minor changes.[17] In short, two days before infection a bacterial culture was streaked from the frozen stock on an ampicillin containing LB agar plate. The next day, an overnight bacterial culture was prepared by inoculating 5 mL of ampicillin containing LB medium with one colony from the agar plate. The overnight culture was incubated at 310 K and 200 rpm for 16-20 h and then diluted 1:33 in 5 mL fresh, pre-warmed (310 K) ampicillin containing LB medium for a further incubation of 3.5 h. 4 mL the culture was transferred to 15 mL Falcon tube and pelleted at 4000 rpm for 10 min at room temperature. The pellet was washed once with DMEM/FCS and resuspended in DMEM/FCS (310 K). In order to infect the cells with the MOI 20 for 30 min, the bacterial culture was diluted according to the following assumption: OD_{595} of 1 ≈ 1.3 x 10^9 CFU mL^{-1}. To infect cells with bacteria, the cell culture medium was aspirated and 100 µL of bacteria in DMEM/FCS was added to the wells. Plates were centrifuged at 1000 rpm at room temperature for 5 min and incubated at 310 K with 5% CO_2 in a humidified cell culture incubator to allow invasion for 1 h. The cells were washed 4 times with DMEM/FCS containing 100 µg mL^{-1} gentamycin and incubated for another 1 h in DMEM/FSC containing 100 µg mL^{-1} gentamycin. For the remaining infection period, the media was replaced with DMEM/FCS containing 10 µg mL^{-1} gentamicin and compound if indicated. Compounds were tested at 10 µM in triplicate.

After overnight infection cells were washed once with PBS and incubated in 30 µl of trypsin/EDTA for 5-10 min. Subsequently, 30 µL PBS/1% BSA was added used to resuspend the cells. 60 µL PBS/formalin (7%) was added to fix cells and bacteria. After at least 2 h samples were measured by FACS as previously described.

Effect of compounds on *S. typhimurium* growth in LB medium. An overnight bacterial culture was prepared by inoculating 5 mL of ampicillin (100 µg mL^{-1}) containing LB medium with one colony from an agar plate. The overnight culture was incubated at 310 K and 200 rpm for 16-20 h and then diluted 1:33 in fresh ampicillin (100 μg mL^{-1}) containing LB medium. In a 96-wells plate, 100 μL of the bacteria containing medium was pipetted to an LB medium (100 μL) containing 20 μM of inhibitor. Bacterial growth was monitored by measuring the optical density at 595 nm (OD_{595}).

Cell toxicity. See Experimental section Chapter 2.

DUSP activity assay.[7] Measuring DUSP activity using 3-*O*-methylfluorescein phosphate (OMFP) as a substrate[19] was determined as follows. In a black flat-bottom 96-wells plate was added 0.9 μL DMSO containing inhibitor, to 45 μL recombinant DUSP (~0.1 U) in a Tris-HCl buffer (9 mM Tris-HCl, 11 mM NaCl, 1 mM EDTA, 1 mM DTT, 0.01% triton X-100, pH 7.4). Finally, 45 μL of 40 μM OMFP in the previously described Tris-HCl buffer was added to each well using a multichannel pipet and instantaneously fluorescence was measured at room temperature ($\lambda_{ex}/\lambda_{em}$ = 485/520 nm). The above described mixture with DMSO alone was used as a positive control. OMFP without DUSP was taken as control for auto-hydrolysis of OMFP. For each inhibitor percentage inhibition (PI) was determined at a final inhibitor concentration of 5 μM. IC_{50} values of inhibitors have been determined in an inhibitor concentration range of 0.01 to 6 μM. Data were analyzed using Graphpad Prism software. In addition, the effect of the inhibitors on the fluorescence of the produced OMF was investigated using ~1 μM OMF at an inhibitor concentration of 5 μM (Supporting Figure S3).

Cloning, expression and purification of DUSPs. PCR fragments of phosphatase domains of DUSP3, 11 and 27 (Supporting Table S2) containing a His-tag sequence have been cloned into a pETNKI-His-3c-LIC-kan vector[20] and were sequence verified. The resulting constructs have been transformed into BL21 (DE3) cells. Transformed cells were grown overnight in LB medium (2 mL) containing kanamycin (30 μg mL^{-1}) and were subsequently inoculated in LB medium (1 L) with kanamycin (30 μg mL^{-1}) until an OD_{595} of 0.6 was reached. Protein expression was induced by IPTG (0.5 mM) overnight at 293 K. Cells were spun down (3,000 x g, 15 min, 277 K) and the resulting cell pellet was resuspended in a Tris buffer (40 mM Tris, 200 mM NaCl, 5 mM β-mercaptoethanol, 5 mM imidazol, pH 8.0). After sonification the resuspension the cell debris and insoluble proteins were removed by centrifugation (14,000 x g, 30 min, 277 K) and the soluble fraction was incubated with Talon beads and washed with the above described Tris buffer. The Talon beads were eluted with a Tris buffer (40 mM Tris, 200 mM NaCl, 5 mM β-mercaptoethanol, 300 mM imidazol, pH 8.0) and collected fractions were analyzed on an SDS-PAGE gel. Fractions containing solely DUSP protein were pooled and purified by resource Q anion-exchange chromatography. For crystallization purpose, the His-tag purification label of DUSP27 was removed by GST-tagged 3C protease cleavage overnight at 277 K. A final purification step of all DUSPs involved a S75 gel filtration using as eluent a Tris buffer (40 mM Tris, 100 mM NaCl, 5 mM β-mercaptoethanol, pH 8.0) resulting in a pure protein solution which was concentrated using a Centriprep column.

DUSP27 Crystallization. Screening of crystallization conditions for DUSP27 was performed at nanoliter scale in 96-well format. 200 nL sitting drops (100 nL DUSP27 (5 mg mL^{-1}) and 100 nL reservoir solution) were prepared by the Mosquito dispensing robot (TTP Labtech) using the PACT and JCSG+ screens.[21] Crystallization plates were stored and imaged at 277 K by the RockImager (Formulatrix) and at 293 K by the CrystalFarm (Bruker-AXS). Initial microcrystals and needle-like crystals were observed at 277 K in conditions from the PACT screen containing 0.1 M bis-Tris propane (pH 6.5 and pH 7.5), 20% PEG 3350 and either 0.2 M sodium nitrate, 0.2 M sodium fluoride or 0.2 M sodium-potasium phosphate. These crystals were used in microseeding experiments against the PACT and JCSG+ screen. Briefly, crystals were transferred to 75 μL of reservoir solution in an eppendorf tube and vortexed for 30 s. Sitting drops were prepared from 100 nL of DUSP27 (5 mg mL^{-1}), 100 nL reservoir solution and 10 nL seed solution. Crystals were observed in multiple conditions and further optimization of these conditions was performed using the Formulator microfluidics liquid dispensing robot (Formulatrix) with microseeding. Suitable crystals for X-ray diffraction studies were obtained at 277 K in 0.1 M Tris pH 8.0, 21% PEG 3350, 0.2 M sodium sulphate; in 0.1 M Tris pH 7.2, 12% PEG 8000; in 0.1 M Tris pH 7.5, 0.2 M magnesium chloride and 16% PEG 6000. Crystals appeared as needles and as plates, with typical dimensions of 0.05 x 0.1 x 0.3 mm and 0.1 mm x 0.2 mm x 0.25 mm, respectively.

Data collection and structure refinement. DUSP27 X-ray diffraction data was collected at 100 K from a crystal grown in 0.1 M Tris pH 7.5, 0.2 M magnesium chloride and 16% PEG 6000 at our home source (Microstar Ultra II (Bruker-AXS) with Mar345 image plate detector (Marresearch)). The crystal was cryoprotected in 0.1 M Tris pH 7.5, 0.2 M magnesium chloride, 18% PEG 6000 and 20% glycerol before freezing in liquid nitrogen solution. 100 images were collected with 1 degree oscillation and 120 s exposure per frame and a crystal to detector distance of 200 mm (2.21 Å resolution at the edge of the detector). The diffraction data set was indexed and integrated using Mosflm[22] and scaled using SCALA.[23] Molecular replacement using the structure of DUSP13 (PDB ID: 2PQ5) as search model, was performed in Phaser.[24] An initial model was build and revealed 2 molecules in the asymmetric unit. The model was subjected to automated tracing in ARP/wARP[25] and was further refined using the software programs Refmac in CCP4[26] interspersed with manual rebuilding in Coot.[27] Data collection and refinement statistics can be found in Supporting Table S3.

Molecular docking, protein and ligand preparation. The X-ray structures of DUSP3 (PDB ID: 1VHR) and DUSP27 were used for docking studies. The protein and ligand structures were prepared using Autodock version 1.5.4. The initial 3D structures of the ligands were generated using CORINA. We defined a region for docking by a 30 Å x 30 Å x 30 Å box centered around the P1 and P2 pocket of DUSP3 and 27. Final docking experiments were done using Autodock Vina.[28] Graphics were made using PyMOL 1.3.

6.10 References

1. Turner, M. Microbe outbreak panics Europe. *Nature (London, U. K.)* **474**, 137 (2011).
2. Nikaido, H. Multidrug resistance in bacteria. *Annu. Rev. Biochem.* **78**, 119-146 (2009).
3. Vergne, I. Chua, J. Singh, S. & Deretic, V. Cell Biology of Mycobacterium Tuberculosis Phagosome. *Annu. Rev. Cell Dev. Biol.* **20**, 367-394 (2004).
4. Uchiya, K. & Nikai, T. Salmonella enterica Serovar Typhimurium Infection Induces Cyclooxygenase 2 Expression in Macrophages: Involvement of Salmonella Pathogenicity Island 2. *Infect. Immun.* **72**, 6860-6869 (2004).
5. Kuijl, C. et al. Intracellular bacterial growth is controlled by a kinase network around PKB/AKT1. *Nature* **450**, 725-730 (2007).
6. Hunter, T. Protein kinases and phosphatases: The Yin and Yang of protein phosphorylation and signaling. *Cell* **80**, 225-236 (1995).
7. Tierno, M. et al. Development and optimization of high-throughput in vitro protein phosphatase screening assays. *Nat. Protoc.* **2**, 1134-1144 (2007).
8. Schumacher, M. Todd, J. Rice, A. Tanner, K. & Denu, J. Structural Basis for the Recognition of a

Bisphosphorylated MAP Kinase Peptide by Human VHR Protein Phosphatase. *Biochemistry* **41**, 3009-3017 (2002).

9. Wu, S. et al. Multidentate Small-Molecule Inhibitors of Vaccinia H1-Related (VHR) Phosphatase Decrease Proliferation of Cervix Cancer Cells. *J. Med. Chem.* **52**, 6716-6723 (2009).
10. Yuvaniyama, J. Denu, J. Dixon, J. & Saper, M. Crystal Structure of the Dual Specificity Protein Phosphatase VHR. *Science* **272**, 1328-1331 (1996).
11. Friedberg, I. et al. Identification and characterization of DUSP27, a novel dual-specific protein phosphatase. *FEBS Lett.* **581**, 2527-2533 (2007).
12. Lountos, G. Tropea, J. & Waugh, D. Structure of human dual-specificity phosphatase 27 at 2.38Å resolution. *Acta Cryst. D* **67**, 471-479 (2011).
13. Albers, H. M. et al. Discovery and Optimization of Boronic Acid Based Inhibitors of Autotaxin. *J. Med. Chem.* **53**, 4958-4967 (2010).
14. Albers, H. M. et al. Structure-Based Design of Novel Boronic Acid-Based Inhibitors of Autotaxin. *J. Med. Chem.* **54**, 4619-4626 (2011).
15. Albers, H. M. et al. Boronic acid-based inhibitor of autotaxin reveals rapid turnover of LPA in the circulation. *Proc. Natl. Acad. Sci. USA* **107**, 7257-7262 (2010).
16. Sörensen, M. et al. Rapidly maturing red fluorescent protein variants with strongly enhanced brightness in bacteria. *FEBS Lett.* **552**, 110-114 (2003).
17. Steele-Mortimer, O. Méresse, S. Gorvel, J. Toh, B. & Finlay, B. B. Biogenesis of Salmonella typhimurium-containing vacuoles in epithelial cells involves interactions with the early endocytic pathway. *Cell. Microbiol.* **1**, 33-49 (1999).
18. Boutros, M. Bras, L. & Huber, W. Analysis of cell-based RNAi screens. *Genome Biol.* **7**, R66 (2006).
19. Tamura, K. et al. Cdc25 Inhibition and Cell Cycle Arrest by a Synthetic Thioalkyl Vitamin K Analogue. *Cancer Res.* **60**, 1317-1325 (2000).
20. Luna-Vargas, M. et al. Enabling high-throughput ligation-independent cloning and protein expression for the family of ubiquitin specific proteases. *J. Struct. Biol.* **175**, 113-119 (2011).
21. Egan, D. et al. Towards rationalization of crystallization screening for small- to medium-sized academic laboratories: the PACT/JCSG+ strategy. *Acta Cryst. D* **61**, 1426-1431 (2005).
22. Leslie, A. G. W. Recent changes to the MOSFLM package for processing film and image plate data. *Joint CCP4 + ESF-EAMCB Newsletter on Protein Crystallography* **26**, (1992).
23. Evans, P. Scaling and assessment of data quality. *Acta Cryst. D* **62**, 72-82 (2006).
24. McCoy, A. et al. Phaser crystallographic software. *J. Appl. Cryst.* **40**, 658-674 (2007).
25. Perrakis, A. Morris, R. & Lamzin, V. Automated protein model building combined with iterative structure refinement. *Nat. Struct. Mol. Biol.* **6**, 458-463 (1999).
26. Collaborative Computational Project, N. The CCP4 suite: programs for protein crystallography. *Acta Cryst. D* **50**, 760-763 (1994).
27. Emsley, P. Lohkamp, B. Scott, W. G. & Cowtan, K. Features and development of Coot. *Acta Cryst. D* **66**, 486-501 (2010).
28. Trott, O. & Olson, A. AutoDock Vina: Improving the speed and accuracy of docking with a new scoring function, efficient optimization, and multithreading. *J. Comput. Chem.* **31**, 455-461 (2010).

6.11 Supporting information

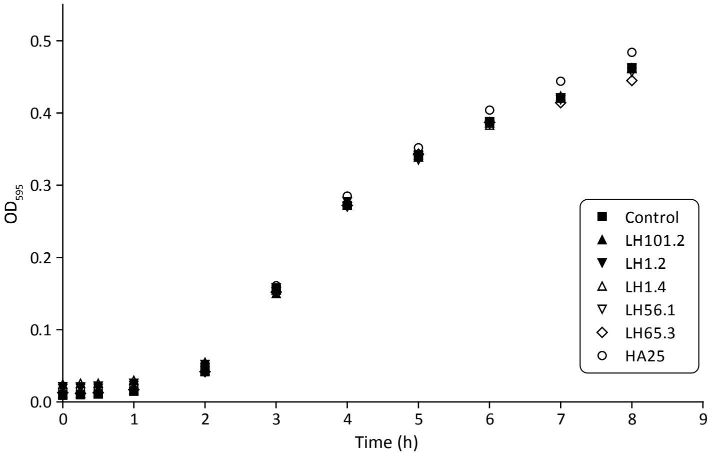

Supporting Figure S1: Effect of compounds on *S. typhimurium* growth in LB medium. Bacterial growth of *S. typhimurium* was measured in the presence or absence of 10 µM of compound at a wavelength of 595 nm. Data points have not been fitted for clarity.

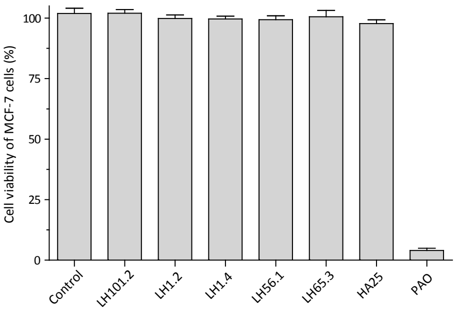

Supporting Figure S2: Effect of compounds on cell viability of MCF-7 cells. Cell viability of MCF-7 cells was tested using the conditions of the *S. typhimurium* FACS assay. Compounds were incubated for 42 h at a concentration of 10 µM. Phenylarsine oxide (PAO) was used as a control for cell death.

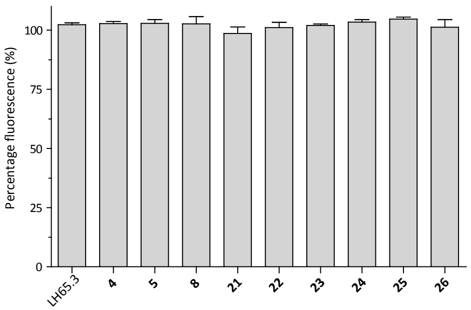

Supporting Figure S3: Effect of DUSP inhibitors on DUSP activity assay readout. Fluorescence of OMF was measured at an inhibitor concentration of 5 µM.

Supporting Table S1: List of screened phosphatase and phosphatase-like siRNAs

Name	Catalog number	Locus id	Accession id
ENPP2	M-004601-01	5168	NM_006209
PTPN6	M-009778-00	5777	NM_002831
C7ORF16	M-018324-01	10842	NM_006658
CDKN3	M-003879-00	1033	NM_005192
DUSP1	M-003484-02	1843	NM_004417
DUSP10	M-003965-01	11221	NM_007207
DUSP2	M-003565-01	1844	NM_004418
DUSP22	M-004517-00	56940	NM_020185
DUSP4	M-003963-02	1846	NM_001394
DUSP5	M-003566-01	1847	NM_004419
DUSP6	M-003964-01	1848	NM_001946
DUSP7	M-003567-00	1849	XM_037430
DUSP8	M-003568-00	1850	NM_004420
ILKAP	M-010260-00	80895	NM_030768
PFKFB1	M-006761-00	5207	NM_002625
PFKFB2	M-006762-01	5208	NM_006212
PFKFB3	M-006763-00	5209	NM_004566
PFKFB4	M-006764-00	5210	NM_004567
PPP1R1B	M-012745-00	84152	NM_032192
PPP2CA	M-003598-00	5515	NM_002715
PPP4C	M-008486-01	5531	NM_002720
PTPN5	M-003600-01	84867	NM_032781
PTPRG	M-008069-00	5793	NM_002841
PTPRJ	M-008476-01	5795	NM_002843
PTPRR	M-004017-01	5801	NM_002849
PTPRT	M-008072-01	11122	NM_007050
TRIO	M-005047-00	7204	NM_007118
ACYP2	M-008864-00	98	NM_138448
PPP1R16B	M-004065-00	26051	NM_015568
PPP2R3A	M-017376-00	5523	NM_002718
SAG	M-011105-00	6295	NM_000541
ZFHX1B	M-006914-00	9839	NM_014795
ACP5	M-009615-01	54	NM_001611
PPP3CA	M-008300-01	5530	NM_000944
PSPH	M-011888-01	5723	NM_004577
ACP1	M-019058-00	52	NM_004300
ACPP	M-009262-00	55	NM_001099
CDC14A	M-003469-00	8556	NM_003672
CDC14B	M-003470-02	8555	NM_003671
CDC25A	M-003226-02	993	NM_001789
CDC25B	M-003227-02	994	NM_004358
CDC25C	M-003228-01	995	NM_001790
DUSP11	M-007885-00	8446	NM_003584
EPM2A	M-006896-01	7957	NM_005670
PPAP2B	M-017312-01	8613	NM_003713
PPAP2C	M-011500-00	8612	NM_003712
PPM1D	M-004554-00	8493	NM_003620
PPP1R3C	M-017077-00	5507	NM_005398
PTEN	M-003023-01	5728	NM_000314
PTPN14	M-008509-00	5784	NM_005401
PTPRU	M-009328-01	10076	NM_005704
TPTE2	M-008107-00	93492	NM_130785
CTDP1	M-009326-01	9150	NM_004715
DUSP12	M-007886-01	11266	NM_007240
DUSP13	M-007887-00	51207	NM_016364
DUSP14	M-007888-00	11072	NM_007026
DUSP15	M-008484-01	128853	NM_080611
DUSP18	M-007891-00	150290	NM_152511
DUSP19	M-007892-01	142679	NM_080876
DUSP21	M-007893-01	63904	NM_022076
DUSP23	M-007909-00	54935	NM_017823
MGC1136	M-008027-01	78986	NM_024025
MGC26484	M-008030-00	168448	XM_171149
MK-STYX	M-008031-01	51657	NM_016086
MTMR1	M-008037-01	8776	NM_003828
MTMR2	M-008038-00	8898	NM_016156
MTMR4	M-008040-01	9110	NM_004687
MTMR7	M-008041-00	9108	XM_044727
PDP2	M-022572-00	57546	NM_020786
PPEF1	M-009479-00	5475	NM_006240
PPEF2	M-012250-01	5470	NM_006239
PPM1B	M-008281-01	5495	NM_002706
PPM1E	M-008964-00	22843	NM_014906
PPM1F	M-009544-00	9647	NM_014634
PPM1G	M-005264-01	5496	NM_002707
PPM1L	M-008679-00	151742	NM_139245
PPM2C	M-008718-00	54704	NM_018444
PPP1CA	M-008927-00	5499	NM_002708
PPP1CB	M-008685-00	5500	NM_002709
PPP2R1A	M-010259-01	5518	NM_014225
PPP2R5A	M-009352-01	5525	NM_006243
PPP2R5B	M-009366-00	5526	NM_006244
PPP2R5C	M-009433-00	5527	NM_002719
PPP2R5D	M-009799-01	5528	NM_006245
PPP2R5E	M-008531-01	5529	NM_006246
PPP3CC	M-010005-00	5533	NM_005605
PPP5C	M-009259-00	5536	NM_006247
PPP6C	M-009935-01	5537	NM_002721
PTP4A1	M-006333-01	7803	NM_003463
PTP4A2	M-009078-00	8073	NM_003479
PTP4A3	M-006859-01	11156	NM_007079
PTPDC1	M-008584-00	138639	NM_152422
PTPLA	M-008742-00	9200	NM_014241
PTPN1	M-003529-04	5770	NM_002827
PTPN11	M-003947-01	5781	NM_002834
PTPN12	M-008064-01	5782	NM_002835
PTPN13	M-008065-00	5783	NM_006264
PTPN21	M-009379-01	11099	NM_007039
PTPN22	M-008066-00	26191	NM_012411
PTPN23	M-009417-00	25930	NM_015466
PTPN3	M-009372-01	5774	NM_002829
PTPN4	M-009489-01	5775	NM_002830
PTPN7	M-008394-00	5778	NM_002832
PTPN9	M-008832-00	5780	NM_002833
PTPRA	M-004519-00	5786	NM_002836
PTPRB	M-004994-02	5787	NM_002837
PTPRC	M-008067-00	5788	NM_002838
PTPRD	M-008527-00	5789	NM_002839

Name	Catalog number	Locus id	Accession id
PTPRE	M-008068-02	5791	NM_006504
PTPRF	M-008375-01	5792	NM_002840
PTPRH	M-009448-00	5794	NM_002842
PTPRK	M-004204-01	5796	NM_002844
PTPRM	M-006326-00	5797	NM_002845
PTPRN	M-009315-01	5798	NM_002846
PTPRN2	M-008070-00	5799	NM_002847
ACP2	M-008205-00	53	NM_001610
INPP5B	M-021811-01	3633	NM_005540
ALPPL2	M-003455-01	251	NM_031313
PPP3R1	M-009869-01	5534	NM_000945
IGBP1	M-011298-01	3476	NM_001551
ANP32E	M-015844-00	81611	NM_030920
LPPR4	M-009911-00	9890	NM_014839
PPP2CB	M-003599-02	5516	NM_004156
ENPP1	M-003809-01	5167	NM_006208
MAP3K7IP1	M-004770-00	10454	NM_006116
ACP6	M-008665-00	51205	NM_016361
INPP5D	M-003013-01	3635	NM_005541
DUT	M-010258-00	1854	NM_001948
SYNJ1	M-019486-01	8867	NM_003895
PPP1R11	M-011917-01	6992	NM_021959
DKFZP761G058	M-018772-00	152926	NM_152542
FLJ40125	M-009006-00	147699	NM_178494
AKAP11	M-009277-01	11215	NM_016248
BPNT1	M-008664-01	10380	NM_006085
PPM1A	M-009574-01	5494	NM_021003
ACPT	M-008366-01	93650	NM_033068
PHPT1	M-016904-00	29085	NM_014172
ENPP3	M-004540-00	5169	NM_005021
PTPN2	M-008969-00	5771	NM_002828
PPP1R7	M-019589-00	5510	NM_002712
LOC151242	M-023104-00	151242	XM_087137
HSPC129	M-008272-00	51496	NM_016396
MTM1	M-008036-01	4534	NM_000252
ALPP	M-003454-01	250	NM_001632
MTMR3	M-008039-01	8897	NM_021090
ENPP4	M-009214-01	22875	NM_014936
PON1	M-009229-00	5444	NM_000446
IMPA1	M-010172-01	3612	NM_005536
PPP1R8	M-010903-00	5511	NM_002713
PPP2R4	M-005214-00	5524	NM_021131
C21ORF6	M-013856-00	10069	NM_016940
DUSP3	M-007894-00	1845	NM_004090
ALPI	M-008673-00	248	NM_001631
TPTE	M-008745-01	7179	NM_013315
ENPP5	M-009805-01	59084	NM_021572
PON2	M-009676-00	5445	NM_000305
IMPA2	M-008348-00	3613	NM_014214
PPP2R2A	M-004824-01	5520	NM_002717
OCRL	M-010026-01	4952	NM_000276
ENPP7	M-009059-00	339221	NM_178543
PTPRS	M-009662-01	5802	NM_002850
SSH3	M-008937-00	54961	NM_017857
FBP2	M-010139-01	8789	NM_003837
PPAP2A	M-019098-00	8611	NM_003711
INPP1	M-008505-01	3628	NM_002194
PR48	M-019459-00	28227	NM_013239
PIB5PA	M-009108-00	27124	NM_014422
TENS1	M-009997-00	64759	NM_022748
C14ORF24	M-018433-00	283635	NM_173607
STYX	M-009571-01	6815	NM_145251
PTPN18	M-009385-00	26469	NM_014369
RNGTT	M-009782-00	8732	NM_003800
FHIT	M-004952-01	2272	NM_002012
SYNJ2	M-012624-00	8871	NM_003898
PPP1CC	M-006827-00	5501	NM_002710
PME-1	M-005211-00	51400	NM_016147
CILP	M-008295-00	8483	NM_003613
FLJ23751	M-008557-00	92370	NM_152282
FRMPD2	M-008854-00	143162	NM_152428
MINPP1	M-009705-00	9562	NM_004897
PTPRZ1	M-009685-00	5803	NM_002851
INPP4B	M-011539-00	8821	NM_003866
ALPL	M-008658-00	249	NM_000478
PPP1R2	M-015361-00	5504	NM_006241
I-4	M-012962-00	80316	NM_025210
RWDD2	M-015117-00	112611	NM_033411
DNAJC6	M-009885-00	9829	NM_014787
ENPP6	M-008704-00	133121	NM_153343
FBP1	M-008725-00	2203	NM_000507
PPP2R2B	M-003022-01	5521	NM_004576
PTPRO	M-008500-01	5800	NM_002848

Supporting Table S2: Amino acid sequences of DUSP3, 11 and 27. The catalytic domain containing the HCXXGXXR motif is underlined.

DUSP	Amino acid sequence
3	MAHHHHHHSAALEVLFQGPGMSGSFELSVQDLNDLLSDGSGCYSLPSQPCNEVTPRIYVGNASVAQDIPKLQKLGITHVLNAAEGRSFMHVNTNANFYKDSGITYLGIKANDTQEFNLSAYFERAADFIDQALAQKNGRVLVHCREGYSRSPTLVIAYLMMRQKMDVKSALSIVRQNREIGPNDGFLAQLCQLNDRLAKEGKLKP
11	MAHHHHHHSAALEVLFQGPGRFIAFKVPLQKSFEKKLAPEECFSPLDLFNKIREQNEELGLIIDLTYTQRYYKPEDLPETVPYLKIFTVGHQVPDDETIFKFKHAVNGFLKENKDNDKLIGVHCTHGLNRTGYLICIYLIDVEGVRPDDAIELFNRCRGHCLERQNYIEDLQNGPIRKNWNSSVPRSSDFEDSAHLMQPVHNKPVKQGPRYNLHQIQGHSAPRHFHTQTQSLQQSVRKFSENPHVY
27 [a]	**MAHHHHHHSAALEVLFQG**PGYTHVNEVWPKLYIGDEATALDRYRLQKAGFTHVLNAAHGRWNVDTGPDYYRDMDIQYHGVEADDLPTFDLSVFFYPAAAFIDRALSDDHSKILVHCVMGRSRSATLVLAYLMIHKDMTLVDAIQQVAKNRCVLPNRGFLKQLRELDKQLVQQRRRSQRQDGEEEDGREL

[a] *In bold the amino acid sequence removed by GST-tagged 3C protease for crystallization purposes.*

Supporting Table S3: Data collection and refinement statistics for DUSP27.

	DUSP27
Data collection	
Space group	$P2_12_12$
Cell dimensions	
a, *b*, *c* (Å)	56.11, 60.62, 54.55
a, b, g (°)	90, 90, 90
Resolution (Å)	2.2 (2.33-2.2)
R_{sym} or R_{merge}	0.094 (0.54)
I / s*I*	4.0 (3.4)
Completeness (%)	97.6 (97.6)
Redundancy	3.8 (3.6)
Refinement	
Resolution (Å)	20-2.2
No. reflections	8598
R_{work} / R_{free}	0.28/0.32
R.m.s. deviations	
Bond lengths (Å)	0.012
Bond angles (°)	1.508

APPENDICES

Summary and future prospects

Nederlandse samenvatting

Curriculum Vitae

List of publications

Nawoord

Summary and future prospects

Autotaxin inhibitors

The first part of this thesis describes the development of inhibitors of autotaxin (ATX or ENPP2), a phosphodiesterase that is responsible for the production of the lipid lysophosphatidic acid (LPA) in the circulation. ATX is implicated in several diseases including inflammation, fibrotic disease and cancer, making it an interesting potential drug target to study. ATX inhibitors are required in the validation process of ATX as a drug target. However, at the start of this study, small molecule ATX inhibitors did not exist. In order to discover ATX inhibitors, ~40,000 small molecules were screened and several structural classes of inhibitors were identified (**Chapters 2** and **3**). After validation experiments a class of small molecules called thiazolidine-2,4-diones proved to be the most promising. This class was amenable to chemical optimization, allowing the synthesis and isolation of ~100 analogs of the confirmed thiazolidine-2,4-dione screening hit (Figure 1). In the handed optimization approach variations were introduced in a benzyl moiety (green) and a benzylidene moiety (blue), which are linked *via* a thiazolidine-2,4-dione core (Figure 1). The key step in the optimization approach was the replacement of a carboxylic acid in one of the screening hit analogs by a boronic acid. The boronic acid was introduced to target the oxygen nucleophile in threonine 210 (T210), an amino acid in the ATX active site which is essential for the activity of this enzyme. This modification resulted in a boronic acid-based inhibitor (HA130; IC_{50} = 30 nM, Figure 1) with almost a 100-fold increase in potency compared to our original screening hit (IC_{50} = 2.5 µM).

Next, the biological properties of HA130 as ATX inhibitor were explored (**Chapter 2**). It was shown that HA130 is a selective inhibitor of ATX and that it does not inhibit ENPP1, the closest family member of ATX. Finally, it was demonstrated that HA130 instantaneously lowers plasma levels of LPA in mice after intravenous administration. This implies that the production of LPA by ATX and LPA degradation by other enzymes is tightly and dynamically regulated. Thus, ATX can be targeted *in vivo* using boronic acid-based inhibitors.

The development of ATX inhibitors described in **Chapters 2** and **3** was conducted before the ATX crystal structure was resolved.

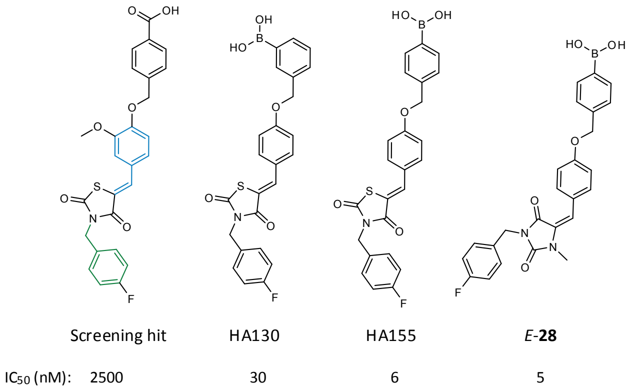

Figure 1: Selection of ATX inhibitors described in this thesis. Benzyl and benzylidene moiety in the screening hit are highlighted in green and blue, respectively.

In 2011, we obtained a crystal structure of ATX in complex with boronic acid-based inhibitor HA155 (IC_{50} = 6 nM, Figure 1). HA155 is a positional boronic acid isomer of HA130 with a higher affinity for ATX compared to HA130 (**Chapter 3**). The structure of HA155 bound to ATX proved that the boronic acid in HA155 indeed targets the threonine oxygen nucleophile in the ATX active site. Next, this structure was used to design new boronic acid-based inhibitors and replaced the thiazolidine-2,4-dione core in HA155 with other cores (**Chapter 4**) and variations of the ether linker in HA155 were investigated. This study finally led to the discovery of a highly active imidazolidine-2,4-dione analog of HA155 (*E*-**28**, IC_{50} = 5 nM) which had an *E*-configured double bond instead of a *Z*-configuration as in HA155 and all other evaluated analogs (Figure 1). To explain how *E*-**28** could bind to ATX molecular docking studies were performed. These studies suggested that *E*-**28** binds differently to the hydrophobic pocket in ATX compared to HA155 and other *Z*-configured analogs, opening possibilities for new inhibitor designs.

New inhibitor designs that could fully exploit the hydrophobic pocket in ATX are designs based on *E*-**28**. Extension from the methylene moiety in the 4-fluorobenzyl group of *E*-**28** with other aromatic moieties could target both regions in the hydrophobic pocket that are separately targeted by *E*-**28** and HA155 alone.

Since the current series of ATX inhibitors contain a fluorine atom, the introduction of the positron-emitting radionuclide fluorine-18 (F18) is an option. This will allow tracing of inhibitors *in vivo* (e.g. mice) using Positron Emission Tomography (PET) imaging to gather information about the pharmacokinetics of these inhibitors.

To validate ATX as a drug target, besides to ATX inhibitors, proper animal model systems that mimic ATX-driven diseases are needed. Few of these models exist today, especially proper models regarding cancer are lacking. Generation of such models and using them in combination with ATX inhibitors is the next step in the validation of ATX as a drug target.

DUSP inhibitors

After a short introduction on dual specificity phosphatases (DUSP, **Chapter 5**) the involvement of host phosphatases in bacterial infection of human host cells was studied. In this study a small interfering RNA (siRNA) phosphatase library was screened to learn which host phosphatases are required for the bacterial growth of *Salmonella (S.) typhimurium* in human host cells (**Chapter 6**). Among the phosphatases identified many DUSPs (DUSP3, 11 and 27) were present. In parallel, a tyrosine phosphatase-targeted small molecule library was tested in order to discover molecules that inhibit *S. typhimurium* growth in human cells. Several compounds inhibited *S. typhimurium* growth in human host cells and one of these compounds inhibited the DUSPs that were identified from the siRNA screen. The most promising compound was then further optimized to result in a potent and selective DUSP3 inhibitor (IC_{50} = 0.33 µM), with a 15-fold increased potency compared to DUSP27 (IC_{50} > 5 µM). Molecular docking of this compound in both DUSP3 and 27 suggests a hydrogen bond between this inhibitor and a tyrosine residue in DUSP3, which cannot be formed in DUSP27, explaining the selectivity of this inhibitor. This tyrosine residue is present in the active site of DUSP3 but is not conserved in the DUSP active site consensus sequence (HCXXGXXR). Therefore, targeting non-conserved active site residues in DUSPs could be a valid strategy for the development of selective DUSP inhibitors. Developing selective phosphatase inhibitors is a challenging task due to the highly conserved active site residues in phosphatases.

For the optimization of DUSP inhibitors a similar approach was taken as for the first optimization method used for the ATX inhibitors. In this method only the outer parts (benzyl and benzylidene moieties) of the inhibitor were modified and the thiazolidine-2,4-dione core part was left untouched. For increasing affinity and/or selectivity of the DUSP inhibitors it would be useful to introduce variations in the thiazolidine-2,4-dione core of the DUSP inhibitors using, for example, modifications that are described in **Chapter 4**.

The approach taken in **Chapter 6** to inhibit host DUSP proteins that are essential for bacterial growth, seems to be a valid way to control bacterial infection. This new approach could be a useful addition to the current treatment of bacterial infections that target solely the bacteria itself, and hold promise as a new therapeutic strategy to treat bacterial infections with less chance for the development of drug resistance.

Nederlandse samenvatting

Ontwikkeling van ATX- en DUSP-remmers

ATX-remmers

Autotaxine (ATX) is een enzym met lysofosfolipase D activiteit en is verantwoordelijk voor de productie van het bioactieve lipide lysofosfatidezuur (LPA) in de bloedcirculatie. LPA activeert verschillende processen in de cel zoals proliferatie, migratie en overleving van de cel. ATX en LPA lijken betrokken te zijn bij diverse ziekten zoals kanker, (chronische) ontstekingen en fibrose. Het is tot op heden echter nog niet duidelijk wat de exacte functies van ATX en LPA zijn in de ontwikkeling van deze ziektes. ATX-remmers kunnen hierin duidelijkheid verschaffen door bijvoorbeeld ATX te remmen in diermodellen waarin ATX-gerelateerde ziektes zijn opgewekt. Indien deze ATX-remmers een positief effect vertonen in de genoemde diermodellen dan kunnen ze direct verder ontwikkeld worden tot nieuwe medicijnen voor de mens.

In het begin van dit onderzoek waren er nog geen actieve en selectieve remmers voor ATX bekend. Er is daarom eerst een bibliotheek van ~40.000 commercieel verkrijgbare kleine moleculen getest op hun mogelijkheid om ATX te remmen. Dat heeft geresulteerd in de identificatie van een chemische klasse van verbindingen van gesubstitueerde thiazolidine-2,4-dionen, die ATX selectief bleken te remmen. De beste verbinding van deze klasse is geselecteerd en chemisch gemodificeerd om het vermogen als ATX-remmer te optimaliseren. Deze optimalisatie heeft uiteindelijk een ATX-remmer opgeleverd, genaamd HA130, met een 100 maal sterkere activiteit voor ATX. De belangrijkste modificatie was de introductie van een boorzuurgroep, ontworpen om te binden aan het katalytische threonine-residu in het actieve centrum van ATX om zo de activiteit van ATX te blokkeren.

Vervolgens is het effect van HA130 op de productie van LPA in het bloed van muizen onderzocht. Toediening van deze remmer aan muizen resulteerde in een zeer snelle verlaging van het LPA-niveau in het bloed. Hieruit bleek dat de productie en degradatie van LPA in de bloedcirculatie veel dynamischer is dan eerder was aangenomen. ATX-remmers kunnen dus het LPA-niveau in de bloedcirculatie verlagen en hiermee een belangrijke bijdrage leveren om de rol van ATX en LPA in ziekten verder op te helderen.

Tijdens de voorgaande studies was de ruimtelijke structuur van ATX nog niet bekend. Deze structuur is belangrijk om de functie en het mechanisme van ATX op atomair niveau te bestuderen. Recentelijk is er een kristalstructuur van ATX gebonden aan de ATX-remmer HA155 opgehelderd, welke laat zien hoe HA155 bindt aan ATX. HA155 is de naam van een actiever boorzuuranaloog van de hierboven beschreven HA130. Deze kristalstructuur bevestigt de hypothese dat het boorzuur in HA155 het actieve centrum van ATX blokkeert door te binden aan het nucleofiele zuurstofatoom van het katalytische threonine-residu in ATX. De 4-fluorobenzylgroep van HA155 bindt aan een hydrofobe (waterschuwe) uitsparing waar normaal gesproken de hydrofobe staart van LPA aan bindt. De kennis van hoe het HA155 molecuul aan ATX bindt geeft een idee waar in de chemische structuur van HA155 modificaties toegestaan zijn. Gebruikmakend van deze kennis zijn er verschillende nieuwe boorzuuranalogen van HA155 ontworpen en gemaakt. Dit heeft uiteindelijk geresulteerd in een zeer actief boorzuuranaloog van HA155, genaamd *E*-**28**, dat een *E*-geconfigureerde dubbele binding heeft in plaats van een *Z*-configuratie zoals in HA155 en alle andere geteste analogen van HA155. Dit betekent dat de 4-fluorobenzylgroep in *E*-**28** een compleet andere ruimtelijke oriëntatie heeft dan in HA155. Men zou dan ook verwachten dat deze 4-fluorobenzylgroep anders bindt aan de hydrofobe uitsparing in ATX, in vergelijking met HA155. Om te verklaren hoe *E*-**28** zou kunnen binden aan ATX zijn er computersimulaties uitgevoerd. In deze studie hebben we de binding van *E*-**28** aan het actieve centrum van ATX gesimuleerd. Dit suggereerde dat *E*-**28** anders bindt aan de hydrofobe uitsparing in ATX in vergelijking met HA155 en andere *Z*-geconfigureerde analogen. Echter, een kristalstructuur van *E*-**28** gebonden aan ATX zal dit moeten bevestigen. De vinding dat *E*-**28** mogelijk anders bindt aan de hydrofobe uitsparing in ATX dan HA155, kan gebruikt worden voor het ontwerpen van nieuwe ATX-remmers.

DUSP-remmers

Een ander belangrijk onderwerp beschreven in dit proefschrift is de bestrijding van bacteriële infecties door middel van het remmen van duale specificiteit fosfatasen (DUSP). Bacteriële infecties zijn nog steeds een grote sociale bedreiging. Zo sterven jaarlijks ongeveer 500.000 mensen aan buiktyfus veroorzaakt door de bacterie *Salmonella Typhi*. De meeste sterfgevallen van deze ziekten vinden plaats in de derde wereld. Ook de recente uitbraak van de Enterohemorragische *Escherichia coli* (EHEC) bacterie in Europa laat zien dat bacteriële infecties serieus genomen moeten worden. Door de resistentie van bacteriën voor meerdere typen antibiotica (multidrug resistance, MDR) wordt het steeds moeilijker om deze bacteriële infecties te behandelen. Nieuwe strategieën zijn daarom nodig om deze resistente bacteriën te overwinnen.

Dikwijls verschuilen pathogene (ziekmakende) bacteriën zich in de cellen van de gastheer om zo te kunnen ontsnappen aan het immuunsysteem. Daarnaast hebben deze bacteriën bepaalde eiwitten van de gastheercel nodig om te kunnen overleven. Het ontwikkelen van geneesmiddelen die aangrijpen op deze gastheer eiwitten, kan een alternatieve strategie zijn om bacteriële infecties te behandelen. In deze studie is er gekeken naar welke fosfatasen, een klasse van eiwitten, van humane gastheercellen essentieel zijn voor de overleving van de bacterie *Salmonella (S.) typhimurium*. Dit bleken de fosfatasen DUSP3, 11 en 27 te zijn.

Daarnaast zijn er moleculen, die ontworpen zijn om DUSP-fosfatasen te remmen, getest op de vermindering van de *S. typhimurium*-infectie van menselijke gastheercellen. Eén van deze verbindingen bleek de eerder geïdentificeerde DUSP-eiwitten van de gastheer die essentieel zijn voor *S. typhimurium*-infectie te remmen. Deze verbinding werd vervolgens geoptimaliseerd, wat resulteerde in een actieve en selectieve remmer van DUSP3, met een minstens 15-voudig verhoogde activiteit in vergelijking met DUSP27. Tegenlijkertijd is de kristalstructuur van DUSP27 opgelost naast de al bekende structuur van DUSP3. Een computersimulatie van de binding van deze remmer met zowel DUSP3 als met DUSP27 suggereert een waterstofbrug tussen deze remmer en een tyrosine residu in DUSP3, dat niet gevormd kan worden in DUSP27. Dit is een mogelijke verklaring voor de selectiviteit van deze remmer voor DUSP3. Het tyrosine residu van DUSP3 dat een waterstofbrug vormt met de selectieve DUSP3-remmer, is niet geconserveerd in de consensus sequentie (HCXXGXXR) die typerend is voor het actieve centrum van de DUSP-familie. Het gebruikmaken van niet-geconserveerde actieve centrum residuen in de DUSP-familie kan mogelijk een goede strategie zijn voor de ontwikkeling van selectieve DUSP-remmers met antibacteriële werking. Het ontwikkelen van selectieve fosfataseremmers is een uitdagende taak door de sterk geconserveerde actieve centrum residuen in fosfatasen.

Concluderend, het remmen van de activiteit van DUSP-eiwitten in de gastheer die essentieel zijn voor bacteriële overleving, lijkt een goede strategie te zijn om bacteriële infecties te bestrijden. Deze nieuwe aanpak kan een nuttige aanvulling zijn op de huidige behandeling van bacteriële infecties die zich alleen richten op het direct doden van de bacterie. Deze nieuwe strategie is ook interessant omdat de ontwikkeling van bacteriële resistentie tegen deze remmers wellicht moeilijker is.

Curriculum vitae

Harald Matheas Henricus Gerardus Albers werd geboren op 15 september 1980 te Venray. In 1997 behaalde hij zijn VBO-diploma aan het Agrarisch Opleidings Centrum te Horst. Vervolgens voltooide hij zijn HAVO (1999) en VWO (2001) studie aan het Dendron College in Horst. Met zijn interesse voor natuurwetenschappen begon hij in 2001 aan de studie Scheikundige Technologie aan de Technische Universiteit Eindhoven (TU/e). Tijdens zijn academische scheikundige opleiding aan de TU/e heeft hij zich verder verdiept in de biologie met als hoofdinteresse oncologie. Hij volbracht zijn afstudeeropdracht binnen de vakgroep van Professor E.W. (Bert) Meijer, waar hij onderzoek deed naar de aggregatie van C3-symmetrische discoten uitgerust met een MRI-label als supramoleculaire MRI contrastmiddel. In maart 2007 behaalde hij *cum laude* het ingenieurs examen Chemical Engineering and Chemistry aan de TU/e. Vanaf april 2007 begon hij aan het promotieonderzoek in de groep van Dr. Huib Ovaa aan het Nederlands Kanker Instituut (NKI) te Amsterdam. Hij presenteerde de resultaten van zijn promotieonderzoek op verschillende nationale en internationale congressen waaronder hij een lezing gaf in 2011 tijdens het 241ste congres van de American Chemical Society (ACS) voor de Division of Medicinal Chemistry in Anaheim, Californië. Tijdens deze congressen heeft hij verscheidene prijzen gewonnen, waaronder in 2007 de *Best Poster Prize Fundamental Science* tijdens de jaarlijkse PhD retraite van de Oncology Graduate School Amsterdam, in 2010 de *Best Poster Prize* van de farmacochemie sessie en de eerste prijs in de *PhD Student Competition* op de FIGON Dutch Medicine Days, in 2011 de *Best Poster Prize* tijdens de Netherlands Proteomics Centre Progress Meeting en in 2011 de *Best Presentation Prize* van de farmacochemie sessie gedurende de FIGON Dutch Medicine Days. Tenslotte won hij de *Best Poster Prize* tijdens de conferentie CHAINS2011, georganiseerd door NWO en de KNCV.

List of publications

Albers, H.; Kuijl, C.; Scanu, T.; Hendrickx, L.; Wekker, S.; Farhou, N.; Liu, N.; Celie, P.; Ovaa, H.; Neefjes, J. Controlling Bacterial Infection by Human Dual Specificity Phosphatase Inhibition. *Manuscript in preparation.*

Albers, H.; Ovaa, H. Chemical Evolution of Autotaxin Inhibitors. *Accepted for publication in Chemical Reviews.*

Albers, H.; Hendrickx, L.; van Tol, R.; Hausmann, J.; Perrakis, A.; Ovaa, H. Structure-Based Design of Novel Boronic Acid-Based Inhibitors of Autotaxin. *Journal of Medicinal Chemistry* **2011**, *54*, 4619-4626.

Besenius, P.; van den Hout, K.; **Albers, H.**; de Greef, T.; Olijve, L.; Hermans, T.; de Waal, B.; Bomans, P.; Sommerdijk, N.; Portale, G.; Palmans, A.; van Genderen, M.; Vekemans, J.; Meijer, E. W. Controlled Supramolecular Oligomerization of C3-Symmetrical Molecules in Water: The Impact of Hydrophobic Shielding. *Chemistry A European Journal* **2011**, *17*, 5193-5203.

Hausmann, J.; Kamtekar, S.; Christodoulou, E.; Day, J.; Wu, T.; Fulkerson, Z.; **Albers, H.**; van Meeteren, L.; Houben, A.; van Zeijl, L.; Jansen, S.; Andries, M.; Hall, T.; Pegg, L.; Benson, T.; Kasiem, M.; Harlos, K.; Kooi, C.; Smyth, S.; Ovaa, H.; Bollen, M.; Morris, A.; Moolenaar, W.; Perrakis, A. Structural Basis of Substrate Discrimination and Integrin Binding by Autotaxin. *Nature Structural & Molecular Biology* **2011**, *18*, 198-204.

Albers, H.; van Meeteren, L.; Egan, D.; van Tilburg, E.; Moolenaar, W.; Ovaa, H. Discovery and Optimization of Boronic Acid-Based Inhibitors of Autotaxin. *Journal of Medicinal Chemistry* **2010**, *53*, 4958-4967. *

Albers, H.; Dong, A.; van, M.; Egan, D.; Sunkara, M.; van, T.; Schuurman, K.; van, T.; Morris, A.; Smyth, S.; Moolenaar, W.; Ovaa, H. Boronic Acid-Based Inhibitor of Autotaxin Reveals Rapid Turnover of LPA in the Circulation. *Proceedings of the National Academy of Sciences of the United States of America* **2010**, *107*, 7257-7262.

Cavalli, S.; Houben, A.; **Albers, H.**; van Tilburg, E.; de Ru, A.; Aoki, J.; van Veelen, P.; Moolenaar, W.; Ovaa, H. Development of an Activity-Based Probe for Autotaxin. *ChemBioChem* **2010**, *11*, 2311-2317.

** Faculty of 1000 (F1000) citation.*

Nawoord

In 2007 begon voor mij het nomadenbestaan tussen Helmond en Amsterdam. Uiteindelijk heeft dit geleid tot de totstandkoming van dit proefschrift wat gepaard is gegaan met veel samenwerking en steun van anderen. Daarom wil ik hier van de gelegenheid gebruik maken om bepaalde mensen in het bijzonder te bedanken.

Huib, het is ongelofelijk hoe jouw groep is gegroeid in de afgelopen jaren. Naast de prachtige artikelen en diverse beurzen heb je nu ook de prestigieuze Gouden KNCV medaille bemachtigd. Voor dit alles heb ik veel respect. Het autotaxine (ATX) project valt buiten het hoofdonderzoek van je groep, waardoor ik hier zelfstandig aan heb kunnen werken. Ik wil je bedanken voor de academische vrijheid die je me hebt gegeven in de afgelopen jaren en die uiteindelijk heeft geresulteerd in verscheidene artikelen en dit proefschrift.

Zoals de meesten in de inhoudsopgave hebben gelezen gaat het grootste gedeelte van mijn onderzoek over de ontwikkeling van ATX-remmers. Daarom wil ik binnen het ATX-team verschillende mensen bedanken. Natuurlijk te beginnen met Wouter. Jouw kennis van ATX en LPA is ongelooflijk, hier heb ik dan ook veel van mogen leren. Laurens, bedankt voor al je hulp in het begin van mijn promotie. Anna, veel succes met het afronden van je promotieonderzoek en met je nieuwe baan in Barcelona. Olaf, bedankt voor alle *in vivo* experimenten. Leonie, welkom bij het ATX-team. Der Jens, Viel Glück in Anspruch nehmen. Dave, every successful inhibitor discovery program starts with a proper screen as we have proven. Andrew & colleagues, our collaboration was very fruitful. Tassos, I'm very grateful that you and your group have resolved the ATX-HA155 structure during my PhD study. This inspired me to further explore the wonders and beauty of the world of structural biology.

Van het bacterie/DUSP-team wil ik als eerste Sjaak bedanken. Jouw enthousiasme voor de wetenschap is aanstekelijk en ongeremd. Jouw oorverdovende lokroep net voor de Neefjes-werkbespreking is niet meer weg te denken van onze afdeling. Tiziana and Petra, thank you for your help with the FACS experiments. Coen, het samenwerken met jou was erg prettig en heeft mooie resultaten opgeleverd. Ook heb ik veel plezier beleefd aan ons bezoek bij jullie in San Francisco. Veel geluk en succes gewenst samen met Diane en jullie dochtertje Anna. Patrick, ik wil je bedanken voor je bijdrage aan het DUSP gedeelte van mijn onderzoek. Voornamelijk het oplossen van de DUSP27 structuur geeft dit onderzoek een extra dimensie.

Erica, een van de pioniers van de Ovaa-groep, ik wil je bedanken voor de goede begeleiding en onze miniwerkbesprekingen die altijd erg verhelderend waren, maar ook gezellig. Helaas was onze samenwerking van korte duur aangezien je snel na mijn komst naar Rotterdam vertrok. Waarschijnlijk had ik nog veel meer van jou kunnen leren. Boris, jouw bijdrage aan de Ovaa-groep was en is groot. Naast je belangrijke bijdrage aan het opzetten van de infrastructuur binnen de Ovaa-groep wil ik je persoonlijk bedanken voor de talloze keren dat je naar de UvA bent gereisd voor onze NMR-metingen.

De kamergenootjes van het Ovaa-hoofdkantoor: Kim, jouw creativiteit is grenzeloos, zowel wetenschappelijk als grafisch. Diverse keren heb je mij advies gegeven over illustraties voor posters, presentaties en artikelen. Je was ook nooit te verlegen om een PNAS-grapje te maken en kon goed je vrouwtje staan tegenover onze kamerhopper, Farid. Ook Farid wil ik bedanken voor onze gesprekken over de wetenschappelijke politiek. Ik ben benieuwd welke kamer jouw volgende werkplek zal zijn. And I want to thank Dharjath for our nice conversations and breakfast cookies.

Henk, onze peptide-man. Je zit misschien qua locatie een beetje verstopt op onze afdeling, maar je bent onmisbaar voor de Ovaa-groep. De talloze peptides die je maakt zijn nodig in de meeste onderzoeksprojecten binnen onze groep. Jouw sarcasme en ironie kan ik erg waarderen. Ook heb ik erg genoten van je wereldse verhalen onder het genot van een kopje koffie.

Tijdens mijn promotieonderzoek heb ik ook de eer gehad om verschillende studenten te begeleiden. Sharida, bedankt voor de vele analogen die je voor mij hebt gemaakt. Rob, jij hebt een belangrijke bijdrage geleverd aan hoofdstuk 4. Bedankt voor de mooie ATX-remmers die je hebt gemaakt. Loes, mijn eerste studente, hoe jou te bedanken? Het was erg plezierig om je te begeleiden en ik heb er zelf ook veel van geleerd. Jouw (academische) aanwezigheid zal niet vergeten worden.

Veel mensen vergeten dat een succesvolle afdeling steunt op de schouders van de ondersteunende staf. Trudi, Suzanne, Patty, Lennert, Marieke en Hans bedankt voor al jullie hulp. Daarnaast wil ik alle huidige en voormalige collega’s, in het bijzonder Nalan en Silvia, bedanken voor hun hulp en gezelligheid.

Vrienden zijn erg belangrijk tijdens een promotieonderzoek en ze zorgen voor de nodige ontspanning. Appel en Tielke, Willy en Edith, Daan en Maura, ik wil jullie bedanken voor alle gezellige avondjes en activiteiten en ik hoop dat er nog vele mogen volgen. Appel, ik wil jou in het bijzonder bedanken voor al je hulp rondom dit proefschrift. Naast je nieuwe baan en je drukke gezinsleven was je nooit te beroerd om kritisch te kijken naar mijn proefschrift.

Alfa-onderzoekers kunnen als de beste het bèta-onderzoek in perspectief plaatsen. Hiervoor wil ik mijn zus Karianne en mijn schoonbroer Raymond bedanken.

Pap en Mam, zonder jullie was dit proefschrift nooit mogelijk geweest. Jullie hebben me altijd gesteund tijdens mijn lange studietraject en jullie toewijding was dan ook groot. Alle congressen die ik bijwoonde en prijzen die ik won werden nauwkeurig gearchiveerd. Ook stonden jullie altijd klaar als ik weer eens een keer moest verhuizen. Het was vaak moeilijk uit te leggen waar ik qua onderzoek mee bezig was, maar dat werd gelukkig gecompenseerd door de vele verhalen binnen huize Albers. Ik ben dankbaar dat ik jullie beiden persoonlijk kan bedanken: Pap en Mam, bedankt woa!

Patricia, lieve schat, waar te beginnen. We kennen elkaar al zo lang dat woorden eigenlijk overbodig zijn. Toch wil ik je bedanken voor je steun en begrip, vooral omdat onze dagelijkse levens zo verschillend zijn. We hebben de afgelopen jaren veel moeten opgeven door mijn nomadenbestaan, maar het heeft ook mooie momenten opgeleverd zoals onze reis naar Amerika en onze motorritten. Hopelijk mogen we nog veel van deze mooie momenten samen delen.

Harald